The Optical System and the Astronomical Potential of A-MKID, a New Camera Using Microwave Kinetic Inductance Detector Technology

Dissertation
zur
Erlangung des Doktorgrades (Dr. rer. nat.)
der
Mathematisch-Naturwissenschaftlichen Fakultät
der
Rheinischen Friedrich-Wilhelms-Universität Bonn

von
Luis Esteras Otal
aus
Reus, Spanien

Bonn, 21.08.2014

Dieser Forschungsbericht wurde als Dissertation von der Mathematisch-Naturwissenschaftlichen Fakultät der Universität Bonn angenommen und ist auf dem Hochschulschriftenserver der ULB Bonn http://hss.ulb.uni-bonn.de/diss_online elektronisch publiziert.

1. Gutachter:	Prof. hon. Dr. Karl Menten
2. Gutachter:	Prof. Dr. Frank Bertoldi
Tag der Promotion:	15.12.2014
Erscheinungsjahr:	2015

A mi madre.

Para algunos la vida es galopar un camino
empedrado de horas minutos y segundos,
y yo, más humilde soy, y sólo quiero
que la ola que surge del último suspiro
de un segundo, me transporte mecido hasta el siguiente.

Santos Isidro Sesea

Abstract

In the framework of sub-millimeter astronomy, the need to create more efficient cameras with more pixels, with larger FoV and with higher mapping speed is highly desirable. In order to satisfy this necessity a new camera based on Microwave Kinetic Inductance Detectors (MKID) technology has been developed for the APEX Telescope (located in one of the best sites on Earth for sub-millimeter observations). In order to increase even more the observing efficiency, the camera works at two frequencies simultaneously (LFA: 345 GHz and HFA: 850 GHz). Also, the high angular resolution of the HFA ($\sim 8''$), provides more accurate size estimates and position of the sources.

With this aim, a novel optical design with a complete diffraction limited field of view of $>$15 x 15 arcmin^2, in the two working frequencies, has been developed for the new camera. The system has been designed to optimize the MKIDs' response, as well as to minimize the number of optical elements used in order to optimize its compactness.

The first commissioning of the new camera, called A-MKID, was accomplished during December 2013. Some problems regarding cryogenics and read-out electronics were detected. Beam characterization studies revealed misalignments produced during the optics installation. This fact caused some aberration in several parts of the array.

Furthermore, observations of an astronomical Galactic target, the nebula NGC3603, have been performed with the new camera, obtaining a map with a sensitivity per beam a factor ~ 3 worse than that of the Large APEX Bolometer Camera (LABOCA). This low sensitivity was mainly due to read-out electronics issues and the misalignments produced. Nevertheless, no strange artifacts were detected in these observations and no fundamental obstacles were encountered.

In order to demonstrate the high scientific potential of continuum observations at these wavelengths, a study of the dust component of the well known nebula M17 SW has been carried out. Although no data of the new camera could be included in this study (they will be included in further publications), interesting results have been achieved with the available data of this source in the sub-millimeter and infrared

wavelength regime. At the same time, the study also reveals that observations of this kind of structures in the sub-millimeter range could be done in a more efficient way with a the larger A-MKID camera. In addition, the new camera will provide data at 850 GHz which is not currently available for this and other important sources.

Spectral Energy Distributions (SEDs) were calculated along a strip of measurements using a specific aperture size. This allowed to cover the complete region in order to characterize the different gas phases from the H_{II} region to the molecular cloud, including the photon-dominated region (PDR) located in between.

The SEDs were well modeled using a combined function of two gray-body laws, each of them representing a cold and a hot component.

Temperatures between 50 and 120 K and column densities (N_{H_2}) around 10^{22} cm^{-2} were obtained for the cold component, while for the hot component a temperature range between 250 and 310 K, and column densities (N_{H_2}) of roughly 10^{19} cm^{-2} were estimated. Moreover, additional important parameters such as mass, optical depth and visual extinction were also derived from our SED fits.

Our results are in agreement with the common PDR structure reported by Hollenbach & Tielens (1997), but they could also be interpreted in terms of a clumpy PDR model.

Contents

1

Introduction

The A-MKID camera is a receiver based on Microwave Kinetic Inductance Detectors (MKIDs) as sensing elements. This technology allows efficient frequency-domain multiplexing and therefore high pixel counts for the overall camera system.

The camera operates in the sub-millimeter range, simultaneously in two frequency bands: 870 μm (345 GHz) and 350 μm (850 GHz), and offers in total about 25000 pixels to the user.

The most significant limitations to the detection of astronomical emission at sub-millimeter wavelengths are atmospheric emission, noise and attenuation. The sub-millimeter atmosphere is dominated by numerous water vapor absorption bands, observations are possible only through "windows" between these bands. Therefore a dry and cool site with stable atmosphere is needed for sub-millimeter observations.

In this chapter, firstly the characteristics of the APEX telescope will be summarized. Secondly, the astronomical motivation for the used wavelengths will be given. Thirdly, an overview of the state of the art of millimeter and sub-millimeter detection technologies and also of the current receivers which operate with these technologies will be presented. Finally a brief explanation about the technology (MKID) used and implemented for our camera will be shown.

1.1 APEX telescope

The A-MKID camera will be installed on the Atacama Pathfinder Experiment telescope (APEX). The APEX telescope is a 12 meters dish telescope located in Llano Chajnantor (Atacama desert, Chile) at 5105 meters altitude (see figure 1.1).

FIGURE 1.1— APEX telescope at Llano Chajnantor. Image extracted from APEX web-page[1].

On Llano Chajnantor the amount of precipitable water vapor (PWV) is typically 1.0 mm and falls below 0.5 mm up to 25% of the time, making this site one of the best on Earth for sub-millimeter observations. Figure 1.2 shows the atmospheric transmission between 200 GHz and 1.6 THz for different PWV values. On the figure, the different atmospheric windows where observations are possible can be distinguished.

1.2 Astronomical motivation

Millimeter and sub-millimeter astronomy is an important field of the current astronomical research. Since our camera operates in the sub-millimeter range, in the following we will mainly refer to this frequency range; nevertheless, some of the points shown here could be applied to millimeter wavelengths as well. The sub-millimeter range is placed between the far-infrared and microwave wavebands, i.e., between a few hundred micrometers and $\sim$ 3 mm (approximately between one THz and 100 GHz in frequency).

The A-MKID camera is a direct detection camera which provides information about the continuum emission, but it does not work for spectroscopy (molecular line detection). Sub-millimeter continuum emission is a powerful probe of the warm and cool dust in the universe. Fitting a (modified) Planck law to the observed continuum

[1] http://www.apex-telescope.org/

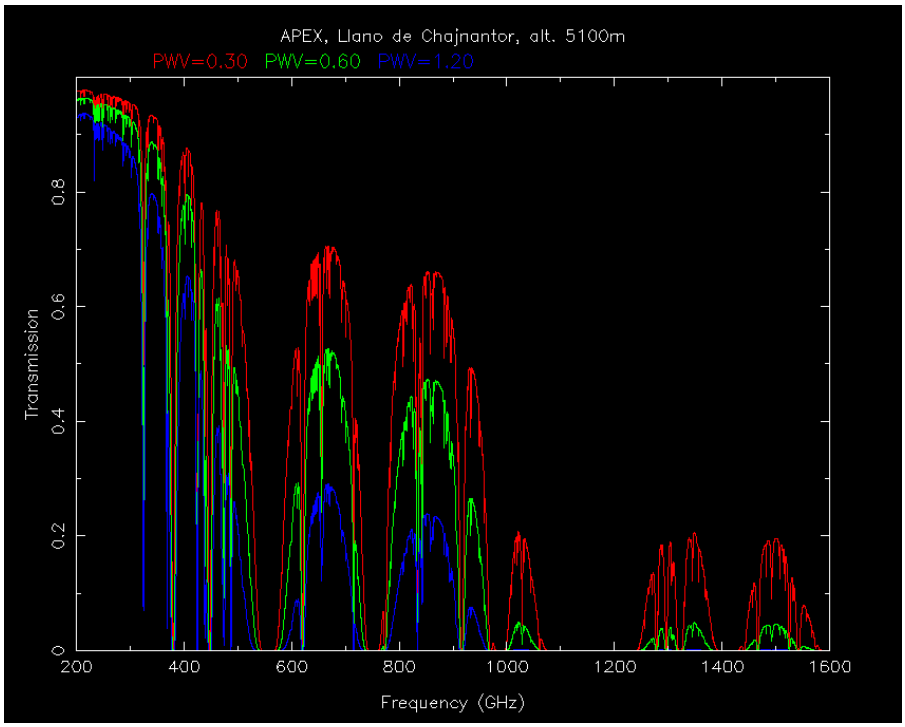

FIGURE 1.2— Atmospheric transmission between 200 GHz and 1.6 THz for different PWV values at the APEX site (Llano Chajnantor). Image extracted from APEX web-page[1].

data the temperature can be easily determined. The peak of the Planck function is directly related to the temperature. The frequency range in which the Planck function peaks for the dust temperatures found in the interstellar medium ($T \sim 10-200$ K) lies at sub-millimeter wavelengths. In this framework several important fields of research can be studied (Siringo et al. 2009):

1. **Star formation in the Milky Way:**

   Dust emission is a direct tracer of the gas column density and the gas mass. Large scale surveys in the Milky Way reveal the distribution and gas properties of a large number of pre-stellar clusters and cores in different environments and evolutionary stages. They also provide information on the structure of the interstellar medium on large scales at high spatial resolution. With them we are able to improve our understanding of the processes that govern star formation as well as the relation between the clump mass spectrum and the stellar initial mass function. Such surveys are also important for finding precursors of high-mass stars, which are undetectable at other wavelengths due to the high obscuration

by the massive cores in which they are embedded (Siringo et al. 2009).

In this context, a study of the dust component of the Galactic star forming region M17 SW is carried out in chapter 3.

2. **Cold gas in galaxies:**

   The only reliable way to trace the bulk of dust in galaxies is through sub-millimeter and far-infrared observations. According to recent studies, it seems that most of the dust mass in spiral galaxies lies in cold, low surface-brightness disks, often extending far from the galactic nucleus (e.g. Weiß et al. 2008). It is important to study this component because it contains a significant amount of the total gas mass in galaxies while studies based on H_I observations heavily underestimate the gas surface density.

   Moreover, sub-millimeter observations will be extremely useful for determining the low-z galaxy standards, such as the local luminosity and dust mass functions, which are required to interpret information from distant objects found in deep cosmological surveys (Siringo et al. 2009).

3. **Galaxy formation at high redshift:**

   Sub-millimeter continuum emission is also a prominent tool for the study of the distant universe. Because of the expansion of the universe, the peak of the emission shifts toward the lower frequencies with increasing cosmological distance, favoring the detection at sub-millimeter wavelengths. Sub-millimeter observations show equal sensitivity to dusty star-forming galaxies over a redshift range from $z \sim 1 - 10$; detections at these redshifts are possible because of the so-called negative K-correction (first discussed by Blain & Longair 1993). This fact makes sub-millimeter observations useful to obtain information about the star formation history at epochs from about half to only 5% of the present age of the universe.

   Recent studies show that the volume density of luminous sub-millimeter galaxies (SMGs) increases by roughly a factor thousand near $z \sim 2$ (Chapman et al. 2005), and therefore, in contrast to what happens in to the local universe, this would mean that the SEDs[1] from luminous obscured galaxies at high redshifts (e.g. LIRGs[2] and ULIRGs[3]) peak at sub-millimeter wavelengths because of thermal dust emission.

   Since the sub-millimeter dust emission can be converted into dust/gas masses, a direct estimate of the star formation rates (SFRs) of these objects can be cal-

[1] SED: Spectral Energy Distribution
[2] LIRGs: Luminous Infrared Galaxies
[3] ULIRGs: Ultra-Luminous Infrared Galaxies

culated. Generally, high SFRs are obtained, which suggests that approximately half of all the stars that are observed today may have formed in highly obscured systems that remain undetected at optical or near-infrared wavelengths.

1.3 Sub-millimeter detection technologies and receivers

Over the years different detector types have been developed in the millimeter and sub-millimeter range; first using conventional bolometers and later using improved technologies as TES[4] bolometers, or MKIDs (our technology; see next section).

A bolometer is a temperature sensor. The power of the incident radiation is measured via the heating of an absorbing material with a temperature-dependent electrical resistance. The bolometer principle is the following (see figure 1.3): An incident signal with power P is absorbed by the bolometer and heats up a thermal mass with heat capacity C and temperature T_B. The thermal mass is connected to a heat sink of constant temperature (T_S) through a link with thermal conductance G. Hence, the temperature increase produced by the incident signal is $\Delta T = P/G$ (thus, $T_B = T_S + \Delta T$) with an intrinsic thermal time of τ = C/G (Richards 1994). The change in temperature is read out with a resistive thermometer and this is the resulting signal.

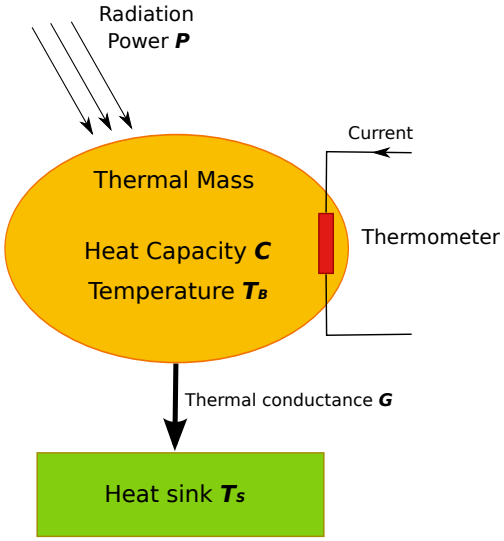

FIGURE 1.3— Schematic of the bolometer working principle.

Some receivers have been developed with this technology, like MAMBO[5] (Kreysa

[4]TES: Transition Edge Sensors
[5]MAMBO: MAx-Planck Millimeter BOlometer

et al. 2002) with 117 bolometers (or pixels) in its latest upgrade and operating at 1.2 μm (250 GHz), or LABOCA[6] (Siringo et al. 2009) with 295 bolometers (or pixels) and operating at 870 μm ($345GHz$). In both cases so-called composite bolometers were used; they use different materials in their parts in order to separately optimize the critical bolometer parameters, like thermal conductivity, heat capacity and absorptivity. They can be simplified by the combination of two elements: an extremely sensitive temperature sensor, called thermistor and made by a semiconductor material, and a radiation absorber made by a metallic film. More information about this type of bolometer and some others can be found in Richards (1994).

Over time, very good performance has been reached with these detectors. The sensitivity achieved with instruments based on them was background limited and arrays of hundreds of these detectors (hereafter called conventional bolometers) could be manufactured. However, when larger arrays are needed to increase mapping speed (to reduce observing time) some form of multiplexing is needed to reduce the cryogenic wire counts (reduce the wiring overhead). With conventional bolometers each one needs "its own" wiring and if the number of bolometers is increased there is a point where the device is physically nearly impossible to manufacture. Several studies shows that time domain multiplexing or rapid switching can be achieved using quantum contact high-mobility transistors (Benoit et al. 2008) or MOSFETs[7] (Revéret et al. 2008). Indeed, this technique has been demonstrated with considerable success by integrating superconducting quantum interference devices (SQUIDs) into a type of bolometer known as TES[8] (Benford et al. 2000; Siringo et al. 2010; Holland et al. 2013). Moreover, combining SQUIDs with frequency-domain multiplexing TESs has also been achieved, where instead of switching between separate wires the bandwidth of a single wire is subdivided between multiple pixels (Yoon et al. 2001, Irwin & Lehnert 2004, Irwin & Hilton 2005).

TESs are superconducting sensors instead of semi-conducting thermistors. In a TES bolometer the transition between the superconducting and the normal state is used as an extremely sensitive thermometer and very high sensitivity can be achieved (Benford et al. 2000). The low-impedance detector which represents a superconducting TES is well matched by a superconducting SQUID amplifier. In a few words, a SQUID amplifier works as a magnetic flux-to-voltage converter with extremely low output voltage noise. Figure 1.4 shows how the coupled TES-SQUID system works. A voltage-biased TES placed in series with an inductor near a SQUID induces a changing flux through the SQUID when the TES resistance changes.

The TES multiplexing (in time-domain which is the most used one in millimeter

[6]LABOCA: Large APEX BOlometer CAmera
[7]MOSFET: MetalOxideSemiconductor Field-Effect Transistor
[8]TES: Transition Edge Sensor

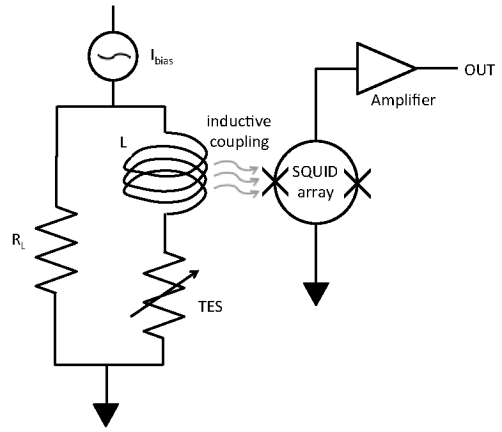

FIGURE 1.4— Schematic of the TES-SQUID working principle. Figure extracted from Benford et al. (2000).

and sub-millimeter receivers) can be understood as follows (see figure 1.5): a SQUID amplifier can be switched rapidly between an operational and a nonoperational, superconducting state by biasing the SQUID with a specific current. If n SQUIDs are stacked in series with n+1 electrical address wires, a driving current between an adjacent pair of wires will result in only one operational SQUID. Since the other SQUIDs are in the superconducting state, the output voltage across the entire array is exactly the voltage across the one active SQUID. In this way, only one amplifier is necessary for n detectors. Hence, adding the connections for the common TES bias and feedback signal, a total of n+7 wires are needed (Benford et al. 2000).

In a realistic scenario a two-dimensional array is considered (array of m rows and n columns). In this case a significant advantage can be achieved since the columns can share common address lines and thus only one amplifier is needed. In the most straightforward wiring scheme, $4n+m+3$ wires are needed, unlike discrete bolometer arrays where $8mn$ wires are necessary to fully wire them (Benford et al. 2000).

Several receivers have been developed using this technology: SABOCA[9] (Siringo et al. 2010), SCUBA-2[10] (Holland et al. 2013), MBAC[11] (Zhao et al. 2008) and others.

Nevertheless, even larger arrays are desirable (many kilo-pixels) and SQUID multiplexing systems become very complex and at a certain point they are limited by the multiplexing factor of the readout electronics. Therefore, the necessity to develop detectors which intrinsically are adapted to strong multiplexing becomes

[9]SABOCA: Submillimeter APEX Bolometer Camera

[10]SCUBA-2: Submillimetre Common-User Bolometer Array 2 in the JCMT

[11]MBAC: Millimeter Bolometer Array Camera in the ACT

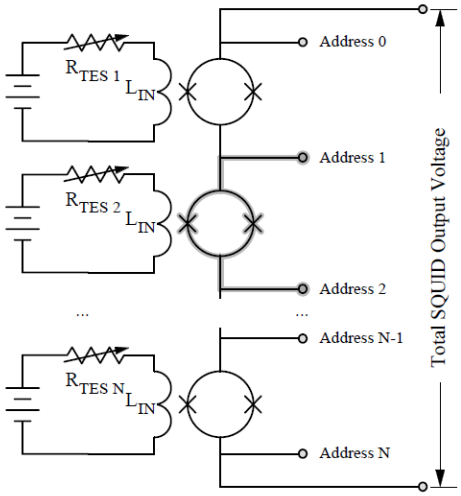

FIGURE 1.5— TES one-dimensional multiplexing principle. Figure extracted from Benford et al. (2000).

highly important. One potential and relatively new technology (not bolometer based) that achieves high sensitivity and is fundamentally compatible with frequency-domain multiplexing is the Microwave Kinetic Inductance Detector (MKID, next subsection).

1.4 MKID technology

The primary attraction of MKIDs is that unlike many other low temperature detectors they are easy to multiplex into large arrays (Zmuidzinas & Richards 2004; Mazin et al. 2006) because they can be easily implemented as high-quality superconducting resonant circuits, electromagnetically coupled to a single transmission line.

MKIDs rely on the principle that incident photons change the surface impedance of a superconductor through the kinetic inductance effect (Mazin 2009). To understand this effect, first some concepts about superconductivity have to be summarized. In the superconducting state pairs of electrons (or other fermions) are bound together forming the so-called Cooper pairs. An electron in a metal normally behaves as a free particle. The electron is repelled from other electrons due to their negative charge, but it also attracts the positive ions that make up the rigid lattice of the metal. This positive charge can attract other electrons at the same time. At long distances this attraction between electrons can overcome the repulsion between the electrons due to their negative charge, and cause them to pair up (Kadin 2005). The rigorous quantum mechanical explanation shows that the effect is due to electronphonon interactions (Kadin 2005).

Superconductors have a non-zero impedance for ac currents, which can be represented as:

$$Z_s = R_s + i\omega L_s \tag{1.1}$$

On one hand, Cooper pairs which carry the super-current can be accelerated and decelerated by an electric field; this allows energy to be stored as kinetic energy of the Cooper pairs. This effect of the inertia of the Cooper pairs is known as the kinetic inductance.

On the other hand, at finite temperatures below the superconducting transition temperature (T_c), a small fraction of Cooper pairs is thermally broken. The resulting so-called quasi-particles produce a small surface resistance (R_s). However, the surface impedance produced (see equation 1.1) is purely inductive, $\omega L_s \gg R_s$ (Maloney et al. 2010).

Cooper pairs are bound together by electron-phonon interaction with an energy $2\Delta \simeq 3.5kT_c$ (Δ is the superconducting gap energy). Therefore, photons with energies $> 2\Delta$ that are absorbed by the superconductor can break up Cooper pairs causing an increase in the quasi-particle density and thus a change in the surface impedance Z_s. This change in the surface impedance also generates a change in the resonance frequency and the quality factor Q of the coupled resonant circuit that an MKID represents; this is exactly what is measured in order to compute the flux heating the detector.

Figure 1.6 shows an overview of the MKID detection process: In panel (a) a photon with energy $h\nu > 2\Delta$ is absorbed by a superconducting film cooled to $T \ll T_c$, breaking Cooper pairs and creating a number of quasi-particle excitations $N_{qp} = \eta h\nu/\Delta$ (where η is the efficiency of creating quasi-particles). On the diagram, Cooper pairs (C) are shown at the Fermi level[12], and the density of states for quasi-particles $N_s(E)$ is plotted as the shaded area as a function of quasi-particle energy E. Panel (b) shows that the increase in quasi-particle density changes the surface impedance (equation 1.1) of the film (represented by a variable inductor). The resonant circuit is represented in the plot as a parallel *LC* circuit which is capacitively coupled to a transmission line. Panel (c) shows that on resonance the *LC* circuit loads the trough line producing a dip in its transmission. The quasi-particles produced by the photon increase both L_s and R_s, which moves the resonance to lower frequency (due to L_s) and makes the resonance dip broader and shallower (due to R_s). Both effects change the amplitude (see panel

[12]The Fermi level is the term used to describe the highest electron energy levels at absolute zero temperature. Electrons are fermions and by the Pauli exclusion principle cannot exist in identical energy states. So at absolute zero they pack into the lowest available energy states and build up a "Fermi sea" of electron energy states. The Fermi level is the surface of that sea at absolute zero where no electrons will have enough energy to rise above the surface (http://hyperphysics.phy-astr.gsu.edu/hbase/solids/fermi.html).

(c)) and the phase (see panel (d)) of a microwave signal passed through the circuit (Mazin 2009).

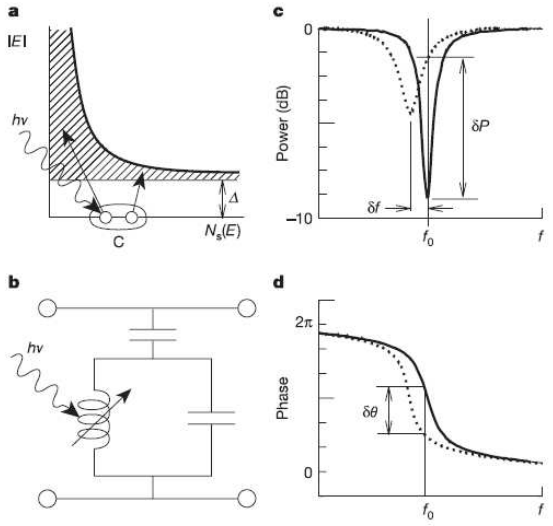

FIGURE 1.6— MKID working mechanism. Figure extracted from Mazin (2009).

This technology introduces a number of advantages compared to other low temperature detectors, such as TESs:

1. The primary advantage is that by using resonant circuits with high quality factors passive frequency-domain multiplexing is allowed; up to thousands of resonators can be read out through a single coaxial cable and a single low-noise cryogenic amplifier, and therefore, the cryogenic wire-count is significantly reduced (Mazin 2009). Figure 1.7 shows on the top panel the electronic circuit representation of an MKID array composed by n LC resonators; the bottom panel shows the frequency response of an MKID array. With this technology frequency-domain multiplexing is possible down to less than 2 MHz frequency spacing (Mazin 2009).

2. Large arrays of MKIDs are significantly easier to fabricate and read out than any competing technology. They do not require any superconducting electronics, and their read-outs can leverage the tremendous advances in room temperature that microwave integrated circuits developed for wireless communication industries have (Mazin et al. 2006).

3. Also, in contrast to TES bolometers which operate at $T \sim T_c$ where the sensitivity to temperature changes is greatest, MKIDs operate at $T \ll T_c$. This leads to a significantly decreased sensitivity to temperature fluctuations and microphonic noise (Monfardini et al. 2010).

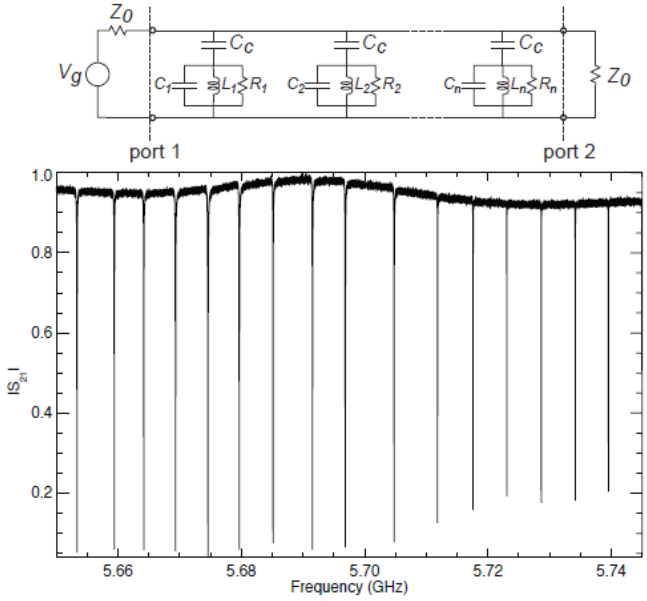

FIGURE 1.7— MKIDs multiplexing. Top panel: an electronic circuit representation of a MKID array composed of n LC resonators. Bottom panel: frequency response of an MKID array with average frequency spacing of 10 MHz. Figure extracted from Mazin (2009).

In order to obtain a high sensitivity of MKIDs to pair-breaking radiation, it is of prime importance to efficiently couple incident radiation into the superconducting resonators. Two distinct technologies have been studied for achieving this coupling:

1. Antenna coupled MKIDs: They are usually implemented as quarter-wave transmission line resonators, capacitively coupled to a feedline on one end, and shorted on the other. At the shorted end normally a slot antenna is attached. The antenna concentrates the incident radiation into the high current-density region of the resonator. In general, in transmission line resonators sensitivity to quasi-particles peaks in areas of high current; in the case of a quarter-wave resonator

this occurs near the end where the slot antenna is located (Mazin 2009). This approach usually requires a micro-lens on top of each pixel for efficient coupling (Monfardini et al. 2010). A single antenna coupled KID resonator can be seen in figure 1.8 in the right panel.

2. LEKIDs (lumped element KIDs): They are composed of two sections: of an interdigitated capacitor and of an inductive meander line to which it is attached, and both together form a resonator. Due to its geometry, the current in the meander section is nearly constant which results in a position-independent response to photon absorption; it becomes an efficient photon absorber. The frequency can be adjusted by changing the length of the inductive meander and the coupling factor can be set by moving the resonator farther from the feedline (Mazin 2009). A single LEKID resonator is shown in figure 1.8 in the left panel.

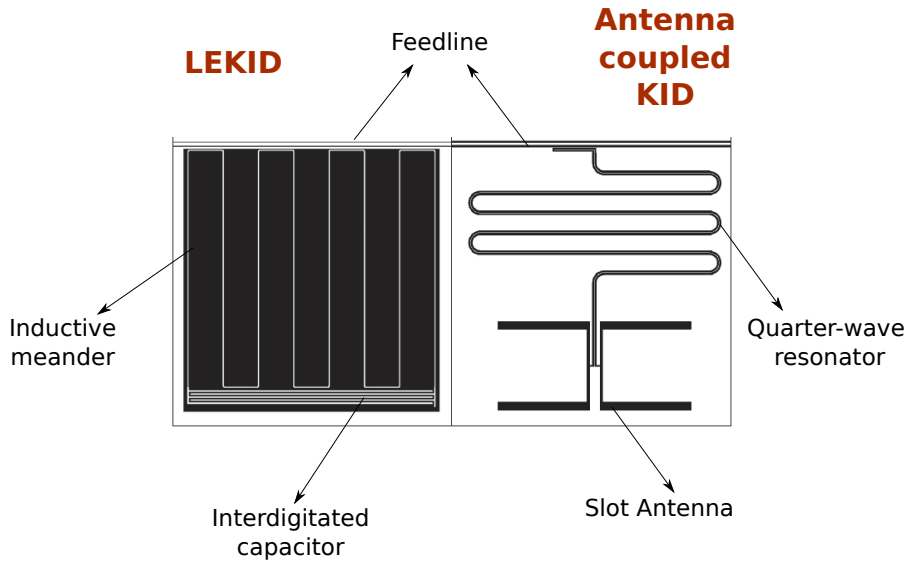

FIGURE 1.8— Real circuit of a single LEKID resonator (left panel) and a single antenna coupled KID resonator (right panel). Figure extracted from Monfardini et al. (2010).

It is important to mention that for both structures the detection process is achieved in the same manner once the incident radiation has been absorbed by the mechanism explained before. On one hand, LEKIDs are easier to make because they do not need quasi-particles to be trapped. However, on the other hand, some studies demonstrate that antenna coupled MKIDs offer higher frequency selectivity (Schlaerth et al. 2008). Also, the slot antenna of the antenna coupled MKIDs is polarization dependent, which

was the main reason for us to chose this structure for our receiver. With a polarization grid in front of the detectors, the working bands of the camera can be split into two polarizations. Therefore, they can work simultaneously using the complete efficiency of the detectors.

As of today, some receivers have been developed with this promising technology with successful results. The first MKID instrument put on the sky was DemoCam which was used on the Caltech Sub-millimeter Observatory 10-meter telescope (CSO), it consisted of a 16-pixel, 2 color/pixel array (Schlaerth et al. 2008). Subsequently, larger arrays have been constructed; NIKA[13] installed at the IRAM 30-meter telescope (Monfardini et al. 2010, Monfardini et al. 2011), consists of a 144 LEKIDs array working at 150 GHz and a 256 antenna-coupled MKID array at 220 GHz. Currently, also other MKID cameras are under development: MUSIC[14], an instrument being developed for the CSO, will have 576 spatial pixels (antenna-coupled MKIDs) in four bands: 850 μm, 1100 μm, 1300 μm and 2000 μm (Maloney et al. 2010, Hollister et al. 2010).

1.5 Main goals

The three main goals of the present thesis project were:

- To design a competitive optical system that fulfills the complete requirements of our A-MKID camera (chapter 2).

- To study and analyze the camera response, once built and installed at the APEX telescope, and to draw conclusions about the array performance, camera field of view, beam shape, side lobes, angular resolution and pixel spacing. In parallel, from this analysis, also conclusions about the optical design performance will be drawn (chapter 3).

- To elaborate a study of the dust continuum component of the well known star-forming region M17 SW, in order to show the high scientific potential of continuum observations at submillimeter wavelengths, since temperatures, column densities and masses (among other useful astronomical parameters) can be derived from them. This study also leads to the conclusion that the found structures will be more efficiently imaged by larger cameras, in particular the A-MKID camera with more pixels, a larger FoV, faster mapping speed and moreover, working at two frequencies simultaneously. Also, the higher angular resolution of the A-MKID high frequency array (HFA) ($\sim 8''$), compared

[13] NIKA: The Néel IRAM KIDs Array
[14] MUSIC: the Multiwavelength Submillimeter kinetic Inductance Camera

with similar cameras, will allow for more accurate size estimates and position determinations of the compact sources found (chapter 4).

2

A-MKID Optics

2.1 Introduction

THe A-MKID camera will operate at two different frequencies simultaneously:

1. Low Frequency Array (LFA): Band center: 870 μm (345 GHz); 34 GHz width (330 – 364 GHz).

2. High Frequency Array (HFA): Band center: 352 μm (850 GHz); 100 GHz width (800 – 900 GHz).

Figure 2.1 shows the frequency response of the bandpass filters for each sub-array (in red), which determines the bandwidth of each detector. The filter response is superposed on the transmission of the atmosphere in a good APEX sub-millimeter night (see also figure 1.2 in chapter 1). As can be seen, the bandpass filters are designed to well match the two atmospheric windows for which the detector has been developed.

Due to the focal ratio from the secondary mirror (sub-reflector of the telescope), the telescope has an f-number of $F = 8$ and the resulting plate scale at the Cassegrain focus is $\simeq 2.15$ arcsec/mm.

One of the goals to achieve with the camera was a diffraction limited field of view (hereafter FoV) for $\sim$ 16 x 16 arcmin^2 for both working frequencies. Nevertheless, since all the different parts of the camera were developed at the same time without knowing the final achievements of each part, the FoV considered for the camera calculations was $\sim$ 15 x 15 arcmin^2 in order to have some margin in the optics design; it is slightly smaller than the original goal but it is still very competitive.

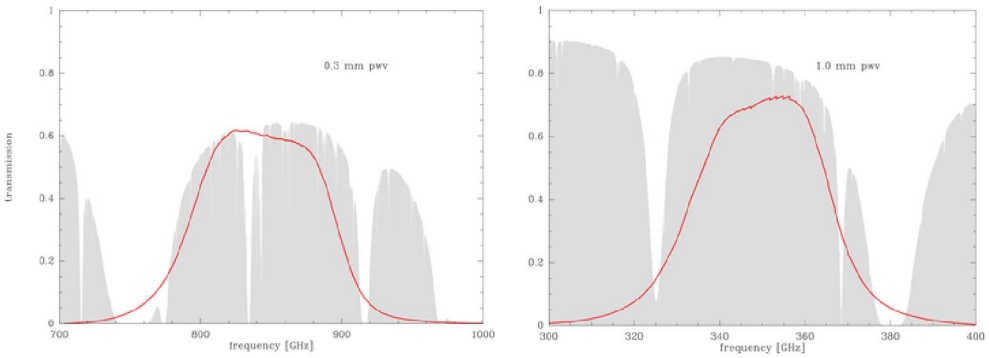

FIGURE 2.1— Frequency response of the bandpass filters for each sub-array (in red) superposed on the transmission of the atmosphere in a good APEX sub-millimeter night. Thanks to the bank of filters located in front of the receiver the two bands are well matching the two atmospheric windows for which the detector has been designed.

Because of the construction constraints of the detector array, it was composed by four detector chips of 58.5 x 58.5 mm each, which gives a size of 117 x 117 mm for the overall detector plane. Figure 2.2 shows the detector plane, where one of the four 58.5 x 58.5 mm detector chips has been installed.

According to the detector size and the required FoV, the magnification of our system could be established. First, the size of the telescope focal plane (in the Cassegrain focus) was calculated,

$$Focal\ plane\ size \simeq \frac{15\ \mathrm{arcmin\,FoV}}{2.15\,\mathrm{arcsec/mm}} \simeq 418.6\,\mathrm{mm} \tag{2.1}$$

and hence, the magnification needed to fit the beams in our detector:

$$Magnification \simeq \frac{418.6\,\mathrm{mm}}{117\,\mathrm{mm}} \simeq 3.58 \tag{2.2}$$

The number of pixels of our camera was computed for both frequencies, but for this the pixel spacing had to be determined first. According to the detector size and the MKID technology the pixel spacing was agreed to be around $\sim 1\ \lambda F$. It is not straightforward to decide the pixel spacing, some studies have been conducted regarding this issue (e.g. Griffin et al. 2002) and the value changes depending on the technology used. A compromise between mapping speed, sensitivity and also resources has to be achieved. We decided on a pixel spacing of $1\ \lambda F$ and obtain:

1. $\lambda_1 F = 6.96\,\mathrm{mm}$ for the lower frequency (LFA).
2. $\lambda_2 F = 2.8\,\mathrm{mm}$ for the higher frequency (HFA).

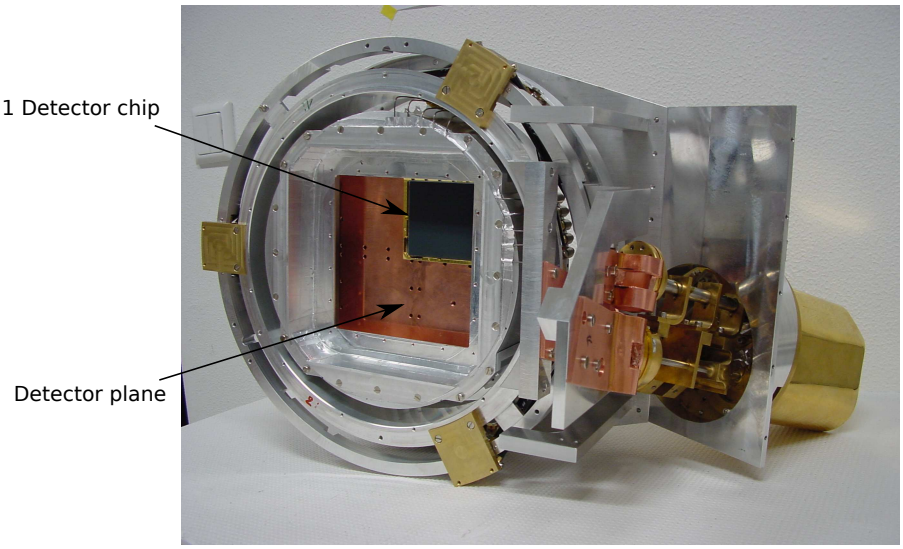

FIGURE 2.2— Detector plane of the A-MKID camera. One of the four 58.5 x 58.5 mm detector chips is already installed.

Also, with the magnification the theoretical physical distance between pixels in the detector plane for exactly 1 λF can be calculated:

1. LFA: $Pix_{dist\ F\lambda_1} = \lambda_1 F / 3.58 \simeq 1.94\,\text{mm}$.
2. HFA: $Pix_{dist\ F\lambda_2} = \lambda_2 F / 3.58 \simeq 0.78\,\text{mm}$.

Finally, the distance considered by SRON[1] for the pixel spacing was slightly larger than the previous values but very close to 1 λF :

1. LFA: $Pix_{dist_1} = 2.0$ mm which represents $\sim 1.03 F\lambda_1$.
2. HFA: $Pix_{dist_2} = 0.8$ mm which represents $\sim 1.02 F\lambda_2$.

From the previous calculations (pixel spacing and detector size) and taking into account the hexagonal pixel arrangement in the detector array, the total number of pixels for each array can be calculated:

1. Number of pixels for the LFA: 3520 pixels.
2. Number of pixels for the HFA: 21600 pixels.

[1] SRON: Netherlands Institute for Space Research `https://home.sron.nl/`

In order to achieve the previous requirements the different aspects of the camera (e.g. optics, cryogenics, read out, MKID development...) required extensive work. Here a small overview of the cryogenics and the read out is given. The MKID detector arrays were provided by SRON and a brief explanation of this technology can be found in the general introduction of this thesis (see section 1.4 of chapter 1). In the body of this chapter a detailed explanation of the optical system is given, from the initial calculations to the final results, passing through the whole optimization process done with the ZEMAX Software[2]. Also, at the end of the chapter a study of the system tolerances resulting from misalignments is reported.

2.1.1 Cryogenics: He 10 cooler

The cryogenic system consists of two 4K pulse-tube closed cycle systems: one to cool the cold optics (M5, M6 and Lyot stop, explained later in this chapter) and the other one to reach the bath temperature for the He 10 cooler, which is the responsible for providing temperatures < 300 mK, needed to operate the detectors. The He 10 cooler is a three stage sorption cooler which uses a mixture consisting of two parts of the ^{3}He isotope and one part of ^{4}He; a ^{4}He - ^{3}He double refrigerator is used to precool and intercept the parasitic heatload for a final ^{3}He single stage refrigerator which reaches the required temperature. A detailed explanation about the mechanism of the 3-stage helium cooler can be found in Bhatia et al. (2000). Figure 2.3 shows the cryostat (open) and the He 10 cooler installed can be seen.

2.1.2 Read-out

For each KID in the detector chip a tone signal is created. After passing the detector, this tone is analyzed in amplitude and phase; the changes in these values provide a direct measurement of the incoming photons.

The tone generation is performed by four 1.1 GHz wide DACs[3]. These four signals are combined in an integrated IF-system to one monolithic 4 GHz wide band with up to 2000 tones for the detectors. After passing the detector chip, the signal is treated again by an IF circuit. The signal is then analyzed by a fast ADC[4] and the difference in phase and amplitude for each KID-tone can be calculated.

For the total system 24 IF chains were designed in highly integrated IF circuits. Each channel (each chain) is composed of two boards, an up-converter and a down-converter board:

[2] `http://www.zemax.com/products/opticstudio`
[3] DAC: Digital to Analog Converter
[4] ADC: Analog to Digital Converter

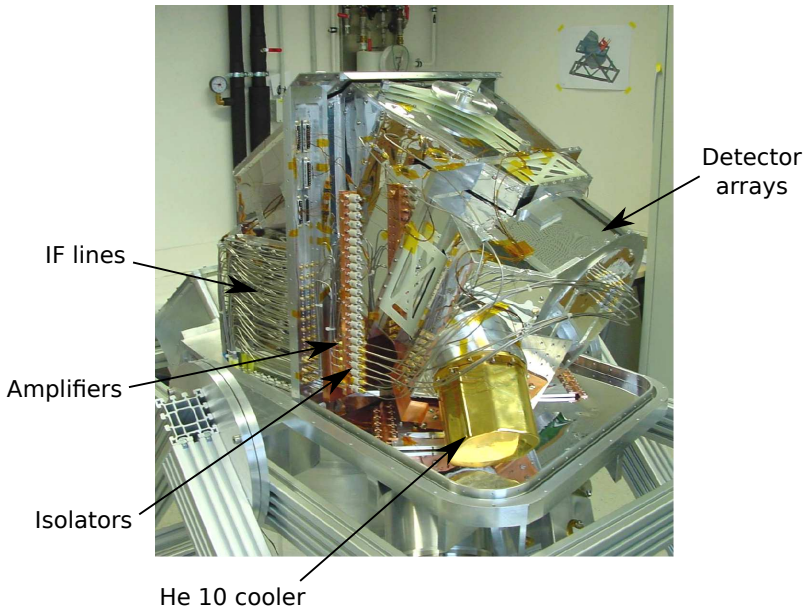

FIGURE 2.3— Cryostat (open) with the He 10 sorption cooler installed.

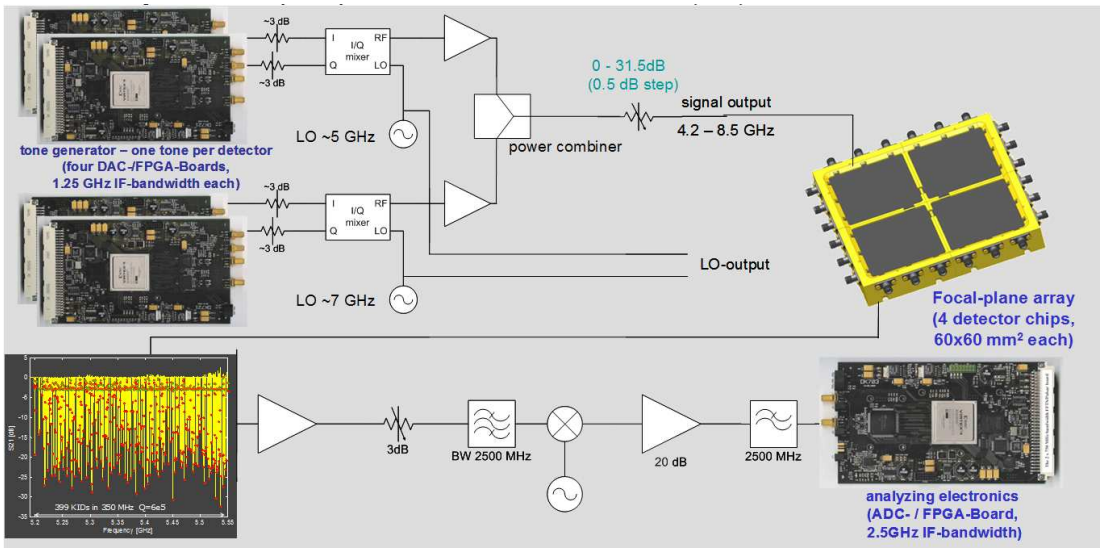

FIGURE 2.4— Read out schematic. The up-converter boards are at top left, the down converter boards at bottom right and the detector at top right.

1. Up-converter board: two separate computer controlled synthesizers, four RF

filters, two amplifiers, two IQ-mixers and a computer controlled attenuator.

2. Down-converter board: provides two separate down-converter circuits, each with a computer controlled synthesizer and attenuator, a low-pass filter and an amplifier.

A schematic of the readout principle is shown is figure 2.4.

Furthermore, one the amplifiers of the up-converter board is a Low Noise Amplifier (LNA), which is located at the 1K stage of the cooling system. The LNAs were manufactured by Caltech MMICs and can produce an amplification higher than 25 dB with a noise contribution of less than 7 K for the IF working band (4 – 8 GHz) with a power dissipation of roughly 5 mW. For the power supply of the LNAs an electronic circuit with 72 channels (three per amplifier) was designed in order the meet the specifications of each amplifier.

2.2 ZEMAX software

2.2.1 What is ZEMAX?

Zemax is a professional software that can model, analyze and assist in the design of optical systems. It has a spreadsheet interface with which the user can define the design parameters of the different elements of the system, and also a set of menus where the general parameters of the system to be modeled can be introduced (like the frequency, the field of view, the units, etc.) (Zemax manual 2011).

2.2.2 Optimization

Zemax also has powerful tools for the optimization of optical systems. Starting with a reasonable optical design, it can be significantly improved under given constraints and/or requirements that the user can define.

In order to optimize a system, Zemax uses a merit function (MF) which has a spreadsheet interface, similar to the one for defining the system elements. The MF is a numerical representation of how closely an optical system meets a specified set of goals. Zemax uses a list of operands which individually represent different constraints or goals for the system. Operands represent goals like image quality, magnification, position of the elements and many others. In the spreadsheet the user can also define a weight for each operand according to the priority that this goal or constraint has in the overall system; the software computes the optimization algorithm according to these weights. The MF is proportional to the square root of the weighted sum of the squared differences between the actual and the target value of each operand in the list. Since the optimization algorithm tries to minimize the distance between the real and target value, the ideal value for each distance operand would be zero, which

would mean that the real value exactly matches with the target value. In general, the MF should be a representation of what the user wants the system to achieve (Zemax manual 2011). Zemax provides a default merit function (DMF). However, when the design is complex, with some specific goals, and thus, the list of constraints is rather large, the MF has to be modified and some more operands have to be added.

For more information about the merit function and how it works a detailed description can be found in the ZEMAX manual (Zemax manual 2011).

2.2.3 Surface definition

Zemax models many types of optical components. These include conventional spherical glass surfaces, plus aspherical, toroidal, cylindric and other surfaces. The user can easily define them in the Lens Data Editor spreadsheet. For a standard surface it is required to define, besides the name of the surface, the radius of curvature (infinity if it is flat), the conic constant and the thickness, which is the distance between the defining element and the next one. For other surfaces more parameters are necessary; some of them can be defined in the Lens Data Editor as well, and in others, like in the polynomial surfaces, they have to be introduced in the Extra Data Editor.

Extended Polynomial Surface

Among all the surfaces that Zemax offers, the extended polynomial surface was selected for our design. According to Stark & Graf (2013), extended polynomial surfaces have a superior performance for systems working in the quasi-optics regime (longer wavelengths than the real optical range).

These surfaces are aspheric surfaces without rotational symmetry. They are generated by a standard, radially-symmetric conic surface to which polynomial terms are added; the terms are of the form $A\,(x/g)^m\,(y/g)^n$, where A is a coefficient, g is a normalization and m and n range over the positive integers (Stark & Graf 2013).

With the polynomial terms it is possible to give the surface a certain shape according to our requirements and therefore, the aberration can be significantly corrected. Without this kind of surface it would be extremely difficult to achieve a satisfactory performance for system like ours, and in general, a complex system with a large list of constraints. All the polynomial coefficients have to be defined in the Extra Data Editor.

The specific surface shape is of the form:

$$z \;=\; \frac{cr^2}{1+\sqrt{1-(1+k)c^2r^2}} \;+\; \sum_{i=1}^{N} A_i E_i(x,y) \tag{2.3}$$

where c is the curvature (the reciprocal radius), r is the radial coordinate, k is the conic constant, N is the number of polynomial coefficients in the series, and A_i is the

coefficient of the i^{th} extended polynomial term. The polynomials (E_i) are power series in x and y, with two first-order terms (x and y), three second-order terms (x^2, y^2, xy), four third order terms etc.. The coordinates x and y are divided by a normalization radius, therefore the polynomial coefficients are dimensionless (Zemax manual 2011).

2.2.4 Tools of analysis

Zemax has a large number of tools to study and analyze optical systems. Among them, the following three ones were mainly used in our case. All of them are based on geometric optics, which in general terms can be considered a good approximation.

Point Spread Function

The diffraction of light, even in a perfect optical system, leads to the formation of a disk, the so-called Airy disk, when a point source such as a star is observed. The size of the Airy disk defines the smallest area to which a lens or mirror can focus a beam of light. The resulting intensity distribution in the image plane is generally called the point spread function (PSF). It widens the irradiance distribution from a single point source in object space such that it is spread over the image plane.

Strehl Ratio

In a real optical system, the irradiance distribution that results from a single point source in object space is not only affected by diffraction, but also by imperfections in the system, leading to aberration. The Strehl ratio is a measure of the quality of such an optical system. It is defined as the ratio between the peak intensity of a point source observed in the detection plane and the theoretical maximum peak intensity of a perfect imaging system working at the diffraction limit.

Spot Diagram

One of the most basic analysis features in Zemax is the spot diagram. This feature launches many rays from a single source point in object space, traces all the rays through the optical system, and plots the (x, y) coordinates of all the rays relative to some common reference. The spot diagram is a collection of points, where each point represents a single ray. There is no interaction or interference between the rays. The spot diagram is a very efficient way to show the effects of the geometric aberrations of the system[5] (Zemax manual 2011).

In order to quantify the system quality with the spot diagram, the reference ellipse for the Airy disk can be added to the diagram; in this way, the geometric aberrations can be compared to the diffraction limit.

[5] `http://kb-en.radiantzemax.com/Print50255.aspx`

2.2.5 ZEMAX and our system

As it was previously mentioned, our camera works at the frequencies of 345 and 870 GHz and, although the working frequency has to be defined in Zemax, the system is studied and analyzed under the geometric optics standard, without simulating Gaussian beams. In our case the geometric optics standard still can be considered a good approximation since the scale of the optics is much larger compared to the wavelength (at least 3 orders of magnitude). When the optics scale and the wavelength are comparable, diffraction effects become significant and therefore Gaussian beam simulations are required.

Nevertheless, in order to be sure that our system works properly, some simulations for a few pixels (field positions) were performed with the UFO software[6] once the final system was achieved. The UFO software works with Gaussian optics propagation, and it could be seen that the system behavior was also satisfactory. Therefore it can be concluded that the Zemax analysis tools based on geometric optics gives reliable information about the system behavior, as expected.

2.3 Optics design

In the introduction of this chapter (section 2.1) the main goals that our camera has to achieve were defined, they were mainly related to the frequency, FoV, magnification and pixel spacing. However, there are more goals that the final system has to reach and also some constraints which have to be taken into account for designing and implementing the system. All of these requirements have to be introduced in the merit function for a proper system optimization. Our system should have:

1. The final beams (beams hitting the detector plane) parallel in order to obtain a proper performance of the hyper-hemispherical lenses located before the detectors (Baryshev et al. 2011). These lenses focus the light to the KID slot antennas.

2. Significantly low aberration in order to achieve a diffraction limited system over the whole required FoV.

3. Less than 10% FoV distortion in order to avoid a large degradation of the image.

4. Size and shape of the overall system must fit in the APEX Cassegrain cabin. This requirement is one of the most critical. The Cassegrain cabin is roughly a cylinder of ~ 3.9 m diameter and ~ 2.0 m height. Since a significant part of it is occupied by other receiver systems, to build a complex system like A-MKID that fits in the remaining space requires significant effort.

[6] Own software developed by Dr. Stefan Heyminck, Max-Planck-Institud für Radioastronomie.

2.3.1 Definition

Our system is composed mainly of reflective elements (mirrors); no other options were considered due to beam sizes and also the remaining space in the Cassegrain cabin into which the system has to fit.

However, regarding the last optical element before the image plane, the use of a lens (dielectric) could be considered, widely used in cameras similar to ours (Fowler et al. 2007; O'Sullivan et al. 2008; Siringo et al. 2009, Sayers et al. 2010).

As a first attempt the use of a lens was studied, and even some test in Zemax with satisfactory results were performed. Using a lens as the last optical element has some advantages (Lamb 2001):

1. Lenses are in general less stringent than mirrors (not at the edges); and beams can be easier collimated before hitting the detector; this would also imply that the aberration problems can be easier corrected.

2. Lenses do not change the direction of propagation of the beam, and being the last element (and part of the cold optics) may make the cryostat design easier.

3. Lenses are axisymmetric elements, which makes their alignment easier.

However, the use of a lens as the last element also implies some issues (Lamb 2001):

1. Losses and dielectric constants are frequency dependent, and consequently, the required thickness for a specific lens also depends on frequency (besides the material properties). In our system, which works at two different frequencies, this could imply a serious problem in its optimization. The optimum material in order to minimize the absorption losses (to reduce the lens thickness) may not be the same for the two frequencies; and in case of using the same material, the optimum thickness would change for each frequency. This would in any case significantly increase the absorption losses, at least for one of the two frequencies.

2. Normally reflection at the dielectric surfaces is significant, and therefore an anti-reflection coating is usually needed. This again introduces some problems: first, the coating may increase the diffraction index, causing astigmatism and cross polarization, and the corresponding loss. Second, since it is part of the cold optics, the compression factor of lens and coating is different and may be damaged in the cold state. And third, also here the optimum material for the coating would change its properties with frequency, which again would introduce a problem since the system would have only one lens with one entire anti-reflection coating.

Due to the issues listed above the idea of using a lens as the last optical element was finally rejected. Therefore a purely reflective optical system was designed.

Regarding reflective elements (mirrors) it is important to mention that:

1. Losses in mirrors are lower than in lenses (throughput is maximized) and also the VSWR (Voltage Standing Wave Ratio), which is inversely related to the return losses, is much lower than in lenses (Lamb 2001).

2. However, the asymmetry created by off-axis mirrors produces intrinsically some losses, which may introduce some difficulties in the optical alignment. Also, the fact that mirrors change the direction of propagation of the beams can make the cryostat design more complicated when a mirror is used as the last optical element.

Mirrors, in particular when they are used as last optical element, introduce some disadvantages; however, these are significantly less problematic than those introduced by a lens.

Therefore, our optical system is purely reflective, which indeed makes our design remarkably novel, since purely reflective systems with similar characteristics have not been reported in the literature; the only exception being the SCUBA-2 optical design (Holland et al. 2013). However, some differences between the optical design of SCUBA-2 and our design have been found:

1. The field of view achieved by SCUBA-2 ($\simeq 8\ x\ 8$ arcmin) is roughly half of the FoV of our design in each dimension and therefore covers a quarter of the area.

2. The working frequencies of SCUBA-2 are 353 GHz (850 μm) and 667 GHz (450 μm); it can be seen that the higher frequency is lower than our higher frequency (857 GHz, 350 μm), and therefore the SCUBA-2 design is less critical in terms of aberration (with higher frequency the Airy disk becomes smaller and therefore more effort is needed to achieve a diffraction-limited system).

3. The SCUBA-2 design is composed of nine optical elements and, as it will be seen, we reached a more compact solution using only six elements (five active ones).

In order to make the calculations easier, an even number of mirrors was the requirement to convert the focal plane of the telescope (Cassegrain focus, after the sub-reflector) to another smaller one. With an odd number of elements the same operation could be done but it simplifies the initial design if the system is treated as follows: If one starts in a focal plane, normally after a reflection in a curved mirror, an aperture plane is found, and then after a second reflection (in another curved mirror) a focal

plane is found again, smaller or larger according to the magnification (ratio between the focal lengths of the mirrors).

The simplest idea was to only employ two mirrors, but it was rapidly rejected for several reasons. First, to get the required magnification in only one step causes significant aberration problems in the final focal plane. And second, there is not too much space left for the window of the cryostat (section 2.1), which in this case should be in the aperture plane between the first mirror and the Lyot stop (section 2.3.5). It is important to mention that the place where the window of the cryostat is located (aperture or focal plane) cannot be larger than $\simeq$ 100 mm (radius) because of the cryostat construction constraints, and in this design with only two elements it would be lager.

The next step was to increase the number of mirrors to four or six. Some simulations with both cases were done and to use four mirrors was finally decided for several reasons. First, it is a more compact design with less elements, which ultimately means a cheaper design. Second, with four mirrors (in two steps) and using polynomial surfaces (section 2.2.3) the required magnification can be achieved with significantly low aberration. Some aberration problems introduced by the first pair of mirrors can be compensated (corrected) with the second pair; with six mirrors the aberration problems were the same or even larger. And third, with four mirrors an intermediate focal plane can be found where the window can be put with the size required by the constructions contraints for the cyrostat.

Therefore the starting point was a simple design with four elliptical mirrors (conic constant $= -1$) and in two dimensions, the height and the width of the cabin, but not the depth. Later, after some optimization loops, some flat mirrors were introduced in order to fit the design into the cabin and consequently the third dimension was used.

For this first design, the radius of curvature of the mirrors and the corresponding distances between them were calculated according to the required magnification at the detector plane and at the intermediate focal plane (where the cryostat window is). Hereafter, M3, M4, M5 and M6 will be the nomenclature used for the four corresponding mirrors; M1 and M2 correspond to the main dish and the sub-reflector, respectively. The starting values are listed in the following enumeration. It is important to mention that some other combinations surely exist which could be used as a starting point, agreeing with the magnification requirements.

1. M3: f2000, radius = 4000 mm
2. M4: f1000, radius = 2000 mm
3. M5: f750, radius = 1500 mm
4. M6: f400, radius = 800 mm

Hence, the magnification reached in the intermediate focal plane (after M4) is $2000/1000 = 2$ and the one introduced by the second pair (M5-M6) is $750/400 = 1.875$. Therefore, considering an ideal system the total magnification achieved would be 3.874, which is close to our goal (magnification $\simeq 4$) and enough for our requirements. In order to obtain this required behavior in terms of magnification, the elements needed to be separated according to their focal lengths.

1. Distance M3 - M4: 3000 mm
2. Distance M4 - M5: 1750 mm
3. Distance M5 - M6: 1150 mm
4. Distance M6 - Image: 400 mm

It is important to notice that these calculations are somehow approximated. First, there was also a slight magnification introduced between M4-M5 which was not taken into account in the calculation. Second, our mirrors were off-axis, since it is the only way to build such a system with reflective elements, and therefore, depending on the angle offset applied to each element, these calculations can slightly change. Finally, there are also some secondary effects that the elements introduce which could not be controlled in this first approximation. However, these numbers were enough as a starting point in ZEMAX. As previously mentioned, a system which approximately matches our constraints is needed in order to introduce it in ZEMAX and to work on it.

2.3.2 Introduction of our system in ZEMAX

Once the radius of curvature and the distance between the elements were known, they could be easily introduced in the ZEMAX Lens Data Editor interface. However, there are two parameters which have yet to be defined: the decenters of the mirrors in order to make them off-axis and the conic constants.

In order to create an off-axis mirror, two ways can be used: The first option is to apply a tilt to the mirror, and therefore an angle is created between the incoming and outgoing rays. The second option, valid in our case since elliptical mirrors are used, consists of applying a decenter to the mirror; this provokes that another part of its elliptical surface, instead of the symmetric part around the vertex, is illuminated; in this way the mirror becomes asymmetric, and consequentially an angle is created between the incoming and outgoing rays. According to Stark & Graf (2013), for long wavelength optics (as in our case) the second option is the most used one, because jointly with the extended polynomial surfaces accurate responses can be achieved for

this frequency range. Therefore, in our case, for a better behavior of the system, the second option was selected.

For the initial design some decentrations (decenters in the Zemax nomenclature) were applied to the mirrors in order to have a good starting point regarding the global shape of the system; this means that the positions of the mirrors are according to the size of the cabin.

1. M3 decenter: 800 mm
2. M4 decenter: 600 mm
3. M5 decenter: 450 mm
4. M6 decenter: 450 mm

As previously mentioned, once the decenters are introduced the distances between the elements have to be re-adjusted in order to find the required system behavior.

The second parameter to be defined was the conic constant of our mirrors. Since our first assumption was to consider completely elliptical mirrors the conic constant was fixed to -1 for all of them.

Figure 2.5 shows this starting design. It can be seen that only two dimensions have been considered for that. The figure also shows that this design is physically not feasible (e.g., M4 is above the main dish). Nevertheless, as will be seen later, introducing two flat mirrors, one after M3 and the other one after M4, can fold the system in such a way as to fit it to the cabin; therefore it is important to keep roughly this system shape.

Fields and frequency definition

Once the elements of the system are defined, the frequency under which the system is studied has to be introduced. There is a menu in Zemax where the user can introduce the wavelength in micrometers. For the development and analysis of our optical design, the high frequency was selected (857 GHz, corresponding to 350 µm wavelength); this is because the high frequency is the most critical one in terms of aberration. This can be easily understood with equation 2.4, which shows the relation between the wavelength and the radius of the Airy disk (this is the distance between the center of the spot and the first null of the diffraction pattern).

The relation between wavelength and the radius of the Airy disk is:

$$r \approx 1.22\lambda N \tag{2.4}$$

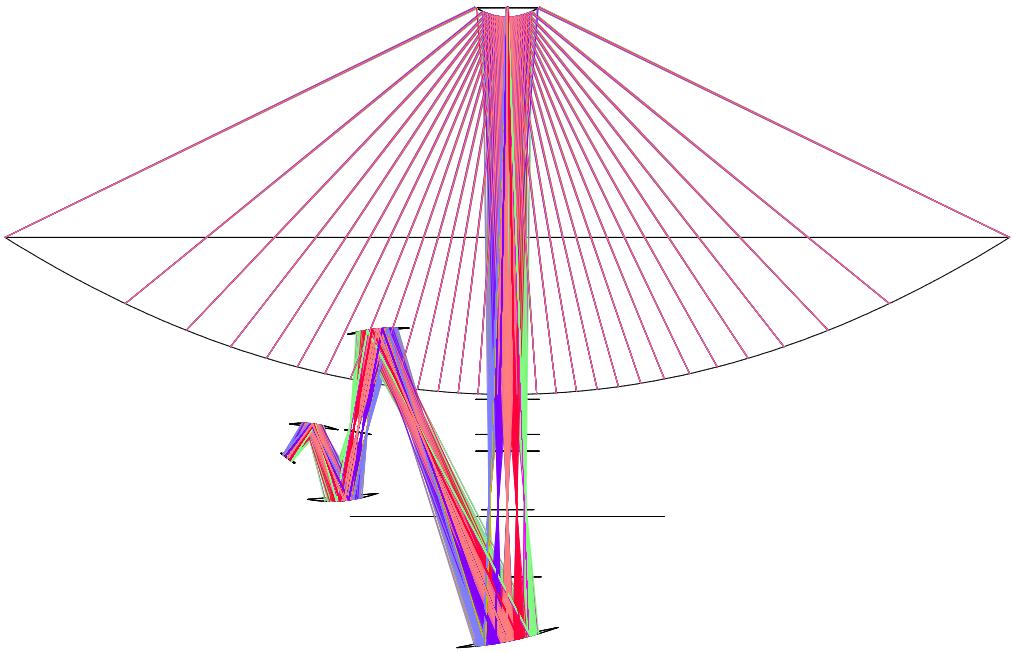

FIGURE 2.5— View of the telescope and the optical elements in the starting 2D format (before any optimization).

where N is the f-number (focal length divided by diameter of the aperture; in the case of the APEX telescope this value is 8). The radius of the Airy disk is proportional to the wavelength (λ); consequently, lower wavelengths (or higher frequencies) have a smaller diffraction pattern (smaller Airy disk) and therefore aberration becomes more critical if a diffraction-limited system is required.

In order to execute the simulations in ZEMAX the FoV also has to be defined. There is another menu where the user can introduce up to 12 field points (in two coordinates: x and y in angle units) according to the required FoV and the measurement points that the user wants to use. 12 fields in some different locations, covering the 16 arcmin of FoV, were defined. It is important to cover homogeneously the whole FoV (not only the center and the edges) in order to know the behavior of the system across the complete FoV. Figure 2.6 shows the field points defined for our measurements; they consist of eight field points along the edges of the FoV, a central point and three points around it. With all these points a reliable response over the whole FoV is expected.

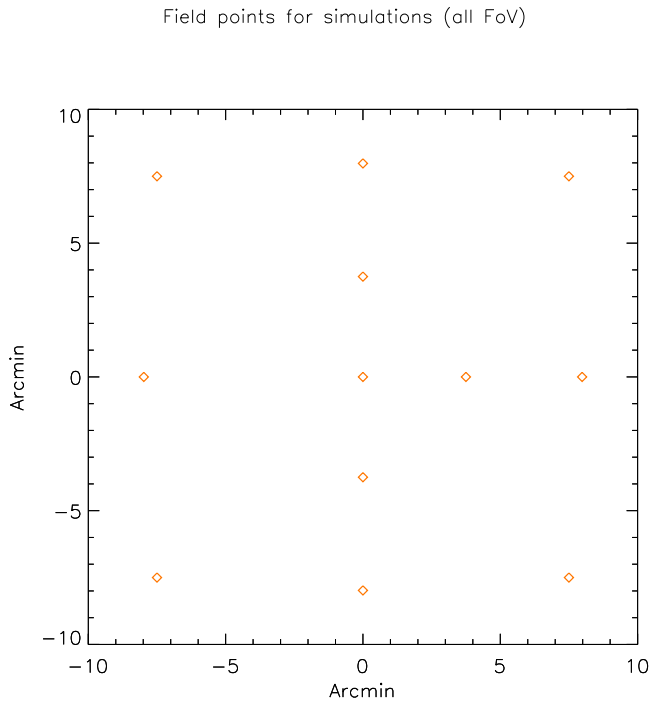

FIGURE 2.6— Field points under which the system was studied. The field points are covering the complete FoV ($16'$).

2.3.3 Building the Merit Function

Once the initial design is defined, the merit function (MF), which has to take care of all the goals and constraints of our design, has to be built. As it was previously mentioned, ZEMAX has a default merit function (see section 2.2.2), however, for our complex design it is not sufficient. Our system has some specific restrictions and aims, which would be never reached using only the default merit function (DMF).

ZEMAX offers more than 200 operands with which almost every aspect related to the design can be controlled. It is important to add the necessary number of operands according to your goals and constraints, but not more, because otherwise more time is spent in each optimization loop. Also, using more operands than strictly necessary may force the software to do something unwanted and it would therefore be very difficult to obtain a final solution.

The sets of operands introduced for starting the optimization process are men-

tioned in the following enumeration.

As will be seen later, there are some more operands that had to be introduced after some optimization loops.

At the beginning, the operands according to the goals that we want to achieve and the operands regarding the constraints that *a priori* should be taken into account are added to the merit function. However, it is difficult to guess in which direction a system will turn, and which unwanted problems may appear after some optimization loops. Indeed, if the initial design and the merit function are well defined, the number of issues which are going to appear is significantly reduced. Nevertheless, when a really accurate response is required, as in our case, some abnormalities are going to appear during the optimization process; and therefore some operands in order to solve them have to be introduced as the optimization progresses.

1. Operands regarding the position of the elements: The first kind of operands added were those related to the position of the mirrors. The position of the elements, while optimizing, has to be restricted because if we let ZEMAX optimize using the MF without these constraints a different geometry, which does not match the specifications, could be reached. The operands used for that were GLCA, GLCB, GLCC, GLCR, GLCX, GLCY and GLCZ.

2. Operands regarding the parallel final beams (see section 2.3): The second issue which had to be taken into account was the position of the final beams; they should be parallel and orthogonal with respect to the image plane (detector plane). For this purpose the operand RAID (see Zemax manual 2011) in the image surface was used. This operand calculates the angle between the incident ray and the normal surface direction. The value of this operand was forced to be smaller than $0.^{\circ}3$ in 16 different field positions covering the entire FoV (in some operands of the MF the user can define an unlimited field position for the operand calculation).

3. Operands regarding the distortion (see section 2.3): As it was previously discussed, one of the main goals is to achieve less than 10% distortion with respect to a regular grid in the image plane (detector plane) in order to avoid a large degradation of the image. For this purpose the operand DISG (see Zemax manual 2011) was used. This operand calculates the generalized distortion in percentage. The value of this operand was forced to be less than 10% in 16 different field positions covering the entire FoV (the same positions as in the previous point).

4. Operands regarding the aberration (RMS radius, see section 2.3): Another important point was to add some operands to correct the aberration in order

to reach a diffraction-limited system. With the default merit function as well as positioning the final beams parallel some part of the aberration is corrected. However, with complex designs it is better to introduce some specific operands for this issue. In order to perform this, the operand RSCH (see Zemax manual 2011) was used. This operand calculates the RMS (root mean square) spot size with respect to the chief ray by means of a Gaussian quadrature method. The value of this operand was initially forced to be smaller than 0.8 in the 16 different field positions; after some optimization loops this threshold was reduced to 0.1 (again for the 16 different fields).

5. Operands regarding the symmetric magnification (working with the ABCD matrix): Another problem which appeared after some optimization loops was that at some point the symmetric magnification (square shape) was lost in the image plane and it got a rectangular shape. This fact was completely unwanted because it means a different magnification in each side of the FoV and thus distortion. With the operand RSCH, already discussed in the number 3 of this enumeration, this kind of distortion can not be controlled. After some optimization tests it was decided to include the operands regarding this issue right from the beginning, since it was almost impossible to recover the proper shape afterwards. In a system without distortion, the chief ray coordinates on the image plane follow a linear relationship with the field coordinate:

$$\begin{bmatrix} x_p \\ y_p \end{bmatrix} = \begin{bmatrix} A & B \\ C & D \end{bmatrix} \cdot \begin{bmatrix} f_x \\ f_y \end{bmatrix} \tag{2.5}$$

where x_p and y_p are the predicted image coordinates and, f_x and f_y are the linear coordinates on the object surface (see Zemax manual 2011). In the MF with the operand ABCD the four values of the matrix can be calculated. If some constraints are applied to the A and D parameters, which in the ideal case are related to variations in the X and Y directions, this problem can be controlled. The ratio between A and D or vice versa (the smaller over the larger) was computed and forced to be lager than 0.8. This means that only a difference of at most 20% between the x and y sides was allowed in the optimization process.

Before starting the optimization some options of the DMF have to be defined as well: the optimization type, the optimization data type and the optimization reference point. A detailed discussion of these points can be found in the Zemax manual (see Zemax manual 2011). For the optimization the type "RMS" was used, which is the most commonly used one. The RMS is the square root of the average value of the squared individual errors[7]. For the optimization data "Wavefront" was selected, which

[7]Mathematically this RMS is called "standard deviation".

measures the aberration in waves. For the reference point "Centroid" was selected. Centroid reference is generally preferred, especially for wavefront optimization.

2.3.4 System optimization

After defining carefully the MF the optimization process was started. Before each optimization loop, the parameters, which are going to be modified in that loop, have to be defined like "variables" in the Lens Data Editor and/or in the Extra Data Editor. Due to the absence of a systematic method to optimize the whole system, our approach was the following: The optimization process was started without any coefficient in the polynomial surfaces (order 0). Then, as the optimization was progressing, the corresponding coefficients to increase the polynomial order which models the surfaces were added. The order was increased progressively, from order 0 (no coefficient) to fourth order (14 coefficients), with the intermediate steps of first order (two coefficients), second order (five coefficients) and third order (nine coefficients). After reaching the fourth order some test were done with fifth order, but no real improvement could be noticed; therefore, 14 coefficients, corresponding to the fourth polynomial order, was the final decision.

Optimization is a complex and delicate process. It can happen in the optimization (loop after loop) that the best response that could be achieved is not the response that the system is ultimately reaching. This is because the optimization function is reaching a local minimum and not the absolute one. If a local minimum is reached in the optimization process, it is important to halt the current step and to move some steps backwards; the more optimization loops are in the local minimum, the more difficult it is to get out from there.

In order to avoid these local minima and to aim always for the absolute minimum, every time that the polynomial order of the surfaces was increased, several optimization loops were done trying to involve all the surface parameters (first some parameters in all the surfaces at the same time, and later with more detail in each surface). Then, when the optimization could not proceed further, the polynomial order of the surface was increased. At the end, before increasing the polynomial order, all the surface parameters had to be optimized: polynomial coefficients, radius of curvature, distances, conic constants and the decenters.

2.3.5 The Lyot Stop

The Lyot stop is basically an aperture which is important to add, in first order, to fit the beams from our detectors to the telescope, and in second order, to avoid that stray light, out of our beams, is absorbed by the detectors and also to prevent over-illumination in our detectors from the beams themselves.

Passing through the system in the other direction (starting from the detectors), if

the sub-reflector is over-illuminated by the detectors it can produce spillover in the sub-reflector itself and also in the primary mirror (main dish); this is an unwanted effect because "warm temperature" radiation (e.g. radiation from the ground) could be reached by the detectors. On the other hand, if the illumination of the main dish is reduced, also the total system efficiency can be affected.

Although the beams coming from the detectors ($F\lambda$ pixels) can not be simulated by Zemax because the direction defined in the software is "sky to detector", it is important to mention that these beams are significantly truncated by the Lyot stop (roughly 50%) since their beam waists are quite small and they become wider considerably fast.

When the final design is approaching the Lyot Stop has to be added in the last aperture plane before the detector array, this is between M5 and M6 and in the 4K stage. It has to be added when the final design is almost achieved (after optimization) and not before, because the optimization process would try to let pass even the unwanted rays through the aperture of the Lyot stop, a feature that would render the Lyot stop useless.

In order to determine the size of the Lyot stop a compromise between optical efficiency and spillover has to be achieved (the same compromise has to be reached independently from which direction the system is seen).

The Lyot stop is located in an aperture plane, as it happens with the sub-reflector. Since the sub-reflector is not allowed to be over-illuminated by the detectors, the beams should be truncated by the Lyot stop such that an image of the sub-reflector is found at the location of the Lyot stop, obviously with a magnification factor in between but with the same edge taper (look at the system in the direction "detector to sky" to understand this reasoning).

A good approximation of the Lyot stop size could be calculated with Zemax as follows: With the central beam (central field: 0°) and using ray tracing the size of the aperture plane where the Lyot stop has to be located can be measured, and therefore the size of the Lyot stop can be adjusted to the size of the aperture plane. Using the central beam the over-illumination of the sub-reflector is minimized, and also the over-illumination on the detectors.

Figure 2.7 shows the place where the Lyot stop is located, between M5 and M6, and how the size of the Lyot stop matches the size of the aperture plane. It can be seen that the size of the Lyot stop is only large enough to let pass the rays of the central beam (in blue).

2.4 2D-design results

After all the optimization process a 2-dimensional design was achieved that was not 100% in agreement with our requirements and constraints, but it was the closest

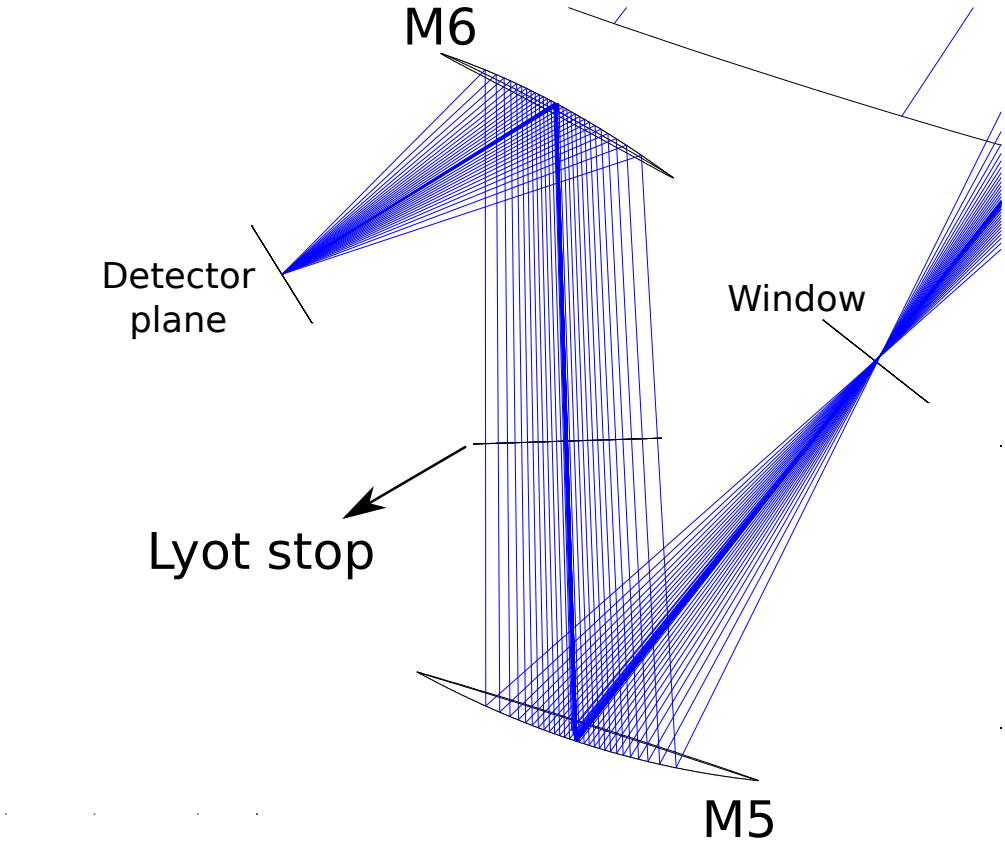

FIGURE 2.7— Central beam rays (in blue) reflected by M5 and M6. The Lyot stop is located between the two mirrors. Note how the rays are passing through it.

approximation that could be achieved.

In figure 2.8 the resulting spot diagrams in the image plane for the 12 fields of figure 2.6 are shown. Although the spot pattern is nearly inside the diffraction limit in all the cases, two problems can be clearly seen:

1. In the edges, in the directions of the field points at $(\pm 0.133, 0)$ and $(0, \pm 0.133)$, spread spots rather than concentrated ones are obtained. This means that the energy is dispersed across this region. This behavior makes the detection worse than if they were more concentrated, even if all the rays are inside the Airy disk.

2. In the corners, basically in the field points corresponding to (0.125, -0.125) and (-0.125,-0.125), the spots are elongated. This means again that the energy distribution is not really uniform and may cause problems in the detection as well.

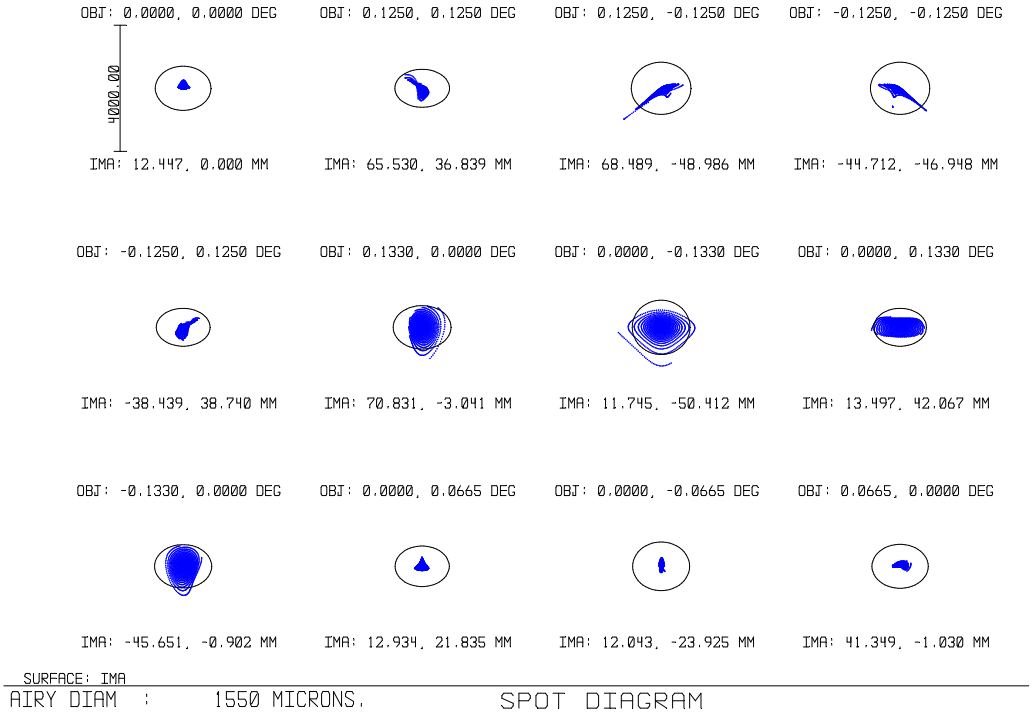

FIGURE 2.8— Spot Diagram of the 2D-design at 350 µm. The first spot is the central ray. The next four are the corners of the FoV, corresponding to the fields at positions $(7.5, 7.5)$, $(7.5, -7.5)$, $(-7.5, -7.5)$, $(-7.5, 7.5)$. The following four are the edges in $\pm x$ and $\pm y$ direction, corresponding to the fields at positions $(8, 0)$, $(0, -8)$, $(0, 8)$, $(-8, 0)$. The last three are some intermediate beams corresponding to the fields at positions $(0, 4)$, $(0, -4)$, $(4, 0)$. The coordinates of the position fields are in arcmin and correspond to the fields of figure 2.6. The black circle corresponds to the Airy radius and below, its size can be read.

Figure 2.9 shows the resulting Strehl ratio in the image plane along the directions $(\pm x, 0)$ and $(0, \pm y)$. Looking at the figure it can be seen that the system is not completely diffraction limited across the entire FoV.

In figure 2.10 the overall optimized 2D system can be seen in the upper panel, and in the lower panel a zoom of the last three surfaces is shown, with the M4, M5, M6, the window, the Loyt stop and the image plane (detector plane). As previously mentioned, this 2D design was not the selected final design: first, because it does not fit into the Cassegrain cabin, which can nevertheless be solved by introducing two flat mirrors; and second, there are evidently still some improvements to be done. Nevertheless, this is a successful intermediate step, and a good starting point for the final 3D model.

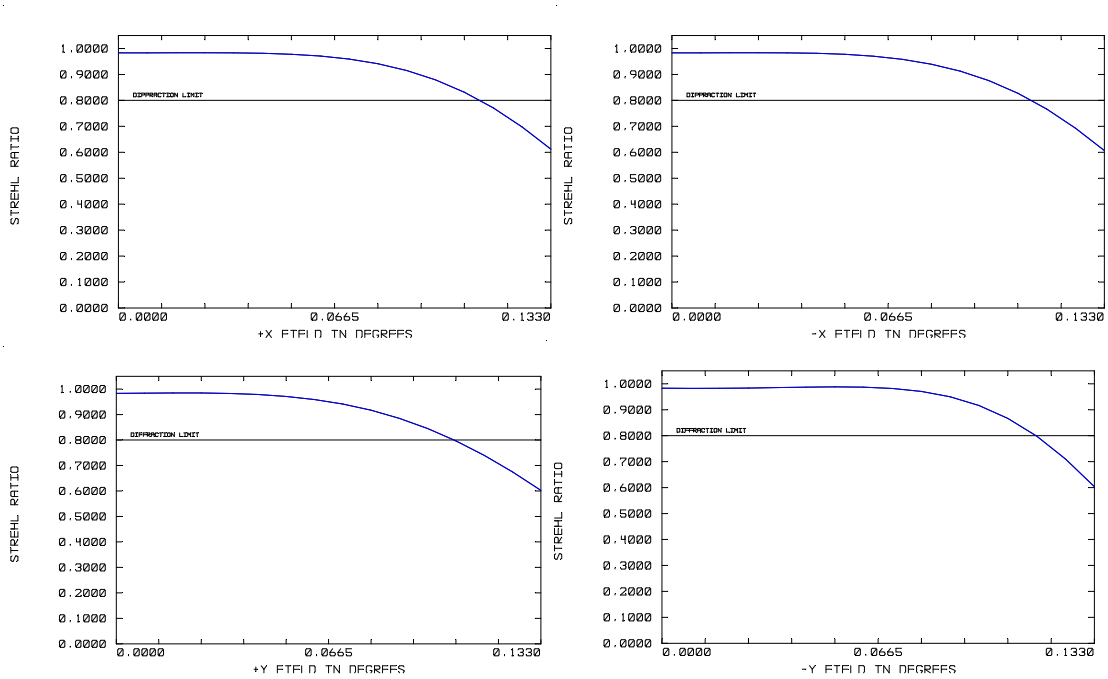

FIGURE 2.9— Strehl ratio of the 2D-design along the directions $(\pm x, 0)$ and $(0, \pm y)$ at 350 µm wavelength. The horizontal black line shows the diffraction limit.

2.5 3D-design

The next step was to add two flat mirrors to our 2D-design in order to fit the system into the APEX Cassegrain cabin, and also not to overlap the system with the rest of the elements that the cabin contains. It is also important to emphasize that adding the third dimension involves to add more degrees of freedom in the optimization, and it could be seen how this significantly corrected the aberration problems (with these extra degrees of freedom the aberration problems introduced by some elements can be compensated with other elements). It will be concluded, after the optimization process, that our final system really reaches all our goals inside the margins and constraints formulated.

2.5.1 Adding flat mirrors

The 2D-model was under the use of two flat mirrors folded into a 3D-model of the APEX Cassegrain cabin. These two flat mirrors were located between M3 and M4 (FM1), and between M4 and M5 (FM2; before the window). To introduce a flat mirror after the window, in the cold optics, was not really an option because it would have significantly increased the size of the cryostat and this would have introduced several

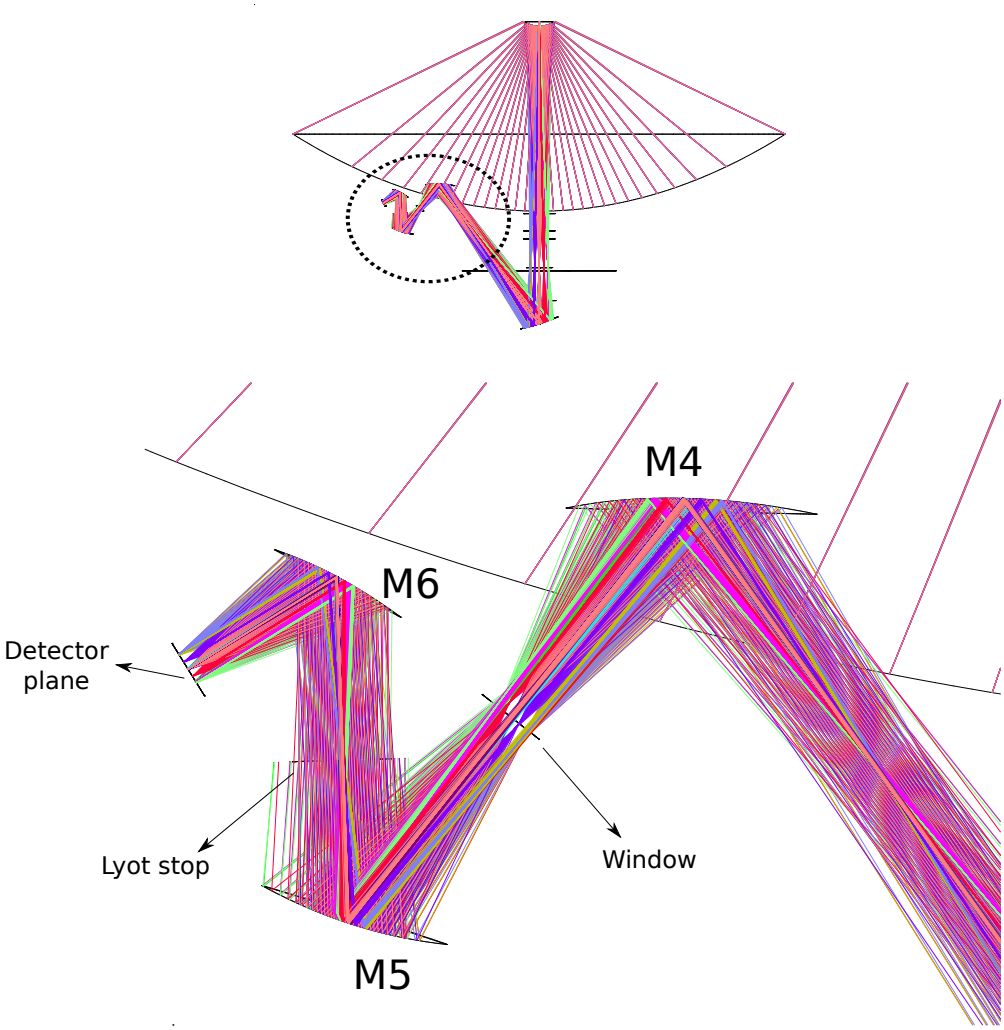

FIGURE 2.10— Upper panel: general view of the APEX telescope with the optical 2D-design (dashed circle). Lower panel: zoom view of the optical 2D-design with M4, M5 and M6; the window, the Lyot stop and the detector plane also shown.

problems: First, it would have been very expensive to manufacture a cryostat of such dimension; second, it would have also been difficult to build it; and third, it would have been very complex to handle such a cryostat, both in the lab for testing and inside the cabin.

In order to optimize the system, almost the same merit function as before was applied. The only operands that needed to be changed were those regarding the

position of the elements, because for this new step in the design the geometry of the system was different. Also the position restriction for the new flat mirrors had to be added. The rest of the operands regarding parallel final beams, distortion, aberration and symmetric magnification remained the same.

In order to achieve a better response the second flat mirror (FM2) was also considered as an active mirror, which means, as a polynomial extended surface. Therefore, the possibility to change its shape with some coefficients was considered in the optimization. This fact introduced even more degrees of freedom to our system, and consequently a better response could be achieved with that. Some attempts were done to consider the first flat mirror (FM1) as a polynomial extended surface as well, however, this option was rejected because it would have increased significantly the price of the of the system (FM1 is two times larger than FM2), and second, it would have introduced difficulties for the alignment of the whole system.

It is important to mention that another problem appeared in the optimization: After some optimization loops the central beam was getting an offset in X direction (relative coordinates with respect to each element). This is because the optimization process tries to reduce the reflection angle between the elements in order to reduce the aberration. It is essential to control this fact in order to properly illuminate the elements, otherwise, since the elements have a specific size, it could introduce losses. Therefore, a compromise between offset and aberration has to be reached.

This issue was controlled and corrected with the operand REAX in the merit function. This operand calculates the real ray position in the local coordinates of the mirror. Thereby, the offset was reduced until 2 mm in M4, 1 mm in M5, and 0.5 mm in M6.

2.5.2 Results

After several optimization loops in this 3D-model (including the correction of the offset) a final design was obtained, where all our goals were achieved well within the margins and constraints. Also, the final design had a geometry which fits into the cabin without overlapping with any other device.

Figure 2.11 shows some views of the final design: The upper panel shows a general view of the telescope and the optics, while the lower panel shows a zoom on the optical design itself (without main dish and sub-reflector); this view is taken from the telescope focal plane (Cassegrain focus) downwards.

Table 2.1 shows the parameters for the final design: The radius of curvature of each mirror, the distances between them and the conic constants. The tilts and decenters applied to each element are shown in table 2.2; these values are relative to the central ray of each surface, which is the way to define the element positions in

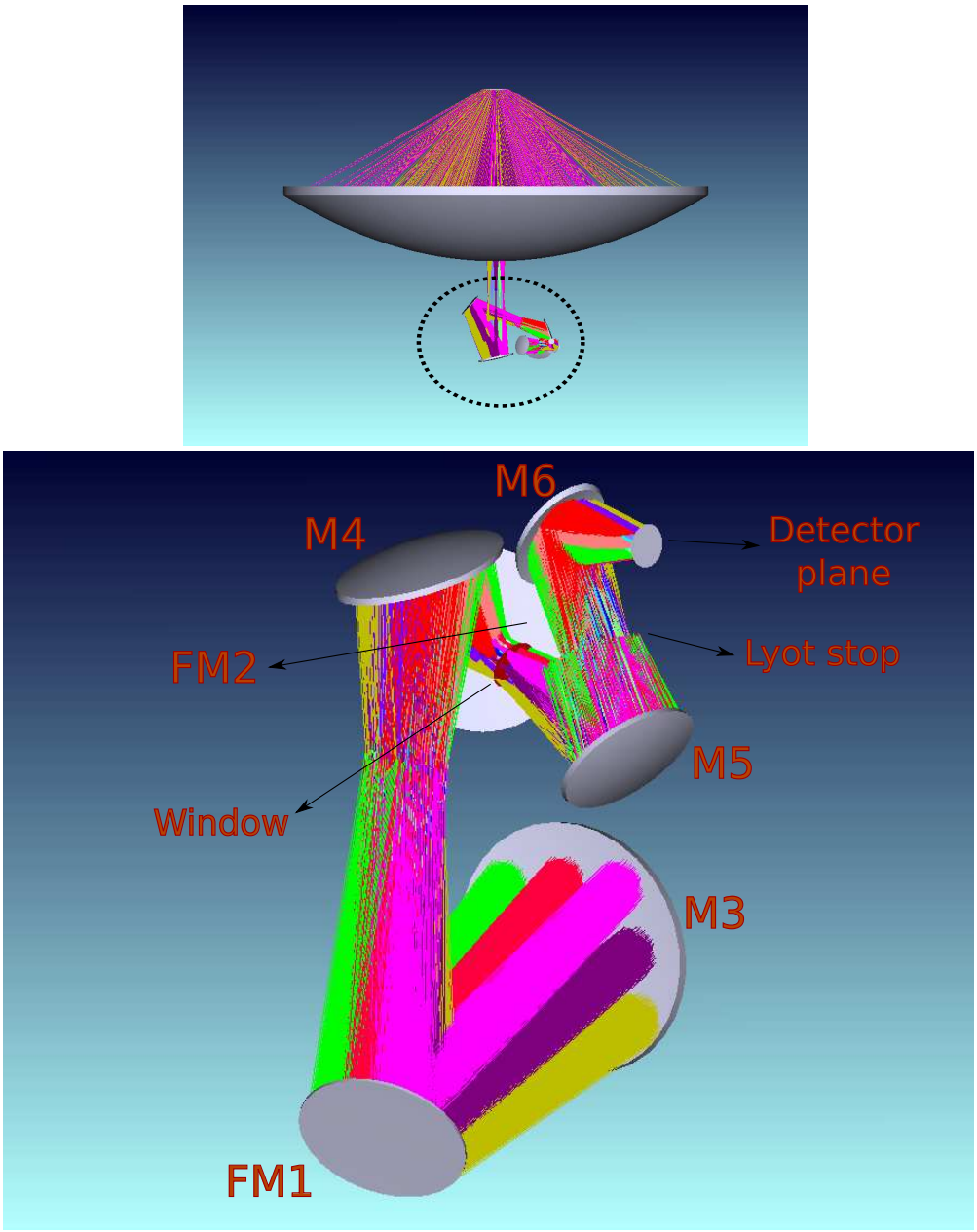

FIGURE 2.11— Upper panel: General view of the telescope with the final 3D-design (dashed circle). Lower panel: zoom onto the final 3D-design; the design is viewed from the focal plane of the telescope downwards.

Zemax; consequently, the coordinate system in Zemax changes with each reflection.

TABLE 2.1— 3D-design parameters.

Element	Radius of curvature (in mm)	Distance to the next element (in mm)	Conic constant
M3	4360	1391.0	2.09
FM1	–	2667.6	0.00
M4	1049	175.8	-0.79
FM2	–	195.0	0.00
Window	–	816.8	–
M5	1293	567.0	-1.06
Lyot stop	–	632.5	–
M6	662	796.4	-0.92
Detector plane	–	–	–

TABLE 2.2— Decenters and tilts for the final 3D-design.

Element	Decenter X (in mm)	Decenter Y (in mm)	Tilt X (in °)	Tilt Y (in °)	Tilt Z (in °)
M3	0.0	-820.4	0.0	0.0	0.0
FM1	0.0	0.0	-22.5	0.0	-10.0
M4	0.0	-493.8	0.0	0.0	0.0
FM2	0.0	0.0	47.5	0.0	-130
Window	0.0	0.0	0.0	0.0	0.0
M5	0.0	-490.4	0.0	0.0	0.0
Lyot stop	0.0	0.0	0.0	0.0	0.0
M6	0.0	407.1	0.0	0.0	0.0
Detector plane	0.0	0.0	0.0	0.0	0.0

[a] The tilts and decenters are relative to the central ray, therefore, the coordinate system changes with each reflection.

The following list shows a review of the achieved system specifications and compares them with the goals defined in sections 2.1 and 2.3:

1. Parallel final beams: In the final design, the angle between the beams (or rays because it is a geometric optics analysis) and the normal surface direction of the detector plane was below $0.^{\circ}3$ for all of them. In fact, the average angle between the beams and the normal surface direction of the detector plane was $\sim 0.^{\circ}185$.

2. Aberration: one of the most important goals was to design a completely

diffraction-limited system. Also for the proper behavior of the detectors, a point-like spot rather than a spread region was required (even inside the Airy disk). This was one of the problems that the 2D-design had (see section 2.4). Figure 2.12 shows the spot diagram of the same 12 field points under which the 2D system was studied (see section 2.4). It can be seen how the system is completely diffraction limited, and also that all the spots are concentrated in point-like circular shapes rather than in disperse regions inside the Airy disk. At the outer points (at the edges of the FoV) the spots are slightly wider but they still conserve the point-like shape. Figure 2.13 shows the spot diagrams of the central field and two more fields (corresponding to positions (7.5,0) and (-7.5,-7.5) of the FoV in figure 2.6) for the 2D and 3D designs; it can be directly seen how the spot diagrams of the 3D design are improved in terms of aberration, especially in the edges (central and bottom case in the figure).

Figure 2.14 shows the Strehl ratio in the directions $\pm x$ and $\pm y$ for the 3D-design (blue lines) and 2D-design (red lines). It can be noticed that the 3D system is completely diffraction limit in the whole FoV while the 2D system, at a certain point, crosses the diffraction limit threshold. Moreover, it can be seen that the response of the 3D model is close to the theoretical maximum (Strehl ratio = 1).

3. Distortion: The requirement was to achieve less than 10% distortion in the detector plane in order to avoid a large degradation of the image. The average distortion achieved was $\sim$ 13%. Due to the geometry and the construction constraints, our goal was slightly surpassed.

   Figure 2.16 shows a model of the FoV distortion on the detector plane (red squares). The estimated distortion value was computed following the Zemax procedure, which compares the positions between a regular squared grid and the real distorted positions after passing the system (red squares in the figure); each real position corresponds to one position on the grid. The calculation was done as follows:

$$\text{Distortion} = 100\% \frac{\Delta_{\text{distortion}}}{D_{\text{grid}}} \tag{2.6}$$

   where $\Delta_{\text{distortion}}$ is the distance of the distorted point from the original grid point, i.e.,

$$\Delta_{\text{distortion}} = \sqrt{(x_{grid} - x_{dist})^2 + (y_{grid} - y_{dist})^2} \tag{2.7}$$

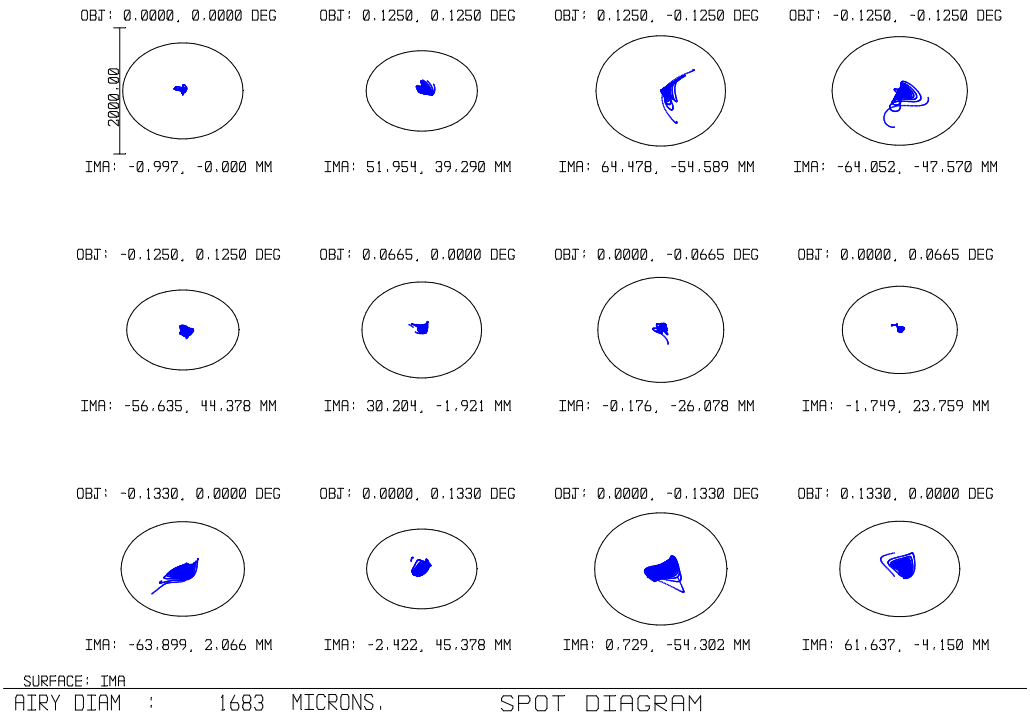

FIGURE 2.12— Spot Diagram of the 3D final design at 350 µm. The first spot is the central field. The next four are the corners of the FoV, corresponding to the position field of (7.5,7.5), (7.5,-7.5), (-7.5,-7.5), (-7.5, 7.5). The following three are some intermediate fields corresponding to field position of (0,4), (0,-4), (4,0). And the last four are the edges in $\pm x$ and $\pm y$ direction, corresponding to the position fields of (8,0), (0,-8), (0,8), (-8,0). The coordinates of the position fields are in arcmin and correspond to the fields of figure 2.6. The black circle corresponds to the Airy radius and below, its size can be read.

and where D_{grid} is the distance of the original grid point from the center of the FoV, i.e.,

$$D_{\text{grid}} = \sqrt{(x_{grid})^2 + (y_{grid})^2}\,. \tag{2.8}$$

Thereby, the distortion is characterized by one value for each grid point. In the histogram of figure 2.15 the distortion distribution of all the grid points is shown. It can be seen that all the distortions are concentrated around a value of 12%. Only 17% of the grid points surpasses the 15% distortion value and none of the points is more than 20% distorted.

Figure 2.16 also shows the full field spot diagram (blue spots) for the same fields as those represented in figure 2.12 but at their real positions in the detector plane.

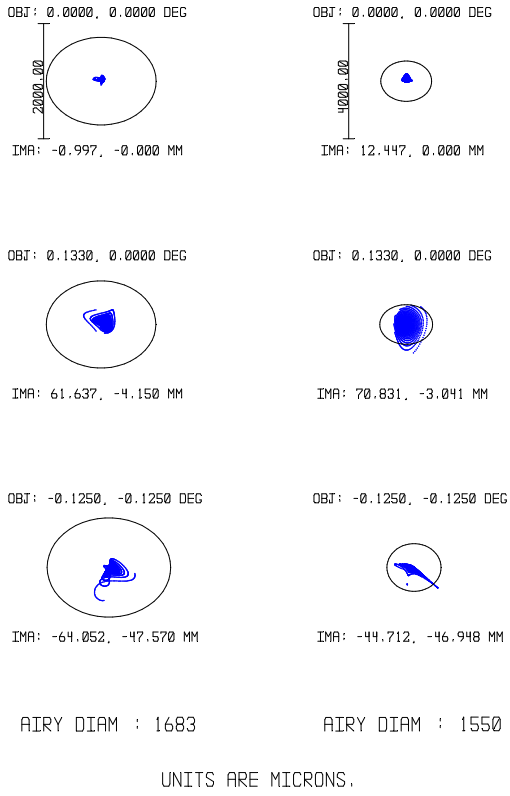

FIGURE 2.13— Spot diagrams of three specific fields of the 2D (right row) and 3D (left row) designs. The fields are: central fields (0,0) (top line) and two fields at the edges, (8,0) (central line) and (-7.5,-7.5) (bottom line). It can be seen how the spots of the 3D design are improved in terms of aberration (smaller and more roundish spots).

With that an estimation of how the beams (the rays in the different field points) hit the detector plane can be seen, and consequently, the shape of the FoV in the detector plane can be understood.

Comparing the model of the FoV distortion (red squares) and full field spot diagram (blue spots) shows that both shapes are in quite good agreement and therefore it can be affirmed that the aforesaid distortion calculation ($\sim 13\%$) is a reliable approximation of the real distortion of our system.

4. Magnification: Using the same tool as before, a model of the FoV of the telescope focal plane (Cassegrain focus) can be computed. Therefore, if we compare the size of the resulting FoV with the size of the FoV-model at the detector plane, the magnification of the system can be estimated. Since the

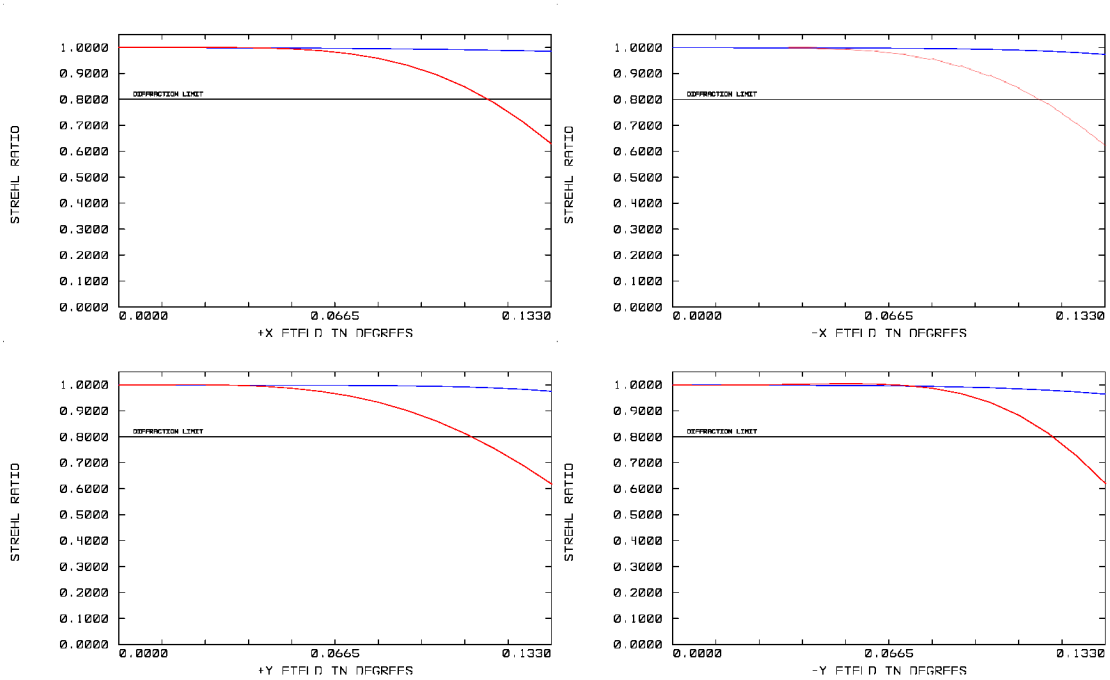

FIGURE 2.14— Strehl ratio of the 3D-design (blue lines) and 2D-design (red lines) in the directions $\pm x$ and $\pm y$ at 350 µm (blue lines). The horizontal black line shows the diffraction limit. While the 3D-design remains always above the diffraction limit, the 2D-design at a certain point crosses this threshold.

system is not completely symmetric two magnification values are obtained, one for each direction (X and Y):

(a) Magnification in X: ~ 3.5.

(b) Magnification in Y: ~ 4.5.

If the average between these two values is computed, we obtain a general magnification of ~ 4, which is roughly 10% larger than the theoretical value (for Fov of $15'$ x $15'$, see section 2.1).

5. FoV: Using the magnification calculated in the previous point, the total size of the FoV in angular units can be computed:

(a) In X direction:

$$117\,\text{mm} \;\text{x}\; 3.5 \;\text{x}\; 2.15\,\text{arcsec/mm} \simeq 14.7' \tag{2.9}$$

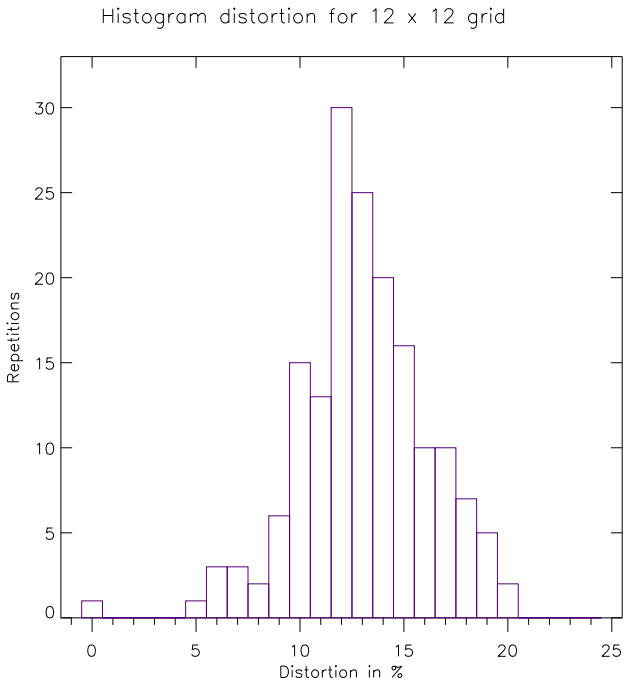

FIGURE 2.15— Histogram of the distribution of the distortion from a regular grid.

(b) In Y direction:

$$117\,\text{mm} \;\text{x}\; 4.5 \;\text{x}\; 2.15\,\text{arcsec/mm} \simeq 18.8' \tag{2.10}$$

where the 117 mm is the edge length of the detector array, 3.5 and 4.5 are the magnification values previously calculated and 2.15 arcsec/mm is the plate scale of the focal plane of the telescope. Despite the different magnification in the two directions, the total FoV covers an area similar to the FoV defined in our initial requirements ($16'$ x $16'$). Therefore, it can be concluded that a very competitive FoV has been achieved for a camera of these characteristics.

6. Pixel spacing: After the calculations done in the introduction of the chapter (section 2.1) and accounting for the constraints of the detector manufacture at SRON, the agreed pixel spacing for the detector plane was: 2 mm for the LFA, and 0.8 mm for the HFA. This implies a pixel spacing in the focal plane of the telescope of:

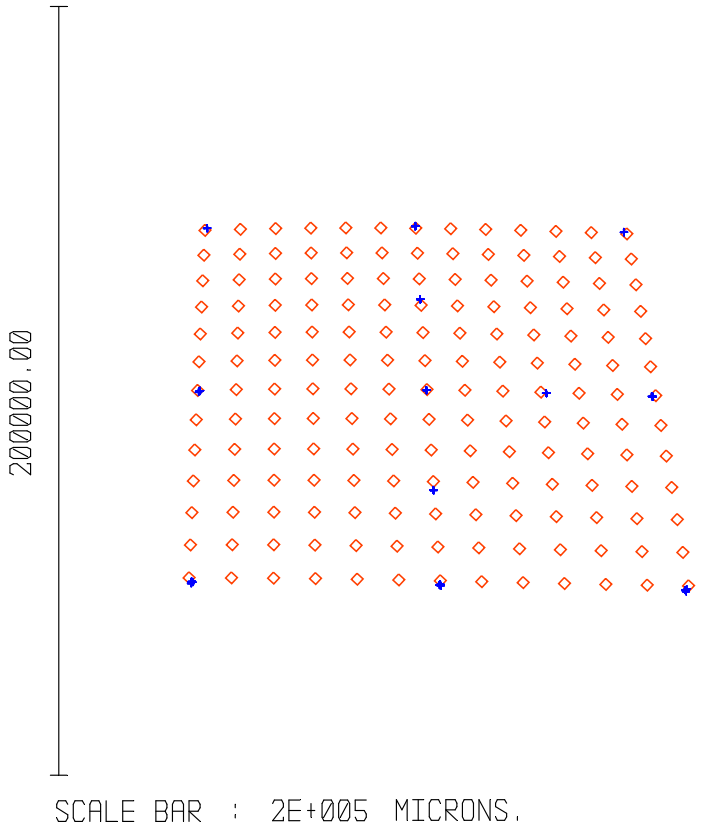

FIGURE 2.16— Full field spot diagram (blue spots) overlaid with the resulting grid distortion (red squares), both in the detector plane. Both shapes are in agreement.

(a) LFA:

- X direction: 2 mm x 3.4 = 6.60 mm
- Y direction: 2 mm x 4.2 = 8.15 mm

(b) HFA

- X direction: 0.8 mm x 3.4 = 2.65 mm
- Y direction: 0.8 mm x 4.2 = 3.28 mm

These distances can also be calculated with respect to $F\lambda$, to see how close they are to the expected pixel spacing ($\sim 1\ F\lambda$):

(a) Low frequency, 345 GHz: ($F\lambda = 6.96$ mm):

- X direction: pixel spacing = $0.95\ F\lambda$

- Y direction: pixel spacing = $1.17 F\lambda$

(b) High frequency, $857\,GHz$: ($F\lambda = 2.8$ mm):

- X direction: pixel spacing = $0.95 F\lambda$
- Y direction: pixel spacing = $1.17 F\lambda$

which is $1.06 F\lambda$ on average for both cases.

Despite the difference between X and Y direction, both values, and in both frequencies, are very close to the expected pixel spacing ($\sim F\lambda$) and therefore, no negative effects can be expected from that.

Closing the section on the system results, it can be concluded that after all the analysis our system successfully achieved all the goals and requirements defined in the specifications. It is true that the average distortion is slightly higher than the initial requirement, but it can still be considered to be within a reasonable error margin.

2.5.3 Study under misalignments

Once the design is ready a study of the response of the system under some displacements and tilts of their elements had to be done. It is important to know the tolerances of the system under misalignments because when the system is physically implemented small misalignment errors are unavoidable; it is almost impossible to achieve a perfect alignment. Also, the movements and vibrations of the telescope can provoke some tiny misalignments.

In order to reduce these problems and to ensure a maximum stability, a compact structure was build into the cabin to ultimately attach the elements to the INVAR cone of the telescope.

Because of the cabin shape and of the design characteristics four blocks were created: The first one was formed by M3, the second one by FM1, the third one by M4 and FM2, and the last one by M5, M6, the Lyot stop and the detector plane. The last block is located in the cold optics and is very compact, because all its elements are inside the cryostat.

Our study consisted of applying a displacement or tilt to one block in one of the three directions (x, y or z), keeping the rest in the same position. Then, the average of the RMS radii of all the fields in the detector plane was calculated. The RMS of each field is computed by Zemax with the spot diagram tool; using ray tracing it calculates the RMS of the resulting spot in the detector plane for each defined field.

This operation was done for each direction and for different values of decenter and tilt. For the displacements the measurements were performed for ± 1 mm, ± 2 mm and ± 5 mm; and for the tilts the calculations were done for $\pm 0.^{\circ}02$, $\pm 0.^{\circ}05$ and $\pm 0.^{\circ}1$.

Figures 2.17 and 2.18 show the behavior of the system under these displacements and tilts for each block. As expected, it can be seen how the average RMS increases as the decenter or tilt value becomes larger. This means that the aberration of the system increases.

It is important to mention that this study is not strictly rigorous, because it is ray tracing based and no diffraction is computed, nevertheless it can give an idea which blocks and which directions are the most critical ones.

Figure 2.17 shows the behavior of the system under the displacements. The displacements are most critical for blocks M4-FM2 and M5-M6, both in Z direction. This means that special attention has to be paid to the alignment of these blocks, especially in the critical direction. Nevertheless, although these are the worst cases, this is not extremely critical either because, first, not more than 1 mm of displacement is expected, and second, no power loss is expected from these misalignments. The RMS radii of the resulting spots are still smaller than the Airy disk radius (see table 2.3), this means that all the power remains concentrated inside the Airy disk (the diffraction limit).

Although no power loss is expected from the optical system with these misalignments, the wider spots produced by them (see table 2.3) affect the proper behavior of the hyper-hemispherical lenses and consequently, the detection on the KIDs; this could lead to a slight fraction of power loss.

Figure 2.18 shows the behavior of the system under the tilts. It can be seen that the applied tilts do not imply big issues for the alignment. The most critical block is M4-FM2 in x-direction, but it is even more benign than the displacement case (see table 2.3).

Table 2.3 shows the resulting RMS radii for the worst cases of the misalignment study; only the values for the central ray and the worst corner are given, and only for the limiting cases of our study: ± 5 mm in Z direction for the M4-FM2 and M5-M6 blocks, and $\pm 0.^{\circ}1$ in X direction for the M4-FM2 block.

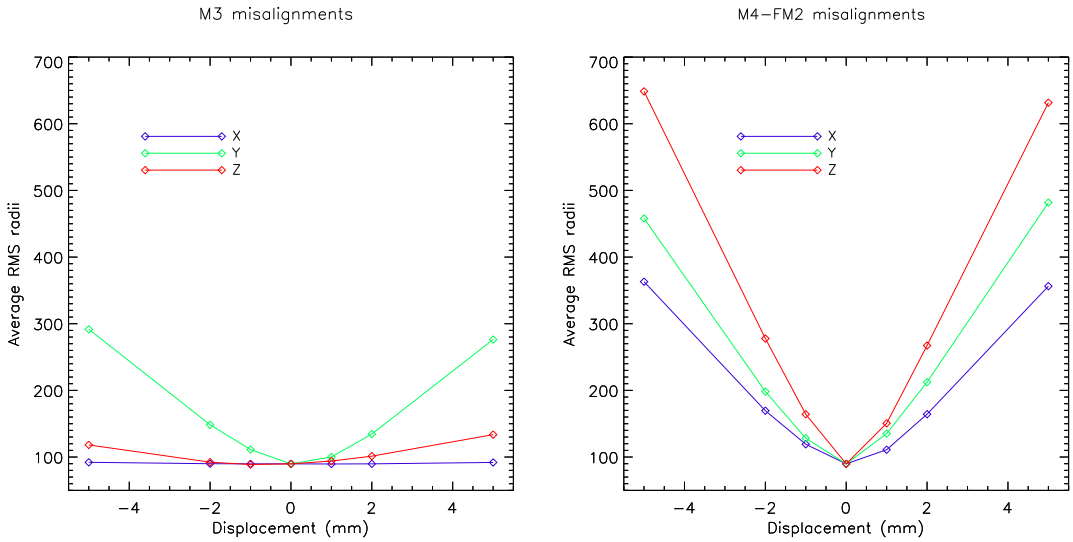

(a)

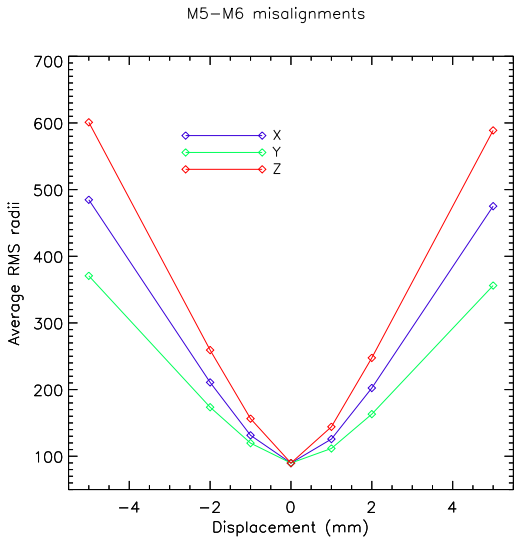

(b)

FIGURE 2.17— Average RMS radii (in µm) vs. displacement in X, Y and Z directions for the blocks M3, M4-FM2 and M5-M6.

TABLE 2.3— RMS radii of the central ray and the worst corner field for the worst cases of the misalignment study.

Position	**M4 - FM2**				**M5 - M6**	
	+5 mm (in Z)	**-5 mm (in Z)**	**+0.1° (in X)**	**-0.1° (in X)**	**+5 mm (in Z)**	**-5 mm (in Z)**
Central Ray RMS (in µm)	639	638	161	173	599	603
Worst Corner RMS (in µm)	709	697	251	255	674	688

[a]The Airy disk radius is roughly $\sim 842\mu m$

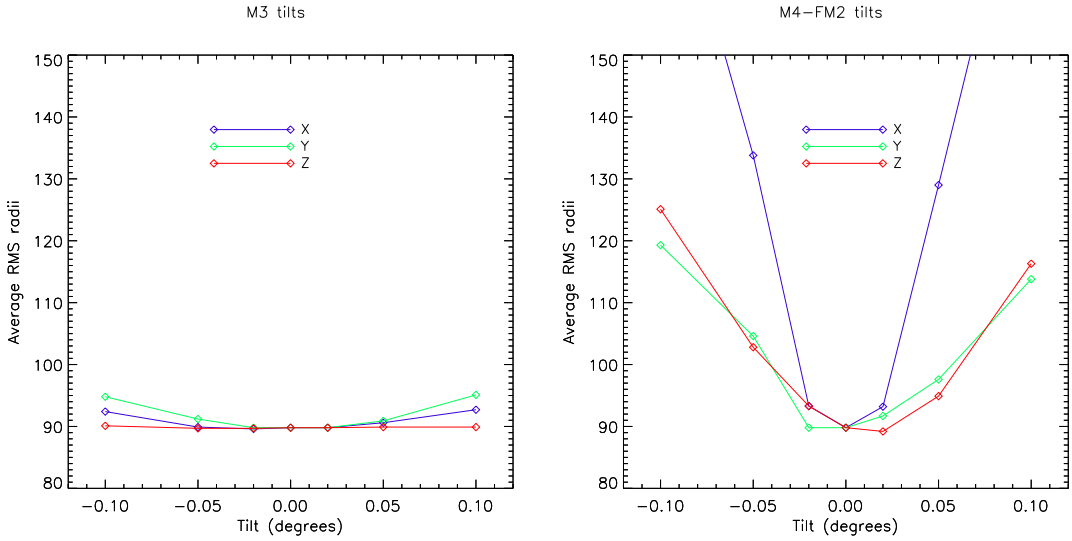

(a)

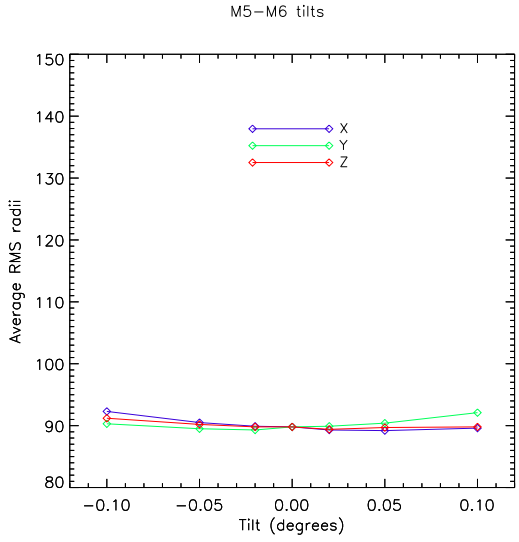

(b)

FIGURE 2.18— Average RMS radii (in μm) vs. tilt in X, Y and Z directions for the blocks M3, M4-FM2 and M5-M6.

Further misalignments

As this study shows, the M4-FM2 block is the most critical component for the alignment of our system. Nevertheless, with the misalignments applied in the study

above the degradation of the system, although unwanted, was relatively smooth; no power loss is expected from these misalignments.

Here, three more cases are added to the decenters and tilts applied to this block. In these cases their values are higher than in the previous study and they are applied together in the three directions; the idea is to figure out how the system behaves under such extreme cases. The tilts and decenters applied are:

1. Decenters (x,y,z) in mm: (+10, -10, 0). Tilts (x,y,z): ($+1^\circ$, $+1^\circ$, $+1^\circ$).
2. Decenters (x,y,z) in mm: (+10, -10, +10). Tilts (x,y,z): ($+1^\circ$, $+1^\circ$, $+1^\circ$).
3. Decenters (x,y,z) in mm: (+10, -10, +10). Tilts (x,y,z): (-1°, -1°, -1°).

In table 2.4 the RMS radii of the central ray and the worst corner are shown; the fractional power loss for each case is also calculated. The fractional power loss is just a rough approximation since it is based on the RMS radius of the resulting spot; therefore, the resulting spot is approximated by a circle which is sometimes far from a good approximation. Nevertheless, it may be used just as a reference for the loss of power, as in our case.

TABLE 2.4— RMS radii of the central ray and the worst corner field for the worst cases of the second misalignment study. For each case the fractional power loss is also calculated.

Position	**M4 - FM2**		
	Case 1	**Case 2**	**Case 3**
Central Ray RMS (radius in μm)	1806	2045	2056
Worst Corner RMS(radius in μm)	2020	2290	2329
Power loss central ray[a]	28%	34%	35%
Power loss worst corner[a]	33%	39%	41%
Airy disk (radius in μm)	856	852	840

[a]Power loss is approximated by the fraction of the resulting spot (using the RMS radius) which is out of the Airy disk (A_D); and it is calculated as $P_L = \frac{(RMS_r - A_D)^2}{(RMS_r)^2}$

Figure 2.19 shows the spot diagram of the central ray for each of the three cases. As expected from the previous calculations, it can be seen how aberration is significant in all the three cases, and also how the system is not diffraction limited anymore; the Airy disk is completely surpassed by the spot diagram in each case.

It is definitively not expected to have such misalignments but it is useful to better understand our system.

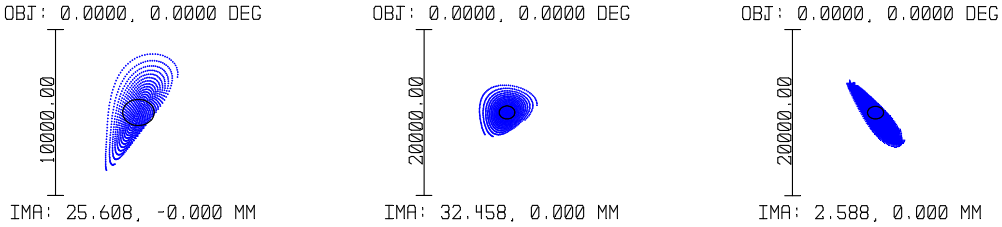

FIGURE 2.19— Central ray spot diagram for each of the three misalignment cases. It can be seen how the diffraction limit (Airy disk) is completely surpassed in the three cases.

2.6 Summary and conclusions

In this chapter the development of the A-MKID optics has been explained; it could be seen how the ambitious camera requirements have finally led us to a very competitive optical system. The main conclusions of our work are:

1. A diffraction-limited system with a FoV of approximately 16x16 arcmin^2 has been achieved for the two working frequencies (345 GHz and 850 GHz).

2. An average distortion of 13% has been achieved in the complete FoV.

3. The system magnification obtained is ~ 4, necessary to achieve the required FoV.

4. A pixel spacing of on average $\sim F\lambda$ was reached, which is a good compromise between throughput, mapping speed and the available resources (see section 2.1).

5. A novel optical system has been developed in order to achieve the previous goals. A purely reflective system has been designed in order to achieve the best response at both working frequencies. The use of lenses requires an anti-reflection coating, but it is almost impossible to optimize the coating for two frequencies at the same time. No other optical design with similar characteristics has been reported in the literature.

6. The optical elements used are:

   - Four elliptical mirrors modeled by extended polynomial surfaces (M3, M4, M5 and M6).

   - Two flat mirrors (FM1 and FM2); FM1 is active and modeled as well by an extended polynomial surface.

   - A Lyot stop, which defines the illumination at the telescope's sub-reflector in order to avoid stray light in our detector plane.

7. A study of tolerances to misalignments has been performed. In order to simulate the real scenario in the telescope Cassegrain cabin, the system was divided into three blocks (M3, FM1, M4-FM2 and M5-M6) to which some tilts and displacements were applied. The system can afford misalignments around 5 mm or $0.^{\circ}1$ in all the blocks without a significant response degradation (see section 2.5.3). The study also reveals that the most critical block is M4-FM2.

3

A-MKID: first commissioning

3.1 Introduction

The first commissioning of the A-MKID camera took place in December 2013. The installation and commissioning were performed by the developing team from MPIfR and SRON with help from the APEX staff.

With some effort the installation was successfully completed; the cryostat (with the detector and the cold optics), the electronic modules, the warm optics and the structures to handle all of these were placed in the Cassegrain cabin of the telescope.

However, some problems arouse during the installation and commissioning; some of them could be fixed and others remained to be solved. Here the most important ones are listed:

1. The cooling: One of the most important issues that occurred was a problem with the cryostat cooling. Due to a thermal contact inside the cryostat, the HFA (High Frequency Array) never reached operation temperature and was completely blind during all the period, while the cooling in the LFA (Low Frequency Array) was not as good as expected, but sufficient to operate. Therefore, only tests and observations with the LFA were possible during this first commissioning period.

2. Read-out electronics: On one hand, the total power of the DAC was constant independently of the number of KIDS detected, and therefore, when the number of KIDS detected was high the power per KID was reduced; this introduced some difficulties in the KID characterization. On the other hand, the IF band ($\sim$ 4 - 8 GHz) showed a total power slope at the high frequency end, this again

introduced a problem because the KIDs in this part of the band were at different power levels than the others and therefore difficult to characterize.

3. The optical alignment: Because of the complexity of the optical design and also of the compactness of the overall structure, the alignment process was not straightforward. Two optical alignments were done: The first one using a device based on two laser pointers, and the second one finding the location of the radio beams using an absorber; a discussion can be found in subsection 3.2.3.

During the first half of this year (2014), the team has been working on the solution of all these issues, and also on the improvement of some other aspects related to the assembling, system operation and characterization. The second commissioning of the camera is planned for the autumn of the current year.

In this chapter the first results of the camera are shown. Despite the troubles with the cooling, optical alignment and the read-out, some data could be extracted. In the following sections this data has been analyzed and some conclusions about the distortion, pixel characterization, beam shape, angular resolution and pixel spacing have been drawn. Furthermore, the last available day of the commissioning period the NGC 3603 nebula could be observed, and a map of this source was obtained. Some conclusions about the performance of the camera have also been extracted comparing the map with some available data of this source.

Some pictures document the montage process and the final installationn:

Figure 3.1 shows the process where the cryostat was lifted up from the ground floor to the second floor of the telescope, where the Cassegrain cabin is located, using the telescope crane.

Figures 3.2, 3.3 and 3.4 show the mirrors installed inside the Cassegrain cabin; Mirror 3 (M3) on the bottom of the cabin; flat mirror 1 (FM1) directly on the INVAR cone of the telescope; and Flat Mirror 2 (FM2) and Mirror 4 (M4) attached next to the cryostat.

Figure 3.5 shows some IF electronics modules mounted in the structure above the cryostat and the M4.

3.2 Performance on the sky

The optical design in the Zemax[1] software was done in the direction sky-detector, therefore, all measurements taken in the simulations are done in the image plane

[1] https://www.radiantzemax.com/en

FIGURE 3.1— Cryostat being elevated with the telescope crane. The Cassegrain cabin is at the second floor of the telescope.

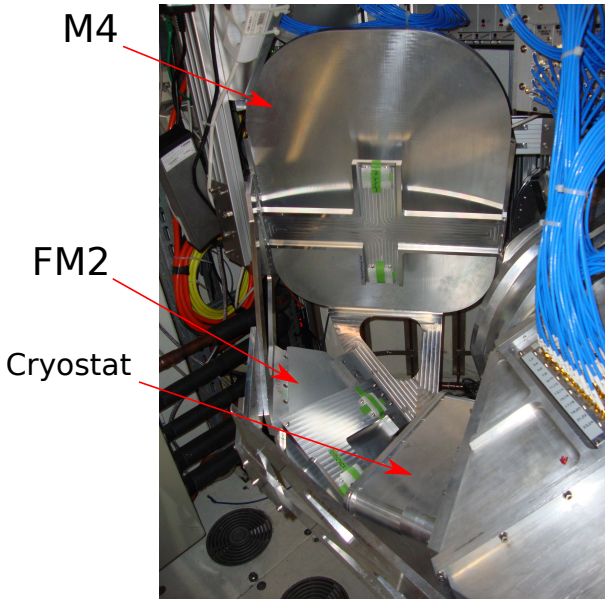

FIGURE 3.2— Mirror 4 (M4) and Flat Mirror 2 (FM2) mounted in the Cassegrain cabin.

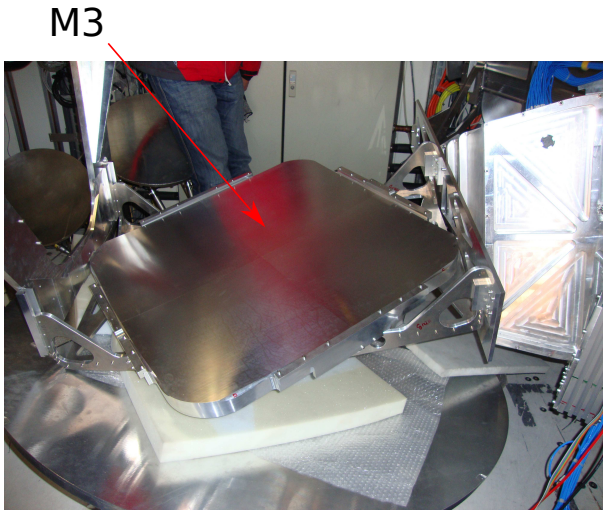

FIGURE 3.3— Mirror 3 (M3) located at the bottom of the Cassegrain cabin.

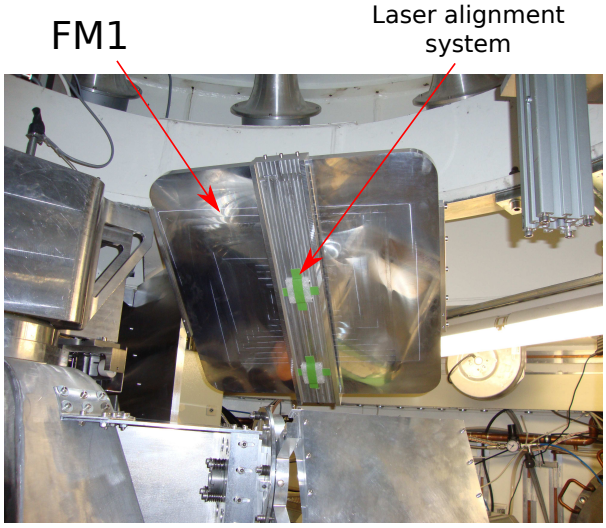

FIGURE 3.4— Flat Mirror 1 mounted directly on the INVAR cone of the telescope, inside the Cassegrain cabin. The laser alignment system composed of two optical mirrors (see section 3.2.3) can also be seen.

(detector plane), or at least from the sky to a specific surface, but always in this direction. In the real observations, since detector and telescope are a single block, it has to be considered that the measurements are taken "on the sky" with the beam produced by the detector, the optics and the telescope together. Therefore, in order to

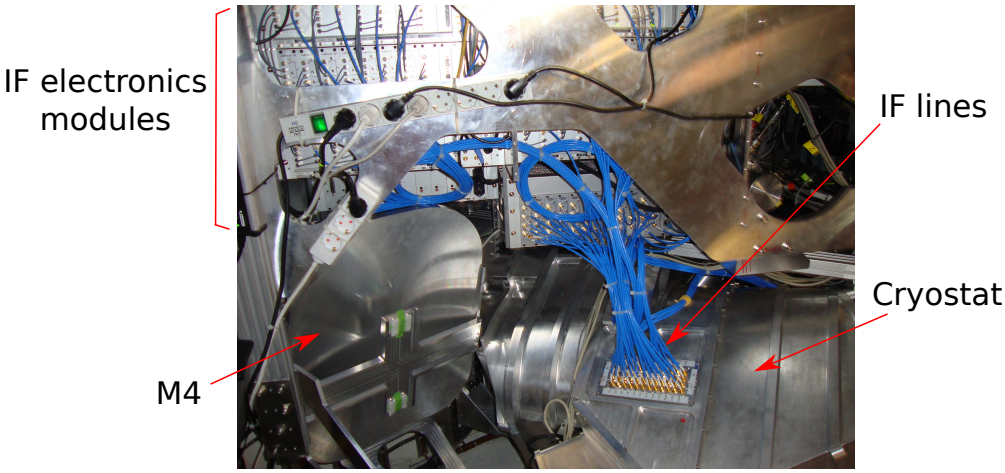

FIGURE 3.5— IF electronics modules mounted in the structure above the cryostat and M4.

compare results from the observations with the simulations some precautions have to be taken. In both cases the optical path crosses the optics in opposite directions. If the optics design is considered as a black box with its corresponding transfer function (or OTF, optical transfer function), the inverse of that function should be applied if the path is in the opposite direction, as it happens between simulations and real observations.

3.2.1 Array parameters

During the period of the commissioning the number of available channels was changing. Before each run of observations a KID search (to detect where the KID tones are; see section 2.1 in chapter 2) and a calibration had to be done, and depending on the status of the detector at that moment the number of KIDs (or channels) available could change significantly. We noticed that the number of available channels was decreasing during the commissioning period. After KID detection and calibration some fully sampled maps of planets (mainly Jupiter and Mars) were done in order to characterize the position on sky and the relative gain of each detector. These parameters were stored in several files called RCPs (average Receiver Channel Parameters). The RCP files also depend on to the source used for the mapping, especially in the two upper corners of the array where the sensitivity was significantly lower. The detectors in these parts could not be well characterized with Mars (too faint for the noise level at this position) and they were only characterized in the RCPs resulting from the Jupiter maps. Just to have an idea, at the beginning of the period around 1900 KIDs were well characterized after the KID search and with the fully sampled map of Jupiter; while in the last days, only around 1100 were usable after the same operation. Even for

fully sampled Mars maps some attempts were done using only half of the array (the half with better sensitivity, see figure 3.8). The general idea behind this is to create a master RCP combining all of them, where each KID is well characterized, and to use that in the future for normal observations.

Moreover, the RCP files give us a realistic picture of the Field of View (FoV) on sky. In figure 3.6 one of the most complete RCPs is shown; it was created from a fully sampled map on Jupiter. It is composed by 1904 detectors (or KIDs, or pixels). On one hand, the distribution of the relative detector gains is indicated by the color scale; it can be noticed how the pixels at the edges of the array suffer from a reduction in gain compared with the rest. This could be just a random effect or a consequence of an optical misalignment; this issue is explained later in this chapter. On the other hand, the resulting distortion created by the optics over the FoV can be also seen. On the figure, it can be clearly differentiated four quadrants, with a cross-shape gap between them; this is due to the geometry of the detector itself, which is composed of four sub-detectors (see section 2.1 in chapter 2).

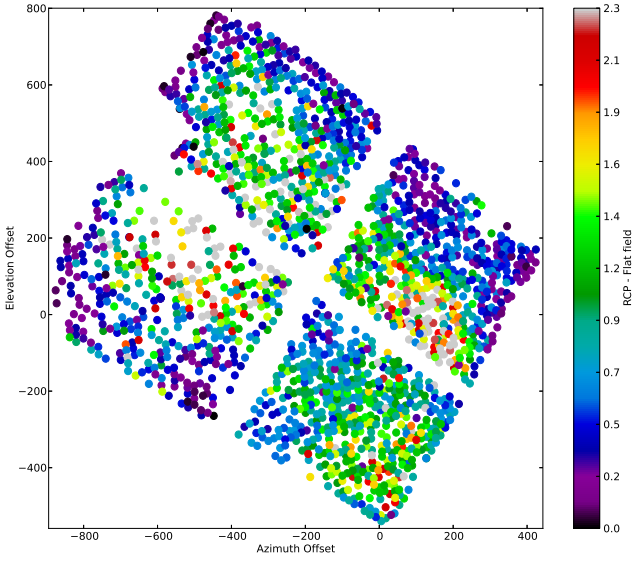

FIGURE 3.6— RCP of the detector resulting from a fully sampled map of Jupiter. It can be seen that almost the full extent of the $900''$ wide FoV is covered. Some distortion can be seen. The color scale represents the pixel gain. The cross-shape gap is due to the geometry of the detector array which is composed of four sub-detectors.

In figure 3.7 the previous RCP (green squares) with the simulated distorted FoV on sky resulting from Zemax (red diamonds) is plotted. The software computes the coordinates of a regular grid of rays which has been passed through the optical system, and gives the resulting coordinates in the image plane (detector plane) (this tool is explained in detail in section 2.5.2 of chapter 2). On one hand, the regular grid of coordinates on sky (starting point) and the resulting grid of coordinates on the detector plane are known from the software. On the other hand, the real size of the detector is also known (see section 2.1 in chapter 2). Therefore, with an over-sized grid FoV we can see which rays from the starting grid on sky are really hitting the detector (117 x 117 mm). Hence, discriminating those rays from the starting grid which are not hitting the detector, the FoV shape of our detector on sky can be computed. Also, if we measure the resulting FoV on sky with this procedure, we see that it is completely in agreement with the FoV measured during the optics simulations (see section 2.5.2 in chapter 2), $\sim 14.7'$ x $18.8'$.

Looking at the figure two aspects have to be pointed out. First, it can be seen that both FoVs are almost fully in agreement. This reveals that the distortion from the real system is very close to the simulated one, which is $\sim 13\%$ on average. And second, it can be also noticed that in the upper quadrant the simulated FoV is slightly larger than the real FoV. It seems that the FoV is truncated by the optical system, this can be either due to misalignments or due to a limitation of the system itself owing to the margins considered in the optimization.

3.2.2 Beam study

Main beam

In order to characterize the beam shape several fully sampled maps on Mars were done; here one of the best resulting maps is presented. The RCP derived from this fully sampled map is shown in figure 3.8. It is composed of 920 detectors and, as can be seen in the figure, the main contribution comes from the bottom quadrant. In the left and right quadrants just a few pixels were detected and in the top quadrant the gain of the pixels is relatively low. Thus, the contribution of these pixels is reduced since in the data reduction the contribution of each pixel is weighted according to its gain.

As we will see, the obtained results are reasonably good because, thanks to the RCP, pixels which are not well characterized ("bad pixels") are either nonexistent or weighted down due to their low gain. This means that only the "good" pixels are considered, but of course one should not forget that the efficiency of the detector is low since approximately only a third of the total array is used for the present calculation.

In figure 3.9 the beam shape derived from the fully sampled map on Mars is shown.

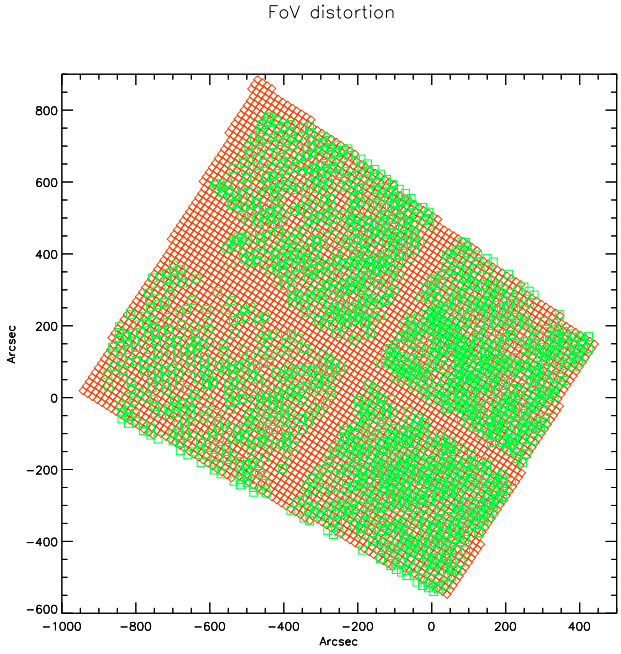

FIGURE 3.7— FoV distortion. Green squares are the RCP of the figure 3.6, and represent the real FoV distortion on sky. Red diamonds are the simulated distorted FoV on sky computed with the Zemax software.

The shape is not a perfect circle and it can be fitted with an elliptical Gaussian of $FWHM_1 = 19.4''$, $FWHM_2 = 17.1''$ and with a rotation angle of $-13.^{\circ}94$, defined as the counter-clockwise counted position angle of the major axis with respect to the X axis (the azimuth). On the left panel of the figure the Mars map is shown with a reduced flux color scale in order to see the low flux received in the side lobes. On the right panel, the same map is plotted but with the complete flux color scale to well characterize the beam. In the following I refer to this beam as "average beam".

In figure 3.10 two sectional cuts in the two aforesaid directions of the elliptical Gaussian beam are shown (blue line). On each cut the fitted Gaussian is plotted as well (red line). It can be seen how the shape of the main beam is almost perfectly fitted by the calculated Gaussian, which means that the measured FWHMs are a reliable estimation.

It is important to comment that in order to well determine the beam shape a point source is needed. In our case we used Mars, which is almost a point source at the

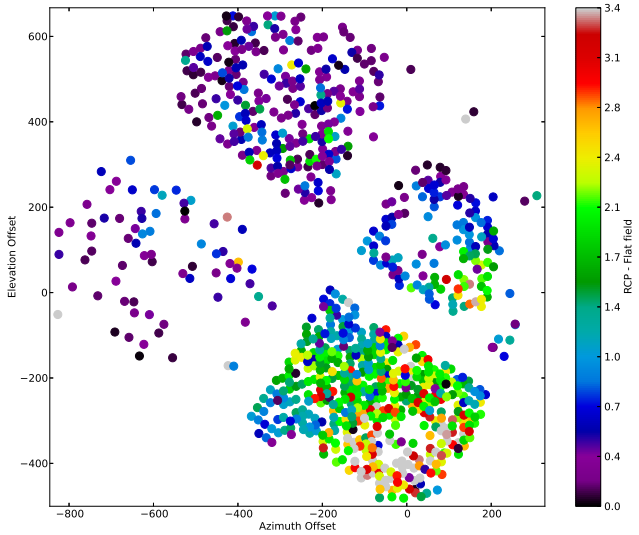

FIGURE 3.8— RCP of the detector resulting from a fully sampled map of Mars. The color scale represents the pixel gain.

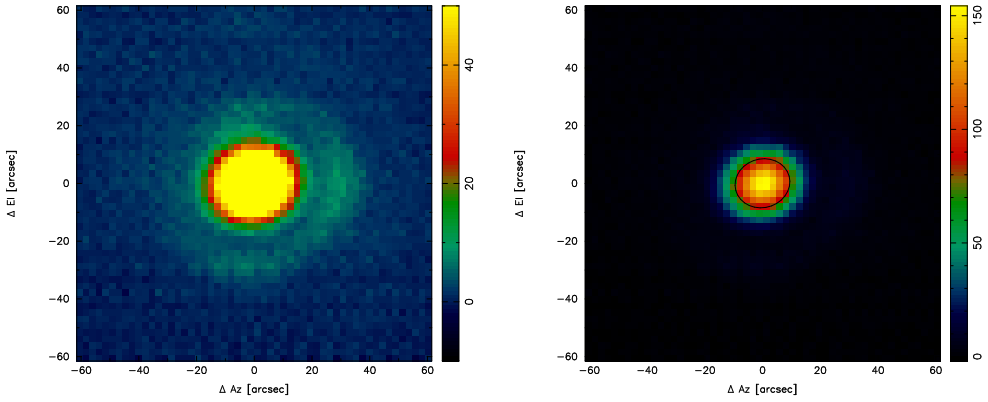

FIGURE 3.9— Beam shape derived from the fully sampled map on Mars. The beam represents an elliptical Gaussian shape with $FWHM_1 = 19.4''$, $FWHM_2 = 17.1''$ and rotation angle from the X axis (Azimuth in this plot) of $-13.^{\circ}94$ (counter-clockwise). Both pictures are for the same map but with different flux color scale. The black line in the right panel is the half-power contour.

working frequency; the convolution of this source with a beam of the expected size (around $18''$) only yields an increment of 2% in the resulting beam. Also, it is important

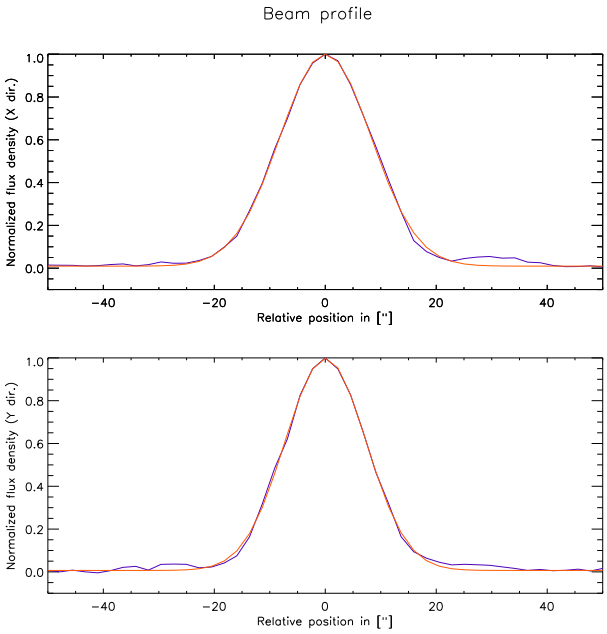

FIGURE 3.10— Beam profile along the X-cut and Y-cut (blue line). The red line is the Gaussian fit with the $FWHM_1$ and $FWHM_2$ of the picture 3.9.

to mention that at the time of the observations the source presented less than 0.5% of ellipticity on sky, which is inconsequential for the characterization of the beam. Concluding, beams derived from Mars can be considered almost the real beam shape of our instrument (detector, optics and telescope together).

During the commissioning run some maps on Uranus were also done. Unfortunately, because of the lack of sensitivity of the detector (low signal to noise ratio) during the period not so much useful data could be extracted from these maps. Figure 3.11 shows the only Uranus map obtained with some useful data. An elliptical Gaussian could be fitted in the resulting beam with $FWHM_1 = 18.5''$, $FWHM_2 = 16.9''$ and with a rotation angle with respect to the X axis of $-26.^{\circ}96$ (counter-clockwise). These results are in quite good agreement with those extracted from the Mars map.

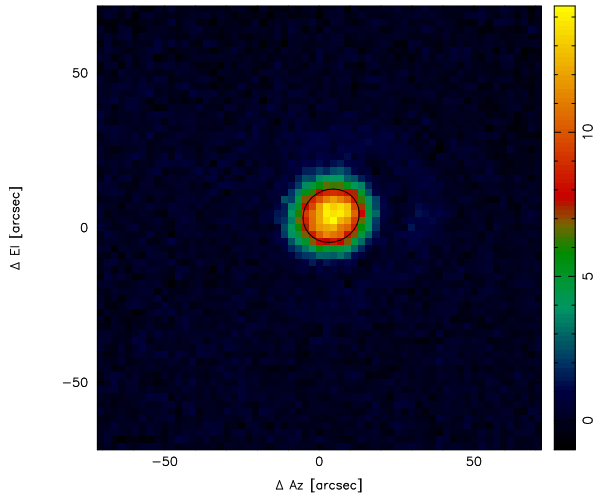

FIGURE 3.11— Beam shape derived from a fully sampled map on Uranus. An elliptical Gaussian could be fitted: $FWHM_1 = 18.5''$, $FWHM_2 = 16.9''$ and a position angle from the X axis of $-26.^{\circ}96$ (counter-clockwise).

First side lobe

The next important step is to study the effects of the side lobes of the beam. With our current observation, the relation between the integrated flux contained in the main beam and the flux enclosed by the first side lobe can be calculated. In figure 3.12 the beam map derived from the Mars map is shown again with two white circles, which roughly determine the separation between the main beam and the first side lobe (inner white circle), and the border between the first side lobe and the blank sky (outer white circle). To determine these margins figure 3.10 was also useful. Further sidelobes beyond the first one could not be measured, because a very bright source would be needed for that.

From the flux calculation we obtained that approximately the 85% of the flux is enclosed by the main beam. It is important not to confuse this calculation with the main beam efficiency, since for that the complete radiation pattern of the antenna would be needed.

Comparison of the results

In order to better characterize our array, the beams at the corners of the array were computed. A group of pixels was selected in each corner and their beam was calculated. The idea behind that was to analyze how the beam behaves in different parts of the array, and comparing these results with the simulations the level of agreement

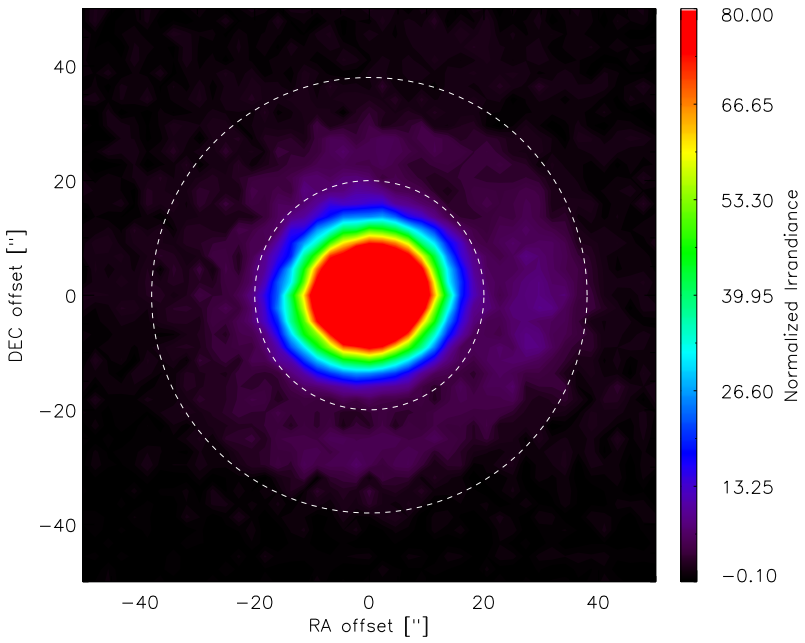

FIGURE 3.12— Beam map derived from the fully sampled maps on Mars, with reduced flux color scale in order to notice the side lobes (as in figure 3.9-right). The white inner circle indicates approximately the separation between the main beam and the first side lobe and the outer circle the border between the first side lobe and the sky. Roughly 85% of the flux is enclosed by the main beam.

with the model can be studied.

As mentioned at the beginning of subsection 3.2.1 the sensitivity was especially low in the corners, and even in the case of Mars there was no detection in a relatively large number of pixels (see figure 3.8). Despite this issue, three beam maps could be computed combining the responses of the pixels in the corners of the array. The fourth one, corresponding to the left quadrant, was impossible to compute since very few pixels were available in this part of the array, and the resulting beam map was extremely noisy. Figure 3.13 shows the beam maps resulting from the three corners where they were computed. The map on the top-right corresponds to the upper quadrant in figure 3.8 (“corner 2” hereafter), the map on the bottom-left corresponds to the lower quadrant (“corner 3” hereafter) and the map on the bottom-right corresponds to the right quadrant (“corner 4” hereafter); the empty space on the top-left would correspond to the left quadrant (“corner 1” hereafter), but as already mentioned, its calculation was not possible (this nomenclature is used in order to agree with the following figures).

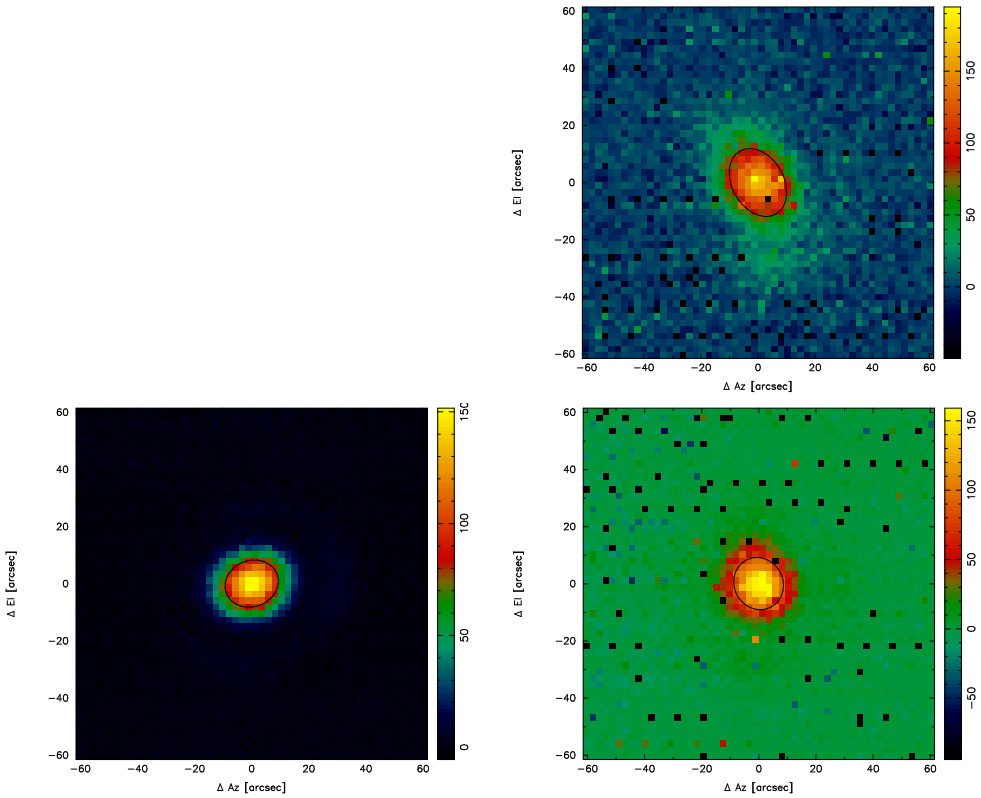

FIGURE 3.13— Mars beam maps in three corners of the array. Due to the lack of pixels available in the fourth corner (corner 1 in our nomenclature), the beam could not be computed in this area. Black circles are the Gaussian beam fittings. Each map was done adding the response of several pixels.

Despite the low signal-to-noise ratio (especially in the top-right and bottom-right maps), the beam maps could be computed and a Gaussian fit could be done in order to characterize the beam shapes. As expected, the resulting Gaussian fits were elliptical in all cases. In table 3.1 the resulting fit parameters are shown; it can be seen how the ellipticity becomes stronger in corner 2 (it can be assumed that it would be strong as well if the beam in corner 1 had been calculated), and how the beam improves significantly in corners 3 and 4; the beam here is even better than the average beam (3.9). This makes sense because according to the RCP, the pixel quality increases in the direction “corner 1-2” to “corner 3-4” (see figure 3.8), and therefore the average beam, which is calculated combining all the pixels, can be a bit more elliptical than the beams in the corners 3 and 4 where pixels seem to be better.

In principle, the predicted level of the overall FoV distortion does not explain this high ellipticity for corner 2, and as we will see in the next section, this ellipticity could

be produced by a slight aberration coming from some misalignments in the optics.

TABLE 3.1— Gaussian beam fitting parameters for the corners of the array. Beams are derived from the fully sampled map on Mars.

Position	$FWHM_1$ **(in $''$)**	$FWHM_2$ **(in $''$)**	**FWHMs ratio**	**Angle (Ho. coord.) (in $^\circ$) (west to south)**	**Rotation (in $^\circ$) (respect main beam)**
Average beam	19.39	17.14	0.88	-14.8	0.0
Corner 1	–	–	–	–	–
Corner 2	25.33	18.04	0.71	59.6	74.4
Corner 3	18.98	16.19	0.85	-20.5	-5.7
Corner 4	18.60	17.12	0.92	63.9	78.7

In order to obtain better, i.e., less noisy beam maps and therefore to improve the beam characterization (better Gaussian fits), first, more pixels are needed in order to cover the full array and, second, the signal-to-noise ratio needs to be increased (by improving the pixel sensitivity or increasing the signal hitting the detectors).

For this reason a fully sampled map of Jupiter was used to compute the beam shapes again; specifically, the map resulting from the RCP previously shown in figure 3.6 was used. Since Jupiter is a very bright source a better characterization of the full array could be done, with more pixels available and with a better signal to noise ratio.

However, the use of Jupiter for this purpose implies basically two problems: First, Jupiter is not a point source, and therefore, if the real beam shape is required a deconvolution with the size of the planet would be needed; and second, Jupiter is not a perfect circle on sky and it presents a small ellipticity which in principle should be taken into account in the resulting beam maps. At the time of the observation Jupiter had a ratio between the minor and major axis of 0.94 (which corresponds to an ellipticity of roughly 6%) with a position angle of the minor axis of $9.^\circ45$ in equatorial coordinates in direction north to east.

Figure 3.14 shows the beam in each of the four corners resulting from the fully sampled map of Jupiter. The Gaussian fit shows that the resulting beams are elliptical; and also how the ellipticity becomes stronger in the two upper corners (corners 1 and 2). The table 3.2 shows the Gaussian fitting results for the four corners.

If the two tables (tables 3.1 and 3.2) are compared, it can be seen that in general the ellipticity is lower for Jupiter than for Mars.

Figure 3.15 shows (for corners 2, 3 and 4) the real shape of Jupiter on sky at the time of the observation (blue line), the beam derived from Mars (green line), which

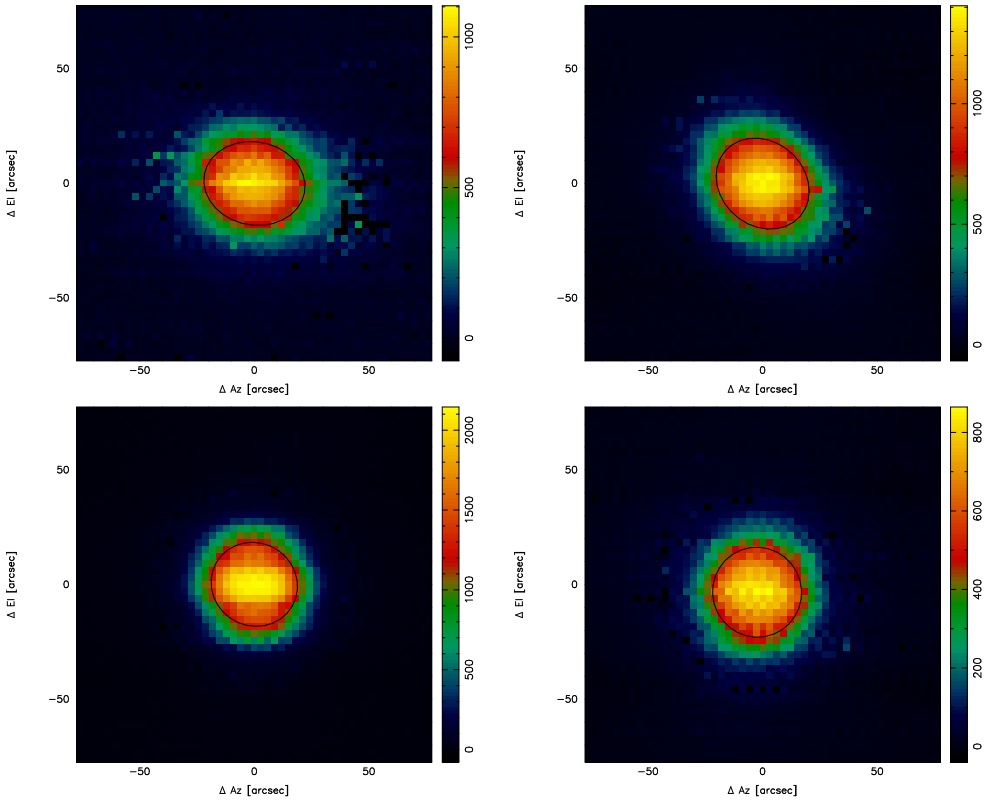

FIGURE 3.14— Jupiter beam maps on the four corners of our array. Black circles are the half-power contours of the Gaussian beam fittings. Each map was done adding the response of several pixels.

can be considered a good approximation of the real beam of the instrument, and the half-power contour of the map of Jupiter (red line), which roughly corresponds to the convolution of the two previous ones (the instrument beam convolved with the real shape of Jupiter). In order to compare the beams, all the beam calculations were done using the same coordinate system and the same point of reference for the rotation angles. The almost round shape of the disk of Jupiter and the fact that its position angle differs significantly, in all the cases, from that of the the real beam makes the resulting beam shapes from Jupiter more roundish. In the corner 2, where the hypothetical aberration is higher, the resulting Jupiter beam is dominated by the ellipticity of the real beam, and it maintains the elliptical shape. However, in the corner 3 and 4, where this hypothetical aberration is very low, due to the compensation between the two ellipses the beam becomes almost circular. This study of the resulting beam shapes supports that the beam shapes obtained from the Mars map are a reliable approximation of the real beam of our instrument.

TABLE 3.2— Gaussian beam fitting parameters for the corners of our array. Beams are derived from the fully sampled map on Jupiter.

Position	$FWHM_1$ **(in $''$)**	$FWHM_2$ **(in $''$)**	**FWHMs ratio**	**Angle (Ho. coord.) (in $^\circ$) (west to south)**	**Rotation (in $^\circ$) (respect main beam)**
Average beam	39.58	37.69	0.95	35.6	0.0
Corner 1	44.39	36.32	0.82	10.2	-25.4
Corner 2	43.35	36.67	0.85	41.1	5.5
Corner 3	38.18	36.17	0.95	29.8	5.8
Corner 4	39.34	38.75	0.98	68.5	32.9

Comparison with simulations

In order to compare these results with the simulations two Zemax software tools could be used:

1. The first one is the "Physical Optics Propagation" (POP hereafter) tool. With this tool the user defines an initial beam and the software computes the final beam after passing through the optical system. At each surface of the optical system the software computes its transfer function, which means that diffraction effects are taken into account (at each surface).

2. The second is the "Point Spread Function" (PSF hereafter) using direct integration of the Huygens method. The PSF of an optical system is the irradiance distribution that results from a single point source in the image plane. In this case geometric optics is used to propagate the beam through the optical system and computes the diffraction in a single step in the "exit pupil", which is the last surface before the image plane. Direct integration of the Huygens method means that each point of the wavefront (each ray in the geometric optics) is considered a perfect point source with amplitude and phase and radiates as a spherical wave. This method yields more accurate results than methods where diffraction is computed directly from each ray.

After some tests the option of using the POP tool was rejected. It would give us the best approximation of the reality if it was used in the direction "detector-sky" as it happens in the real observations. However, since in our case the simulations run the other way around, no useful data can be extracted from that. Our system has at least two surfaces (Lyot stop and sub-reflector) where the beam is truncated and therefore diffraction effects on these surfaces are important; since the beams are different if the system is passed through in one direction or another, the diffraction pattern may change significantly in each case.

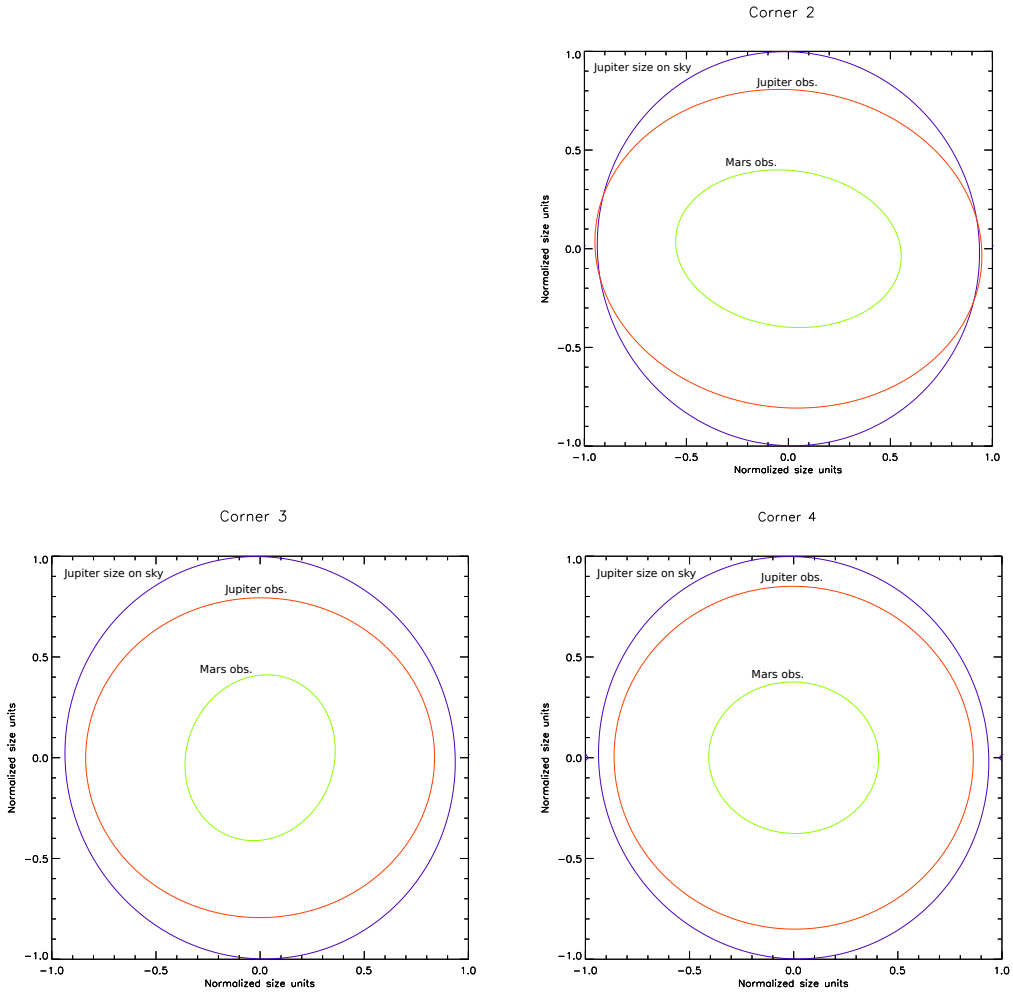

FIGURE 3.15— Ellipticity in corners 2, 3 and 4. Real shape of Jupiter on sky (blue line), half-power contour from Mars observations (green line) and half-power contour from Jupiter observations (red line). All the half-power contours calculations were done using the same system of coordinates and the same point of reference for the rotation angles. Units are normalized to the major axis of Jupiter on the sky (vertical axis).

The Huygens PSF was the tool selected for comparison; it is important to mention that comparisons between real observations and the results using this tool are very rough and that they can only give us an idea in general terms, but no specific results can be achieved with it. This means that big issues with the optical system should appear in both cases (PSF simulations and real observations), but unfortunately further

conclusions can not be drawn with this method, mainly for two reasons:

1. The PSF computation uses geometric optics (ray tracing) until the last surface, where the method computes the resulting diffraction and shows the diffraction pattern in the image plane; no diffraction is calculated in the intermediate surfaces, which in our case would be interesting because, as it was said, there are some surfaces where diffraction effects may be important. Nevertheless, the fact that in geometric optics the direction in which the system is passed through does not really matter could give us an idea of the aberration of the beams. This is because in geometric optics going in the other direction just inverts the transfer function, which allowed an easy comparison.

2. The fact to compute the diffraction only at the last surface introduces another problem; as it was said, beams are different depending in which direction the system is passed through, therefore the diffraction computed on the last surface (in direction sky-detector) is not very representative of the real situation.

Figure 3.16 shows the normalized PSFs resulting from the rays located at the four corners of the FoV. A Gaussian fit was applied to each one in order to determine the FWHMs and the ellipticity of the resulting beams. In order to show the quality of the Gaussian fits, in figure 3.17 they are over-plotted to the beam profiles in the two axes of the ellipses (at least in two cases the PSF is almost circular and the ellipticity is negligible).

The same exercise was done for the PSF derived from the central ray simulation. In figure 3.18 the resulting PSF is plotted (top-left) and also the resulting Gaussian fits over the beam profiles are shown (bottom-left). On the right side of the figure the average beam resulting from the Mars map is plotted again (top-right; same as figure 3.9), and the Gaussian fits over the beam profile are shown as well (bottom-right; same as figure 3.10). Both figures are shown together because, despite all the comparison issues explained before, this is the closest comparison between observations and simulations. It is important to mention that the beam determined from the observations is the average beam of all available pixels (see figure 3.8), while the simulated PSF is computed using only the central ray, which would correspond to the central pixel.

Table 3.3 shows the resulting parameters of the Gaussian fits to the PSFs (corners and center). It can be seen that the beams at the center, corner 1 and corner 2 are almost circular, and how the beams degrade a bit in the corner 3 and 4. These results prove the quality of the system and show that it should work properly if it does not accumulate any aberration (e.g. coming from some misalignments).

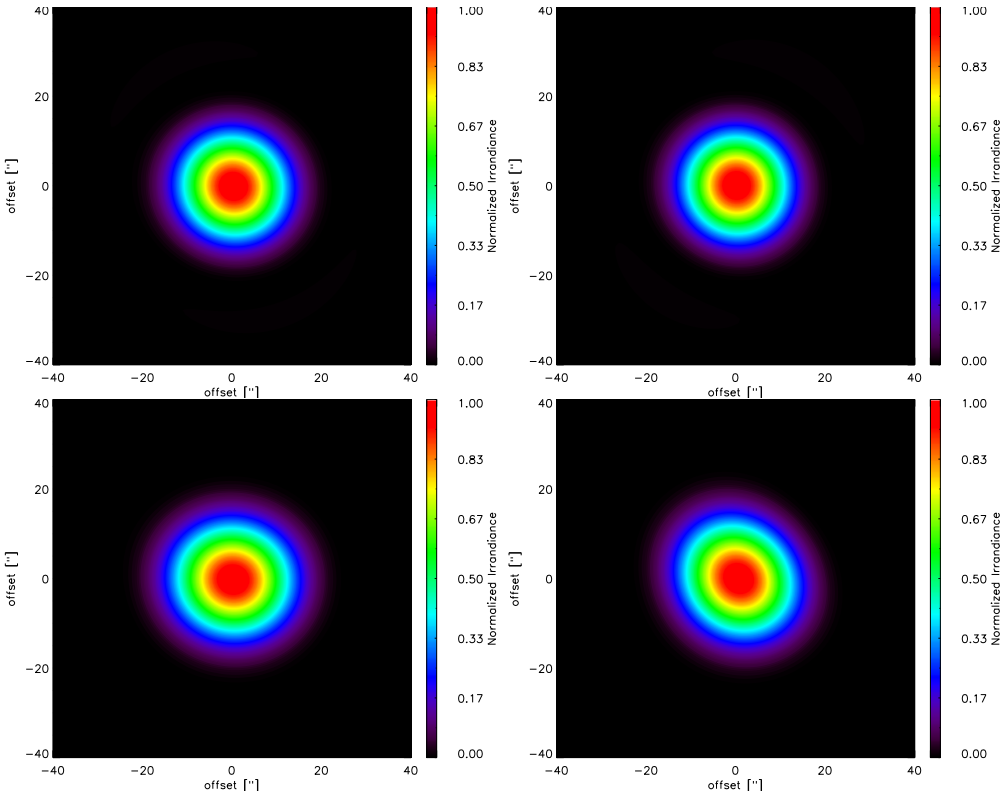

FIGURE 3.16— PSF at the four corners of the array using direct integration of Huygens method. PSF is computed at the detector plane.

Table 3.4 shows the ratios between the FWHMs of the major and minor axis of our elliptical Gaussian fits in order to see the degree of ellipticity of each beam. This is done for the real beams derived from the Mars map (at the corners and for the average beam), and for the beams resulting from the PSF simulations (at the corners and in the center). The rotation angle of the resulting ellipses is shown, too; the rotation angle is measured with respect to the major axis of the resulting ellipse of the average beam (or central pixel in the case of the simulated PSF).

On one hand, it can be seen that the ellipticity in real observations is stonger than in simulated beams, which means that, despite the comparison issues explained before, the system can be improved and better beam shapes can be obtained. On the other hand, looking at the rotation angles no conclusions can be extracted. The idea behind was to analyze whether simulations and real observations had the same sense of rotation. Nevertheless, the analysis was a bit optimistic: first, because of the comparison issues, and second, if the system accumulates some aberration (e.g.

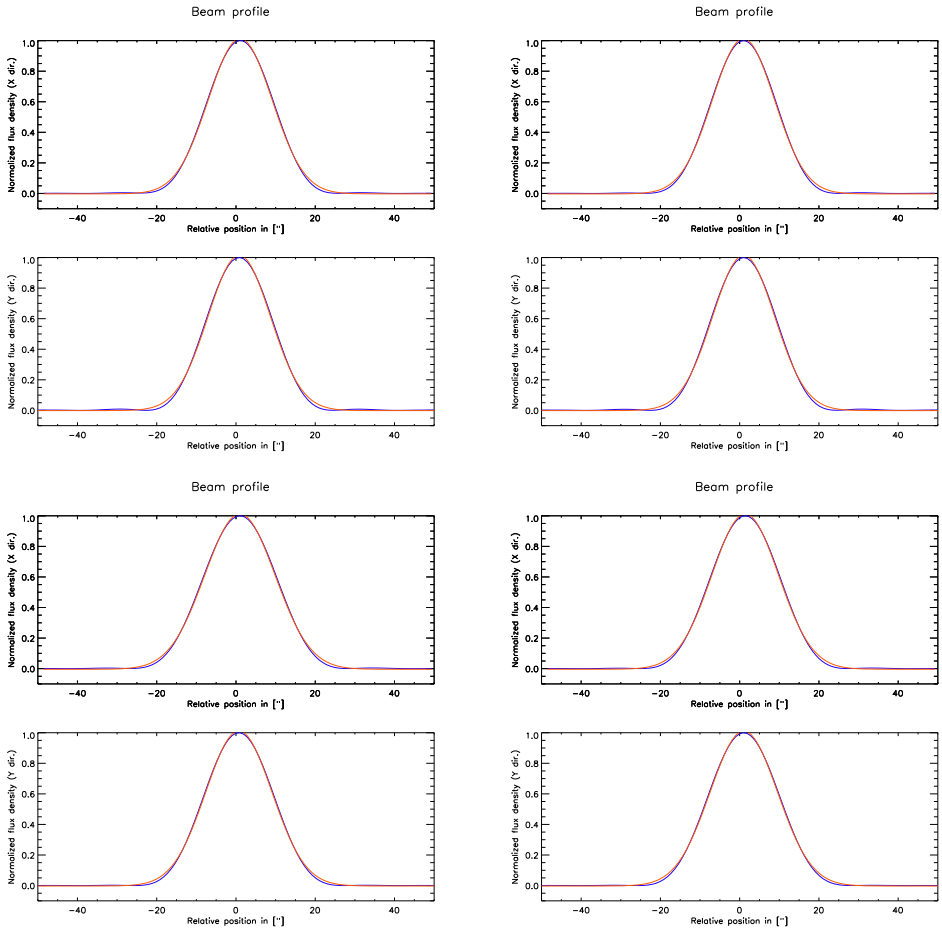

FIGURE 3.17— Fitting results of the four PSFs calculated in figure 3.16. In each figure the fits along the major and minor axis are shown. The blue line corresponds to the real profile of the PSF and the red line to the Gaussian fit.

because of some misalignments) it can differently affect the different parts of the FoV.

3.2.3 Alignment review

During the commissioning period two alignments were done within three days. The first one used a device based on two laser pointers and the second one located the radio beams with an absorber.

In figure 3.19 the two FoVs resulting from the two different alignments are shown. They correspond to two RCPs derived from two Jupiter maps. The RCP represented

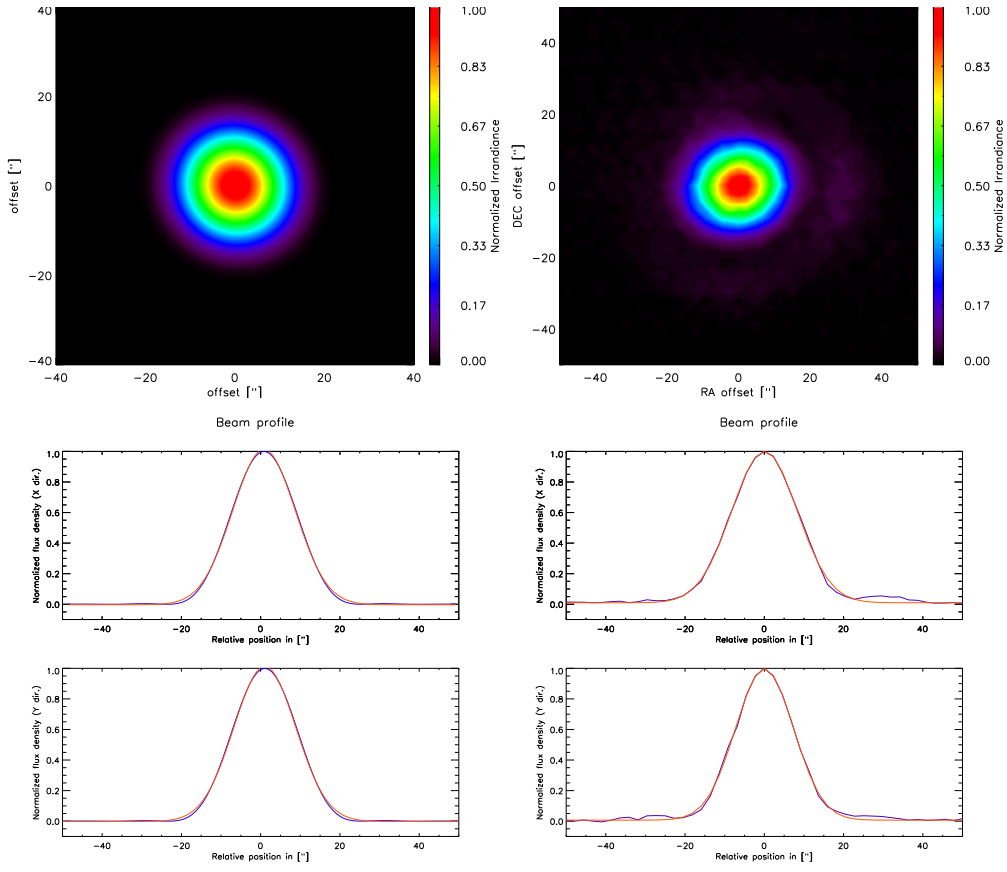

FIGURE 3.18— Normalized beam. Top-left: PSF of the central ray. Bottom-left: the beam profiles (blue) along the two axes of the elliptical Gaussian fit (red). Top-right: real average beam in the focal plane of the telescope (from Mars map). Bottom-right: the beam profiles (blue) along the two axes of the elliptical Gaussian fit (red).

by gray diamonds is the same RCP as that shown in figure 3.6 and corresponds to the first alignment (laser pointers); the other one, represented by yellow diamonds, corresponds to the second alignment (radio beams). Looking at the figure, it can be seen that there is not a big difference in terms of FoV distortion between the two alignments. On the bottom part of the figure some zooms on the FoV are done in order to see the differences of the pixel positions between the two alignments. It can be seen that these differences are rather small and only become a bit larger in the left and upper quadrant. Nevertheless, with the number of pixels available where these differences are larger, it is difficult to conclude which alignment presents less FoV distortion.

TABLE 3.3— Gaussian fitting parameters for the simulated PSFs.

Position	$FWHM_1$ **(in $''$)**	$FWHM_2$ **(in $''$)**	**FWHMs ratio**	**Angle (Ho. coord.) (in $^\circ$) (west to south)**	**Rotation (in $^\circ$) (respect main beam)**
Central beam	18.25	18.02	0.99	4.6	0.0
Corner 1	18.56	18.14	0.98	3.9	-0.7
Corner 2	18.07	18.06	1.0	2.7	-1.9
Corner 3	20.47	19.27	0.94	2.6	-2.0
Corner 4	20.55	18.76	0.91	14.5	9.9

TABLE 3.4— Ratios between the FWHMs of the major and minor axis of each elliptical Gaussian fit (for the average beam and the resulting beam at the corners; for the PSFs the central beam is shown). Rotation angles with respect to the major axis of the average beam are also shown. Both cases are shown, real beams from Mars and simulated PSFs.

Position	**Beams from Mars**		**Simulated PSFs**	
	FWHMs ratio	**Rotation (respect main beam) (in $^\circ$)**	**FWHMs ratio**	**Rotation (respect main beam) (in $^\circ$)**
Average/central beam	0.89	0.0	0.99	0.0
Corner 1	–	-	0.98	-0.7
Corner 2	0.71	74.4	1.0	-1.9
Corner 3	0.85	-5.7	0.94	-2.0
Corner 4	0.92	78.7	0.91	9.9

Another exercise that could be done in order to figure out which alignment is better was to look at the signal to noise (SNR) maps. Some signal to noise maps, obtained from different parts of the array and from each alignment, were compared. Unfortunately, this study did not provide us with any valuable conclusion. Because of several problems (mentioned in the introduction of the chapter; see section 3.1), occurring during the commissioning period, the pixels could not be well characterized, and therefore the SNR maps were varying significantly between different scans, even for the same alignment. Figure 3.20 shows the SNR peaks in different parts of the array for three different RCPs derived from Jupiter (left panel) and three more derived from Mars (right panel). In the Jupiter plot the RCP number 1 is from the first alignment and the numbers 2 and 3 are from the second one. It can be seen that no correlation exists between the SNR peaks and the corresponding alignment; the differences between the three cases are comparable. In the case of Mars only RCPs corresponding to the second alignment are shown; nevertheless, it can be seen how the differences between the SNR peaks are significantly higher than in the case of Jupiter.

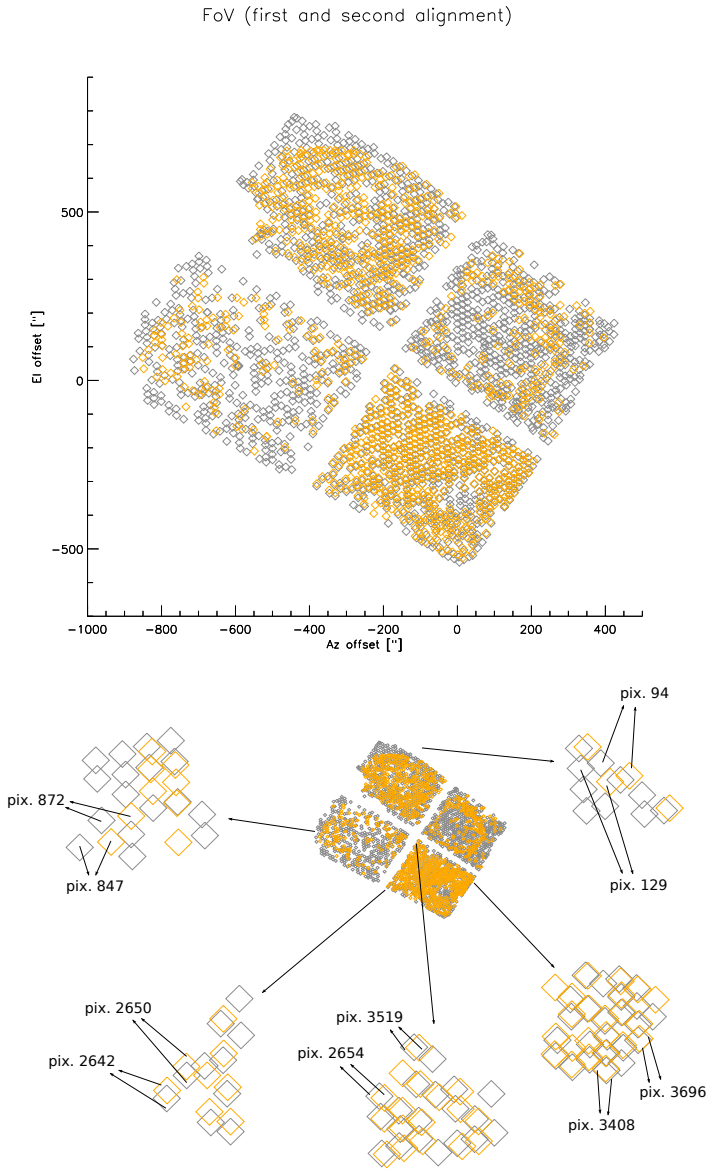

FIGURE 3.19— Two real FoVs. Gray diamonds correspond to the first alignment done during the commissioning period and yellow diamonds to the second one.

However, looking at the figures, it can be seen that the relation between the peaks of the different parts of the array tends to be constant for the different RCPs, or at least, that a degree of correlation exists between them (it happens in three of the four cases

of Jupiter and in two of the three cases of Mars).

From the previous paragraphs two conclusions can be drawn:

1. Depending on the status of the detector, the detector quality was varying during the commissioning period (look at the different RCPs). This seems to be related to the KID calibration process, which indeed was changing throughout the period. If in this process the resonance peak of each detector is not well found the SNR can be deteriorated.

2. The response of the array is different depending on where the measurement is done; however, this difference remains roughly constant for the whole commissioning period (in figure 3.20 the curve shapes of each position are comparable). This has to be related to some issues which did not change during the commissioning period; some hypothesis for that could be:

   – The optical alignment, which provided always the same illumination pattern. If the hypothesis of misalignment is confirmed, it could explain the difference in quality of the different parts of the array.

   – The power level issues explained in the introduction of the chapter (see section 3.1).

3.2.4 Detection of the alignment problem

Looking at the beam shapes in figures 3.9 and 3.13, and comparing these images with the PSF simulations in figures 3.16 and 3.18, it is clear that our system suffers from some degree of aberration. In this section we want to demonstrate that this aberration can be due to some misalignments, and therefore, if these misalignments are corrected a better response from the optical system can be obtained.

Since one of the most critical steps in the alignment process was to align the block composed by the M4 (mirror 4) and FM2 (flat mirror 2) (see figure 3.2 and also section 2.5.3 in chapter 2), some tests with this block were done with the simulation software. Some tilts and displacements were applied to this block in all possible directions. Among the tests done, two representative examples were selected in order to show how with some tilts and displacements the beams become more elliptical, and how this ellipticity follows different directions in different parts of the array (as it happens in the real beams).

The tilts and displacements applied in the two selected examples were (in (x,y,z) coordinates):

1. Misalignment 1: displacements: (+10mm, -10mm, +10mm), tilts: (0.°5, 0.°5, 0.°5).

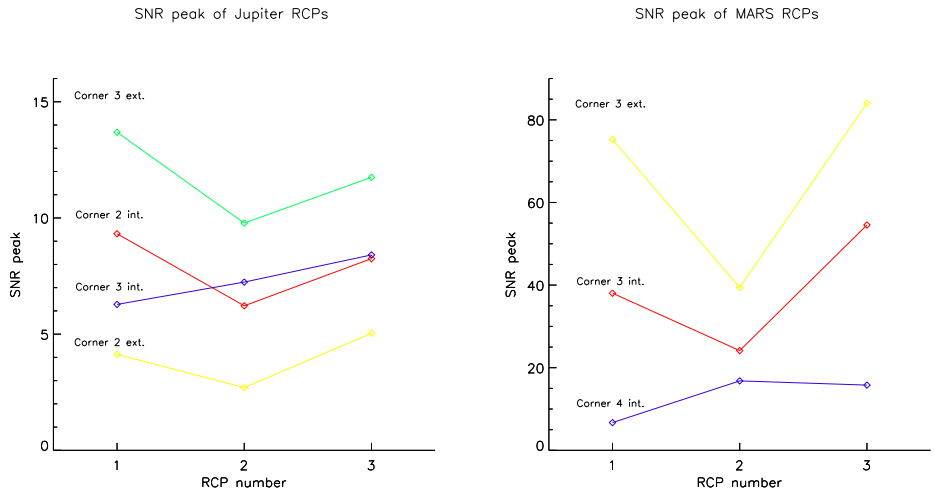

FIGURE 3.20— Signal to Noise peaks in different parts of the array for six different RCPs. Left panel: Jupiter RCPs (three RCPs); the SNR peaks were computed using a few pixels on corner 2 and 3; in each case the calculation was done in the very corner ("ext." on the figure) and in the center of the quadrant ("int." on the figure). Right panel: Mars RCPs (three RCPs); the SNR peaks were computed using a few pixels in corner 3: at the very corner ("ext.") and in the center of the quadrant ("int."); it was also computed in the center of quadrant 4 ("corner 4 int."). All the data was properly calibrated.

2. Misalignment 2: displacements: (0mm, 0mm, 0mm), tilts: (1°, 1°, 1°).

In figures 3.21 and 3.22 (left) the simulated PSFs in the corners and in the center of the FoV, respectively, are shown for the "misalignment 1". Table 3.5 shows the Gaussian fitting parameters corresponding to the simulated PSFs for that misalignment.

The same exercise was done for "misalignment 2"; figures 3.23 and 3.22 (right) show the corresponding simulated PSFs in the corners and in the center of the FoV, respectively; and table 3.5 shows the Gaussian fitting parameters corresponding to those PSFs.

Although the software tool used was the PSF, and although, as it was explained, some care has to be taken when this tool is used for comparison with the real observations, it can be seen in the figures (and to more detail in the tables) how the beam degrades with the tilts and displacements applied to the M4-FM2 block. This

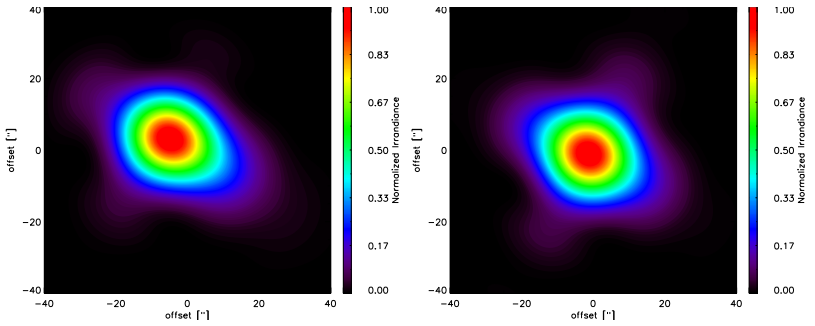

(a)

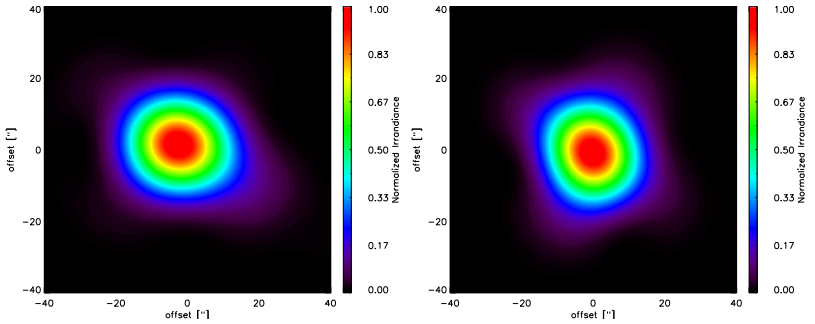

(b)

FIGURE 3.21— Misalignment 1: displacements: (+10, -10, +10), tilts: (0.°5, 0.°5, 0.°5). PSF at the four corners of the array using direct integration with the Huygens method. The PSF is computed at the detector plane.

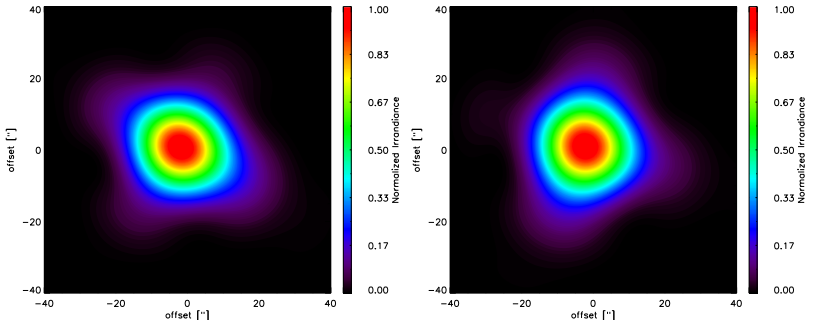

FIGURE 3.22— PSF of the central pixel of misalignment 1 (left) and misalignment 2 (right). The PSF is computed at the detector plane.

seems to indicate that at the telescope our system suffers from some misalignment problems.

TABLE 3.5— Gaussian fitting parameters for the PSFs of misalignment 1.

Position	$FWHM_1$ **(in $''$)**	$FWHM_2$ **(in $''$)**	**FWHMs ratio**	**Angle (Ho. coord.) (in $^\circ$) (west to south)**	**Rotation (in $^\circ$) (respect main beam)**
Central beam	24.13	19.82	0.82	14.38	0.0
Corner 1	25.66	18.83	0.73	15.0	0.62
Corner 2	24.65	19.61	0.80	14.81	0.43
Corner 3	24.79	20.75	0.84	8.7	-5.68
Corner 4	22.31	21.95	0.98	15.66	1.28

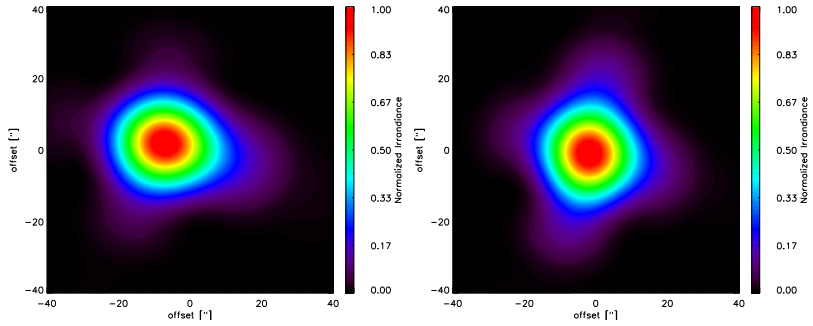

(a)

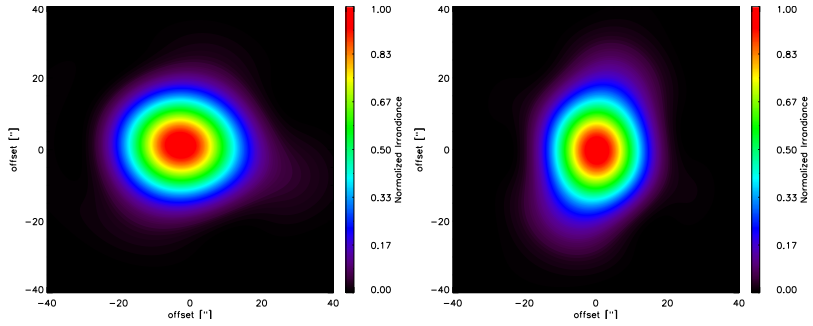

(b)

FIGURE 3.23— Misalignment 2: displacements: (0, 0, 0), tilts: (1°, 1°, 1°). PSF in the four corners of the array using direct integration with the Huygens method. The PSF is computed in the detector plane.

In table 3.7 the ratios between the two FWHMs (major and minor axis) of the resulting elliptical PSFs are shown for the two misalignment cases; the ratios for the real beams are also shown (same as table 3.4) to make the comparison easier. Again, despite the comparison issues already explained, it seems that applying some misalignment in our simulations a response similar to the real one could be achieved.

TABLE 3.6— Gaussian fitting parameters for the PSFs of misalignment 2.

Position	$FWHM_1$ **(in $''$)**	$FWHM_2$ **(in $''$)**	**FWHMs ratio**	**Angle (Ho. coord.) (in $^\circ$) (west to south)**	**Rotation (in $^\circ$) (respect main beam)**
Central beam	22.83	21.57	0.94	90.0	0.0
Corner 1	24.54	20.29	0.83	4.9	-85.1
Corner 2	23.23	21.71	0.93	92.3	2.3
Corner 3	25.03	21.60	0.86	1.0	-89.0
Corner 4	23.09	21.21	0.92	130.7	40.7

The table also shows the rotation angles with respect to the average beam (or central ray in the case of the PSFs); however, no further conclusions can be drawn from that since apparently no correlation between the angles exists for the three cases (real beams, beams from misalignment 1 and beams from misalignment 2).

TABLE 3.7— Ratios between the FWHMs of the major and minor axis for each elliptical Gaussian fit. Rotation angles with respect to the average beam of each case are also shown. Three cases are shown: real beams from Mars and simulated PSFs under misalignments 1 and 2.

Position	**Beams from Mars**		**PSFs misal. 1**		**PSFs misal. 2**	
	FWHMs ratio	**Rotation (in $^\circ$)**	**FWHMs ratio**	**Rotation (in $^\circ$)**	**FWHMs ratio**	**Rotation (in $^\circ$)**
Average/central beam	0.89	0.0	0.82	0.0	0.94	0.0
Corner 1	–	-	0.73	0.62	0.83	-85.1
Corner 2	0.71	74.4	0.80	0.43	0.93	2.3
Corner 3	0.85	-5.7	0.84	-5.68	0.86	-89.0
Corner 4	0.92	78.7	0.95	1.28	0.92	40.7

Finally, in figure 3.24 the simulated FoV distortion on sky (blue triangles) is shown for the two misalignment cases. The upper panel represents the FoV for "misalignment 1" and the lower one the FoV for "misalignment 2". In each plot the real FoV (green squares) and the simulated, original one (i.e., without misalignments, red diamonds, same as figure 3.7) are shown. From these plots it can be concluded that, despite the degradation of the beam, the general distortion of the FoV does not change substantially with respect to the original case. This would agree with our hypothesis: The real system suffers from some misalignments because the beams are degraded (elliptical shape), even if the real and the simulated FoV distortions are similar (i.e., the original FoV and the Fovs resulting from the two misalignments).

It is important to mention that neither of the two misalignment simulations corresponds to the real case. The goal of this study was to affirm that our system suffers from some misalignments, showing the behavior of the system under two representative examples, and we conclude that applying some tilts and decenters to the optical elements a response similar to the real one can be found.

3.2.5 Angular resolution

Once the beam is characterized, the angular resolution of the detector can be determined. Also, looking at the resulting beams using a few pixels in each corner, we can study how this angular resolution changes across the array.

By definition, the angular resolution of a system is the minimum distance between two distinguishable objects in the image plane. This distance can be approximated by the following formula:

$$R = \alpha \, \frac{\lambda}{D} \tag{3.1}$$

where λ is the wavelength, D the diameter of the telescope and R the resulting angular resolution in radians. The factor α can vary according to the applied criterion, which depends on the characteristics of the system, e.g., in our case also on the illumination of the sub-reflector.

According to the Rayleigh criterion α becomes 1.220, which is derived from the position of the first dark circular ring surrounding the central Airy disc of the diffraction pattern. This is the most common estimation for the angular resolution in diffraction-limited optical systems. With this criterion the dip in the response to two point sources of equal intensity separated by the minimum distance is at $\sim 4/3$ of the peak intensity.

The full width at half maximum (FWHM) is normally used to define the beam width and can be used as an approximation for the angular resolution as well; which means that we consider two sources as resolved if the half-power contours of their diffraction pattern do not intersect. With a uniform grading function it corresponds to $\alpha = 1.02$ ($R = 1.02\,\lambda/D$, Baars 2003).

In general terms, the previous formula of the Rayleigh criterion can not be directly applied to determine the theoretical angular resolution of our instrument. The size of the main beam is affected by the aperture efficiency (η_a) of the telescope, which relates the geometrical aperture area of the main dish of the telescope to the effective aperture area. The aperture efficiency is determined by a number of phenomena, which can be described by individual efficiency coefficients, such as, illumination efficiency, spillover efficiency, blocking efficiency due to the sub-reflector, etc (Baars 2003). Since some of these parameters are difficult to compute from first principles, Güsten

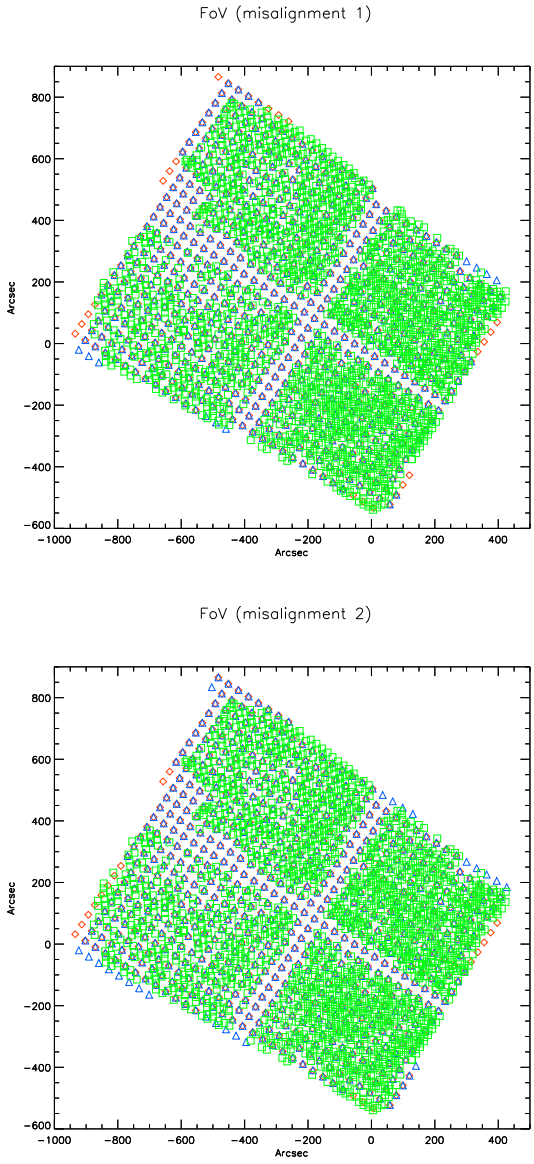

FIGURE 3.24— Distorted FoV for the misalignment cases. Green squares are the real FoV of the RCP derived from the Mars map. Red diamonds are the simulated FoV without distortion. Blue triangles are the simulated FoV under misalignment 1 (top panel) and misalignment 2 (bottom panel).

et al. (2006) compute the aperture efficiency and the beam width using astronomical measurements. Results are shown in table 2 of their study; for a frequency of 352 GHz

the aperture efficiency is 0.60 and the beam width is $\simeq 17.3''$. Now, after this exercise, it can be seen that the real angular resolution of the telescope, at this frequency, is consistent with the Rayleigh criterion ($1.2\lambda/D \approx 17.5''$) (Güsten et al. 2006).

The problem which appears now is that our resulting beam is not circular, and thus, different angular resolutions are found along different directions on the sky. This means that depending on the scanning pattern of the telescope on the sky, the angular resolution could be slightly different.

Table 3.8 shows the two angular resolutions in the two directions of the elliptical main beam (corresponding to the two FWHMs, see table 3.1). A third angular resolution is calculated corresponding to the average between the two previous FWHMs; since the ellipticity is rather weak this gives us a general idea of the angular resolution of our instrument. The factor α was also calculated to compare the results with the theoretical Rayleigh criterion: it can be seen on the table that it fully agrees with the Rayleigh criterion, which verifies that our system is diffraction limited.

Furthermore, if this result is compared with the angular resolution of LABOCA, which operates at the same frequency and in the same telescope, it can be seen that it is also consistent; the angular resolution of LABOCA is $\simeq 18.6''$ (from the APEX-LABOCA web site[2]).

TABLE 3.8— Angular resolution of the main beam. It is calculated for the major and minor axis of the elliptical beam, and also averaging them.

	Value (in $''$)	**Factor α**
Ang. resolution (major axis)	19.4	1.30
Ang. resolution (minor axis)	17.1	1.14
Ang. resolution avrg	18.3	1.22

The same exercise was done for the beams in the corners; the results are given in table 3.9. In each corner the average between the two FWHMs (major and minor axis of the ellipse) was also calculated. For the corners 3 and 4, where the ellipticity is low, this can provide a realistic angular resolution, as for the central beam; but for the corner 2, where the ellipticity becomes stronger, some care should be taken with the result because approximating this shape by a circle becomes meaningless.

Since the beam on corner 1 derived from Mars was not possible to compute, no information about the angular resolution in that part of the array is available. Nevertheless, looking at the data obtained from the Jupiter map in this corner, it could

[2] `http://www.apex-telescope.org/bolometer/laboca/technical/`

TABLE 3.9— Angular resolution in the corners of the array. For each corner the major and the minor axis of the beam are calculated; their average is also given.

	Value (in $''$)	**Factor α**
Corner 2 ang. res. (major axis)	25.3	1.69
Corner 2 ang. res. (minor axis)	18.0	1.20
Corner 2 ang. res. avrg	**21.7**	**1.45**
Corner 3 ang. res. (major axis)	19.0	1.27
Corner 3 ang. res. (minor axis)	16.2	1.08
Corner 3 ang. res. avrg	**17.6**	**1.18**
Corner 4 ang. res. (major axis)	18.6	1.24
Corner 4 ang. res. (minor axis)	17.1	1.14
Corner 4 ang. res. avrg	**17.9**	**1.20**

be assumed that the results in terms of ellipticity would be similar to those from corner 2.

Regarding the factor α, it can be seen how in corners 3 and 4, where the ellipticity is smooth, the angular resolution is also consistent with the Rayleigh criterion.

3.2.6 Pixel spacing

The next and last step of this section is to calculate the pixel spacing of our array. According to the specifications it should be 1 $F\lambda$, which corresponds to a pixel spacing of ≈ 7 mm in the focal plane of the telescope (the APEX F-number is 8 and the working wavelength 870 μm). This pixel spacing is a good agreement between throughput, mapping speed and the resources given. If the plate scale of the telescope is used ($2.15\,''/\text{mm}$) the pixel spacing in angular units can be obtained: $7\text{ mm} \cdot 2.15''/\text{mm} \approx 15''$.

In order to calculate the real pixel spacing, all the pixel distances of the two RCPs shown at the beginning of this section were computed. The RCPs correspond to those shown in figures 3.6 and 3.8, which were derived from maps of Jupiter and Mars, respectively. With the results obtained two histograms were computed, one for each case (see figure 3.25 upper panels). The first peak in each histogram would correspond to the closest distance between pixels and therefore the pixel spacing. This is approximately 1.1 $F\lambda$ for the Jupiter RCP and 1.0 $F\lambda$ for the Mars RCP. Indeed, these results agree with the theoretical pixel spacing (1.0 $F\lambda$) and also with the pixel spacing obtained during the design development ($\sim 1.06\ F\lambda$).

In order to compare the previous result with a predicted pixel distribution a grid simulating 1600 pixels in a hexagonal arrangement was created. Figure 3.26 shows on the upper panel the whole grid, and on the lower panel a zoom on some pixels in order

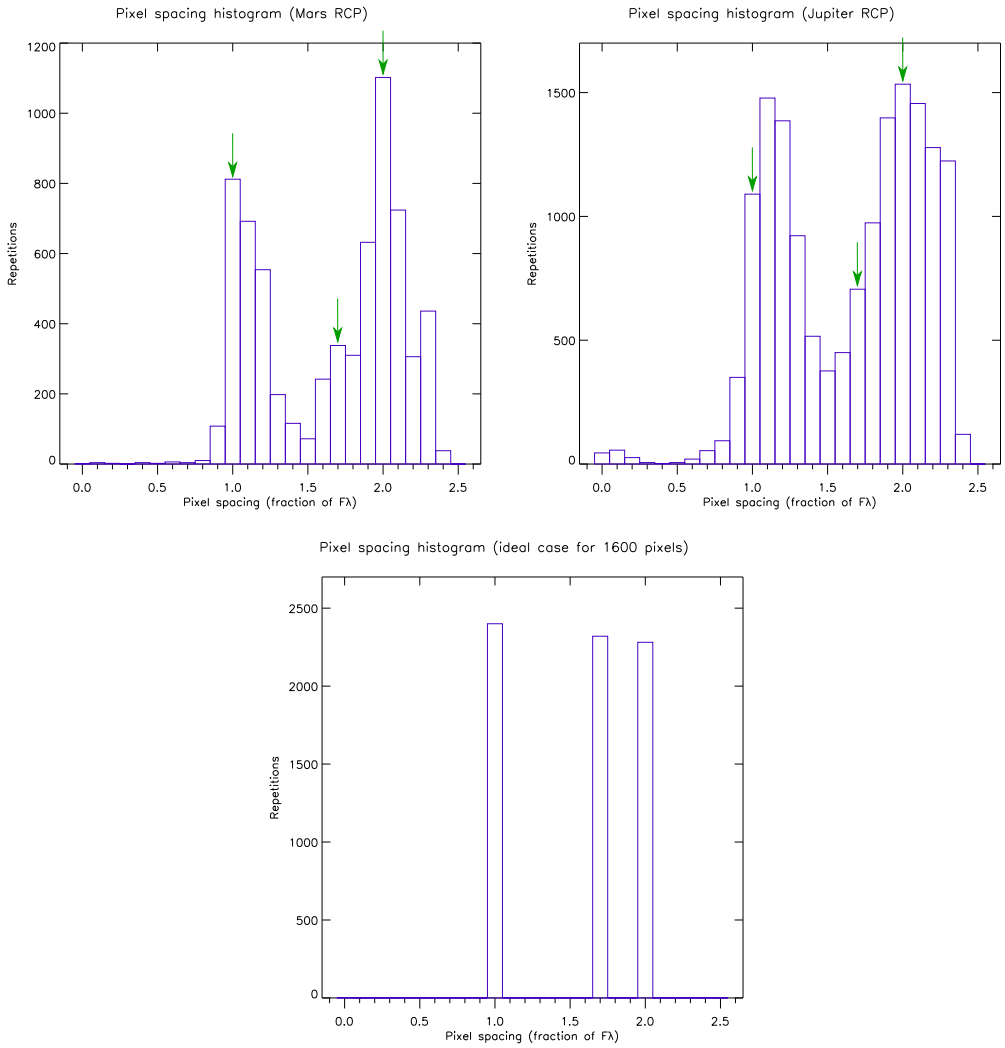

FIGURE 3.25— Pixel spacing histograms. The spacing is counted in fractions of $F\lambda$. Upper right panel: pixel spacing distribution from the Jupiter RCP of figure 3.6. Upper left panel: pixel spacing distribution from the Mars RCP shown in figure 3.8. Bottom panel: Ideal pixel spacing histogram; it results from the pixel spacing calculation of the ideal grid shown in figure 3.26. The green arrows in the upper histograms show where the theoretical positions of the peaks should be. All the distances between pixels were calculated but the histogram is truncated to the shortest three ones.

to see their distribution. For this exercise we could not use the resulting distorted grid of the simulated FoV on sky (shown in figure 3.7), because the pixel arrangement was squared and not hexagonal as it is in our detector.

On this new grid the same exercise was done as for the Jupiter and Mars RCPs; all the distances between the pixels were calculated and a histogram was computed with them. In the histogram, shown in figure 3.25 (lower panel), three peaks can be clearly distinguished; the first one corresponds to closest distance between pixels and therefore, the pixel spacing (1 $F\lambda$); the second, which is within the error bar of $(1.7 \pm 0.05)\, F\lambda$, corresponds to the distances between two aligned pixels with one row in between; and the third one, which is 2 $F\lambda$, corresponds to the distances between two pixels separated by two times the pixel spacing. To better understand these three cases see the lower panel of figure 3.26, where the pixel distribution can be clearly examined.

If the histogram coming from the real FoV (Jupiter and Mars) is compared to that coming from the ideal grid the following conclusions can be drawn (green arrows show the theoretical position where the peaks should be: 1.0 $F\lambda$, 1.7 $F\lambda$ and 2.0 $F\lambda$):

1. The first peak, which corresponds to the pixel spacing, suitably agrees with the theoretically expected peak in the two RCPs (see the first green arrow in figure 3.25). It is true that the histograms from the real FoVs have some dispersion around the peak, but since our FoV is a bit distorted, this affects the pixel spacing, which can be a bit larger or smaller depending on in which part of the array the measurement is done. In the Jupiter RCP, since the first peak is at 1.1 $F\lambda$, this can also be interpreted such that the lower tail of the dispersion of the 1.7 $F\lambda$ peak slightly merges with the upper dispersion tail of the 1.0 $F\lambda$ peak, shifting the peak to the next bin in the histogram. This effect does not occur in the Mars RCP. It can be understood because less pixels are available for that RCP and therefore the distortion may be reduced, making the dispersion tails shorter.

2. The second and the third peak, which are clearly distinguished in the simulated histogram, are rather merged in the histograms from the real FoVs. Again, the FoV distortion creates a dispersion around the peak, and now, since the peaks are closer, the upper dispersion tail of the 1.7 $F\lambda$ peak and the lower dispersion tail of the 2.0 $F\lambda$ peak blend each other, making their distinction difficult. Despite the merging tails, it can be noticed that in both real cases (Jupiter and Mars RCPs) the peak at 1.7 $F\lambda$ is decreased. An explanation for that could be the lack of pixels in these RCPs; if we look at the RCPs with more detail it seems that some lines of pixels are missing, and therefore the pixel-distance distribution is altered as compared to the theoretical one.

For further comparison, a distortion as shown in the left panel of figure 3.27 was applied to the ideal grid of figure 3.26. The histogram resulting from the calculation

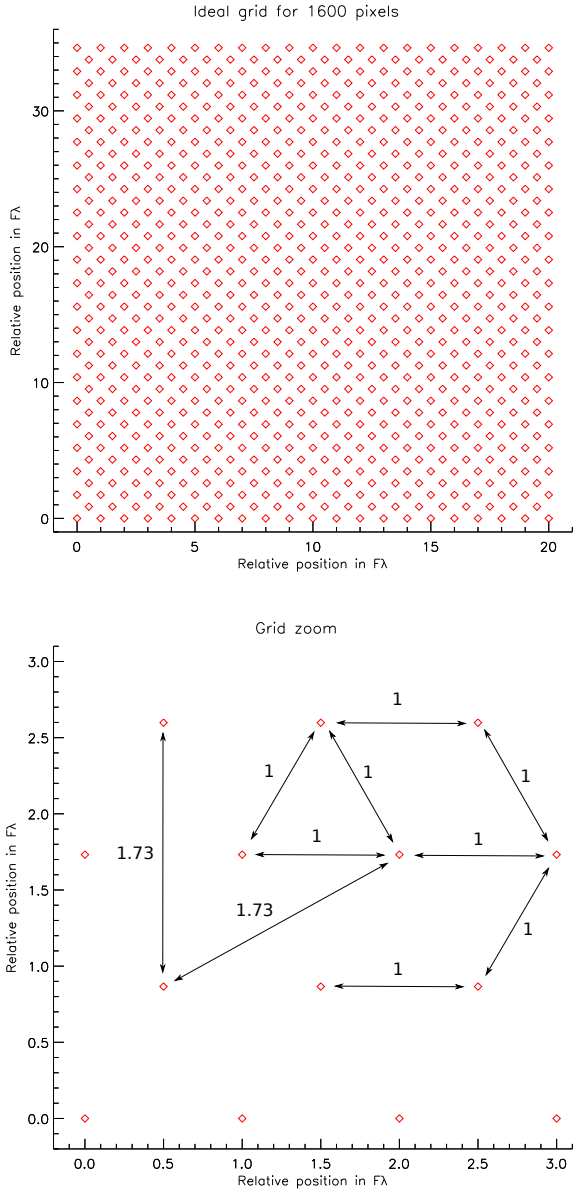

FIGURE 3.26— Upper panel: Ideal grid for $\sim$ 1600 pixels. Lower panel: zoom on the upper grid, showing the theoretical pixel distances in $F\lambda$.

of the pixel distances was computed and the result is shown in the right panel of figure

3.27. The distortion applied was around 15%, but only in the X direction, therefore it is not completely representative for the real situation. Nevertheless, it can be seen that the peaks have some dispersion, and also that the second and the third peak start to merge.

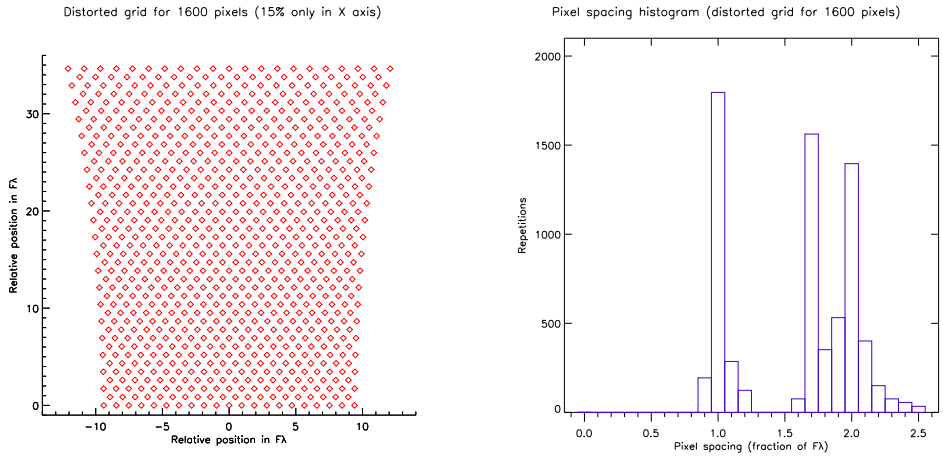

FIGURE 3.27— Left panel: simulated distorted grid (roughly 15% distortion on X axis). Right panel: pixel-distance histogram resulting from the distorted grid.

3.3 NGC 3603: a first comparison

In order to go one step further and to compare the results of our camera with other cameras some maps of the well known NGC3603 nebula, a giant H_{II} region, were done. The initial idea was to observe M17 (another well known nebula), motivated by a wide study of the dust component in this region (see next chapter). However, considering that in the commissioning period the source was only available during the sun avoidance of the telescope another source had to be selected.

NGC3603 is a nebula composed of a glowing cloud of gas and dust, which in the center houses an important stellar cluster; it is an active site of Galactic star formation. The nebula is situated in the Carina spiral arm of the Milky Way at roughly 7.6 kpc distance.

3.3.1 Map comparison

In figure 3.28 the resulting image from the A-MKID camera, reduced with the MARS software still under development, is shown; this image was obtained with the LFA detector of the camera (870 μm; the only one available during the commissioning

period) in 9432 seconds of integration time. The best RMS obtained in the data reduction of this source was approximately 80 mJy/beam.

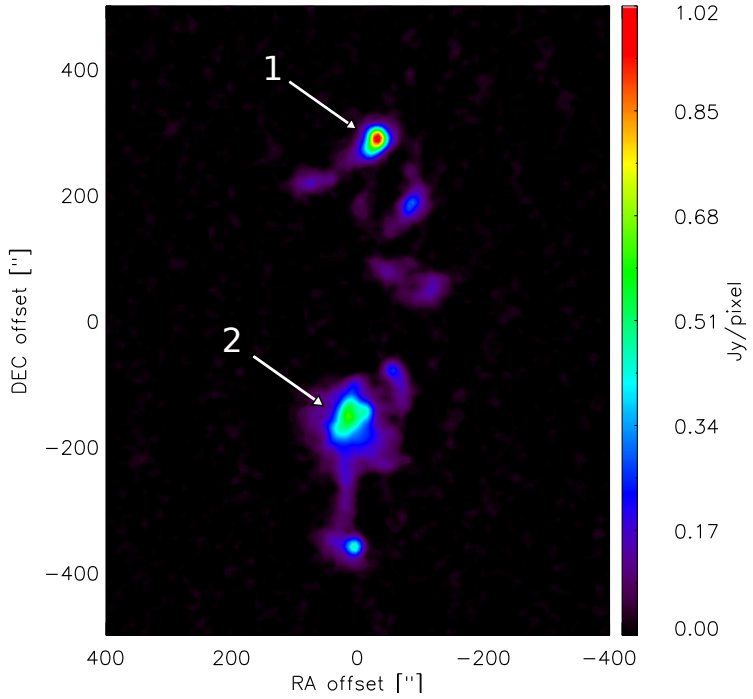

FIGURE 3.28— A-MKID map of NGC3603. Numbers 1 and 2 indicate the two brightest spots of the region.

For the first comparison the LABOCA map of the same source was used (figure 3.29 left). Both cameras are working at the same frequency (345 GHz or 870 μm wavelength) and are mounted at the same telescope, which is extremely useful for a direct comparison between both instruments. The NGC3603 data from LABOCA was available and after its reduction with the BOA[3] software the corresponding map could be computed. For the LABOCA map the integration time was 7310 seconds and the RMS roughly 25 mJy/beam. It is important to mention that in both reduction softwares (Mars and BOA) the noise filtering algorithms were very similar.

Comparing both maps it can be seen that there is some extended emission in the LABOCA map which is not present in the A-MKID map (filaments and emission called A, B, C, D and E in the LABOCA map). It seems that more integration time

[3] http://www3.mpifr-bonn.mpg.de/div/submmtech/software/boa/boa_main

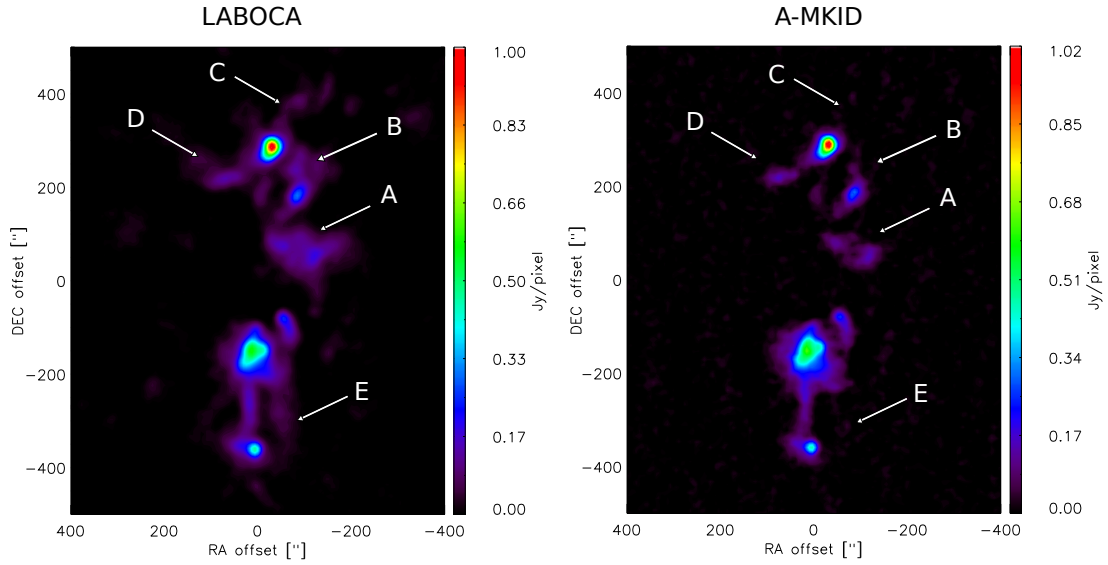

FIGURE 3.29— Left panel: LABOCA NGC3603 map. Right panel: A-MKID NGC3603 map (same as figure 3.28). A, B, C, D and E indicate some extended faint emission of the source which is present in the LABOCA map but not in the A-MKID map.

would be needed to recover these faint parts with the A-MKID camera. In turn, with better sensitivity (less RMS) in its detectors these parts would be recovered within the same or even less integration time which is the final goal of the camera.

Regarding the bright spot in the southern half (called spot 2 in the A-MKID map) the A-MKID map presents some emission around it which is not really present in the LABOCA map. This emission seems to contain some stripes in the horizontal direction; it gives the impression that it is an artifact that could come either from a bad characterization of some detectors (pixels) or from the data reduction itself. It is difficult to figure out what is exactly the reason because this artifact only appears in spot 2 but not in spot 1 (see the A-MKID map, figure 3.28).

Nevertheless, in order to be sure that this feature is really an artifact some more images were obtained for further comparison. From the Herschel public archive the already reduced PACS map at 160μm (figure 3.30) and the SPIRE maps at 350 μm and 500 μm (figure 3.31) were obtained.

If we compare the spot 2 of these images (especially in PACS-160 μm and in SPIRE-350 μm; the resolution of SPIRE-500 μm is too low, $\sim$ 36″ FWHM) with the same spot of the A-MKID and LABOCA maps, it can be seen that the emission rather follows the shape of the LABOCA map. From this can be concluded that the strip shape of the emission surrounding the spot 2 of the A-MKID map is an artifact, which

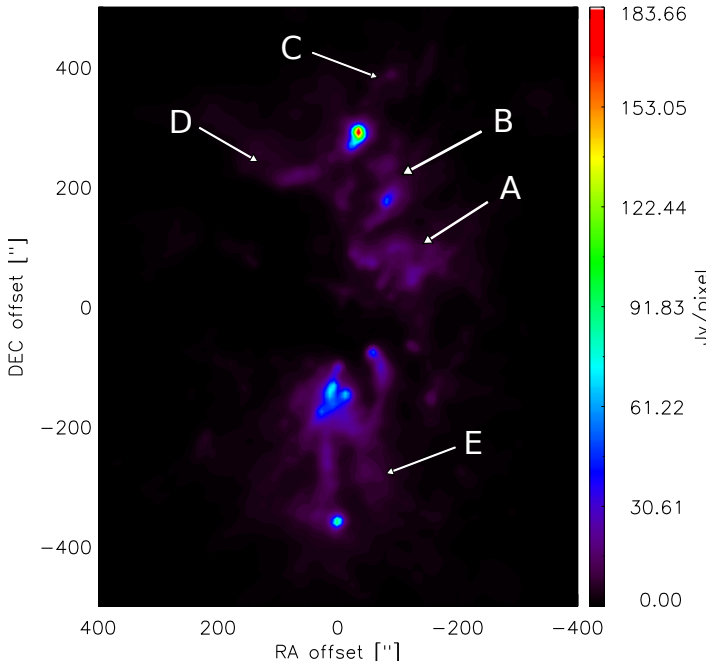

FIGURE 3.30— PACS-160 µm NGC3603 map. A, B, C, D and E indicate some extended faint emission of the source which is not present in the A-MKID map (same as figure 3.29). The FWHM of the PACS-160 µm instrument is 13″.

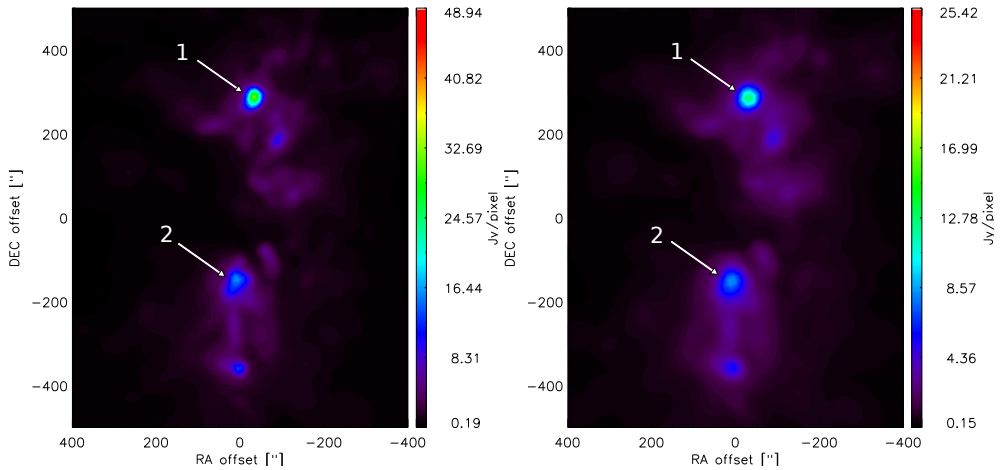

FIGURE 3.31— Left panel: SPIRE-350 µm NGC3603 map. Right panel: SPIRE-500 µm NGC3603 map. Numbers 1 and 2 indicate the two brightest spots of the region (same spots shown in figure 3.28).

needs further study to really understand its origin.

These new images also verify that the extended emission, which appears in the LABOCA map (A, B, C, D and E regions) and not in the A-MKID map, is real and that it is not an artifact of the LABOCA map; actually it would have been an unlikely option. This simply indicates a lack of integration time or sensitivity with the A-MKID camera (RMS of 80 Jy/Beam with A-MKID camera versus 25 Jy/Beam with LABOCA).

3.3.2 Calibration

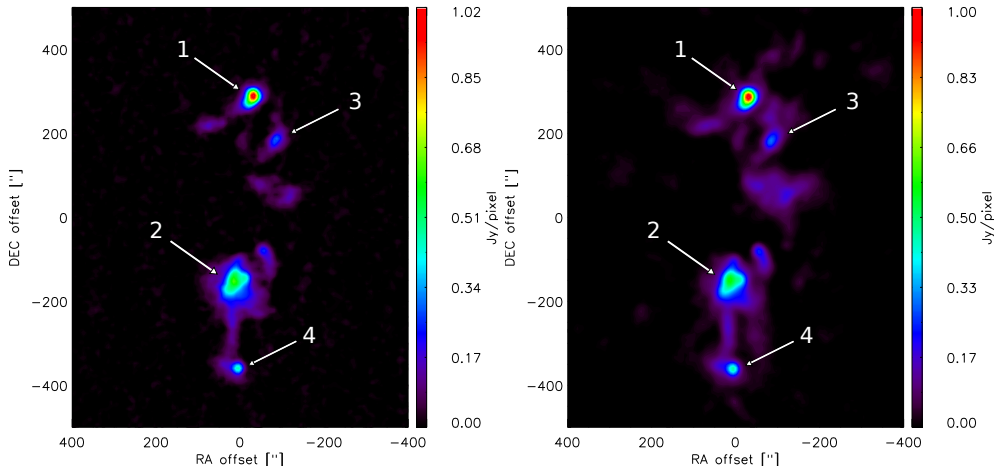

FIGURE 3.32— A-MKID (left) and LABOCA (right) maps of NGC3603. On each map the four different spots for calibration comparison are indicated.

Another point that can be compared between the LABOCA map and the new A-MKID map is the calibration. For that purpose the same four spots were selected in both maps, and the flux from the brightest pixel in each spot was measured (see figure 3.32). In the table 3.10 the results for the flux measurements are shown; it can be seen how the fluxes are pretty much in agreement between the two maps (less than 9% of difference in the worst case) and therefore, it can be concluded that the calibration was properly applied and that it is reliable.

3.3.3 Final statement

Despite the stripe issue of the spot 2, the A-MKID map is in accordance with the other available observations, and therefore could be considered a reliable map. Some improvement has to be done mainly in terms of sensitivity to achieve a competitive

TABLE 3.10— A-MKID and LABOCA calibration comparison. Fluxes from the brightest pixel of the four different spots of figure 3.32 are shown.

Position	LABOCA map (Jy/pixel)	AMKID map (Jy/pixel)
Spot 1	0.996	1.019
Spot 2	0.579	0.637
Spot 3	0.307	0.305
Spot 4	0.465	0.464

camera; nevertheless, since no strange artifacts appear after the data reduction, it can be concluded that the camera performance is on the right way.

3.4 Summary and conclusions

1. The overall FoV distortion agrees with the distortion expected from our model ($\sim 13\%$ on average).

2. Some beam maps were computed from fully sampled maps of several planets (Mars, Uranus and Jupiter). It could be seen that the main beam is not a perfect circle and it features an ellipticity $\sim 11\%$.

3. Measuring on the beam maps, it could be seen that the main beam accumulates the $\sim 85\%$ of the flux. Do not confuse that with the main beam efficiency, where the complete radiation pattern of the antenna is needed for its calculation.

4. Beams using a few pixels in the corners of the array were also computed. It could be seen that the beam shape is not constant along the array; the ellipticity varies from $\sim 7\%$ to $\sim 25\%$.

5. Comparing results with simulations, it was found that a better optical response should be expected. After some tests with the simulation software, the conclusion drawn is that our system suffers from some aberration due to some misalignments. Therefore, better alignment is required.

6. The signal to noise ratio of the detectors was not constant during the commissioning and also was varying in different parts of the array. A better characterization of the detectors is needed.

7. The angular resolution is $\sim 18.3''$; nevertheless some care should be taken with this result due to the ellipticity of the beam, especially in some parts of the array.

8. A pixel spacing around 1 $F\lambda$ was measured, which agrees with our model. However, due to the FoV distortion and the lack of pixels in some cases, the distribution of the pixel distances was different from the theoretical model.

9. An observation of an astronomical target was done. The target was the NGC 3603 nebula. A map was obtained with the MARS reduction software. Comparing the A-MKID map with other available data of the source some conclusions could be drawn:

   – Better sensitivity is required to recover some extended and faint emission, also to save observation time, and therefore, to be a more competitive camera.

   – On small scales an unexpected stripe artifact appears around one of the brightest spots of the source. Its origin it is not clear yet: it could be related either to the data reduction or the bad characterization of some pixels.

   – The calibration of the A-MKID fluxes is consistent with that obtained with LABOCA, and no problems are expected from this side.

   – Although some improvement is needed, in general terms the performance of the camera is on the right way.

4

The dust component of M17 SW

4.1 Introduction

M17 is a young and massive Galactic star-forming region located in the constellation of Sagittarius, also popularly called the Omega Nebula or the Swan Nebula (see figure 4.1). It is considered one of the brightest IR and thermal radio sources on the sky, and also one of the most massive star-forming regions of our Galaxy (Povich et al. 2007).

The central area of the nebula is composed by an H_{II} region which is ionized by a highly obscured cluster of several OB stars ($\geq$ 100 stars) (Beetz et al. 1976 and Hanson et al. 1997). Seven O-stars are found in the center of the cluster (Hanson et al. 1997).

On each side of the star cluster two large structures can be distinguished. They represent the photodissociation regions (PDRs) resulting from the interaction of the expanding H_{II} region with two molecular clouds: M17 North (N) and M17 Southwest (SW). Both regions meet each other at an apparent angle of 45° forming an inverted V-shape (Povich et al. 2007).

The M17 SW region is a giant molecular cloud which is located at a distance of 1.98 kpc (Xu et al. 2011). Due to its nearly edge-on geometry and the large amount of observational data available in the literature, M17 SW is one of the best candidates in our Galaxy to study the entire structure of PDRs, from the heating sources (surrounded by an H_{II} region) through the photodissociation front to the molecular region (Pérez-Beaupuits et al. 2010).

A large amount of research has been done on this source:

1. Several observations of the dust continuum (infrared and submillimeter range) have been done since the 70's. Low & Aumann (1970) and Harper & Low

(1971) performed the firsts far infrared observations of M17. Harper et al. (1976) an Gatley et al. (1979) mapped M17 SW in the mid and far infrared. In the 80's the IRAS satellite provided infrared maps of the whole sky where the dust distribution of the M17 could be observed (because of the low sensitivity no information from the faintest regions could be extracted). More recently, with the Spirit III instrument on board the *MSX* (Price et al. 2001) and through the GLIMPSE survey made with *Spitzer* IRAC (Fazio et al. 2004) several infrared maps with better resolution and sensitivity were obtained. Also, observations in the submillimeter range were performed. CO maps with JCMT observations were obtained by Wilson et al. (1999). Dupac et al. (2002) mapped M17 complex with the balloon-borne telescope PRONAOS (low angular resolution, $3'$) in four submillimeter bands and derived both temperature and spectral index maps.

2. Povich et al. (2007) combine diverse infrared data in order to synthesize a global spectral energy distribution of the M17 complex. They also studied the PAH emission morphology in the cloud. Further studies by the same author found a number of young stellar objects in the vicinity of the central star cluster (Povich et al. 2009).

3. Different studies based on the analysis of low-J CO lines have been done in order to estimate the temperature of the gas. A temperature range of 50-60 K was estimated towards the M17 SW cloud core, whereas 30-35 K was the estimated mean cloud temperature (e.g. Guesten & Fiebig 1988; Bergin et al. 1994; Snell et al. 2000). Temperatures of $\sim$ 275 K were estimated from NH_3 observations (Guesten & Fiebig 1988) towards the VLA 21cm continuum arc (Brogan & Troland 2001)

4. Diverse studies of molecular excitation and emission line profiles from the M17 SW core have been carried out (e.g. Martin et al. 1984; Stutzki & Guesten 1990). They indicated that the structure of gas is highly clumped rather than homogeneous. Reid & Wilson (2006) mapped a portion of this source (5.5 x 5.5 pc) in the submillimeter dust continuum emission and determined the mass of around 100 dusty clumps.

5. The FUV radiation field, G_0, was estimated by Meixner et al. (1992). They obtained a value in the order of 10^4 in units of the equivalent Habing flux (1.6×10^{-3}ergs cm^{-2} s^{-1}, which is the flux calculated by Habing (1968) for the local ambient interstellar radiation field).

The object of our study is the dust component in M17 SW, from the H_{II} region

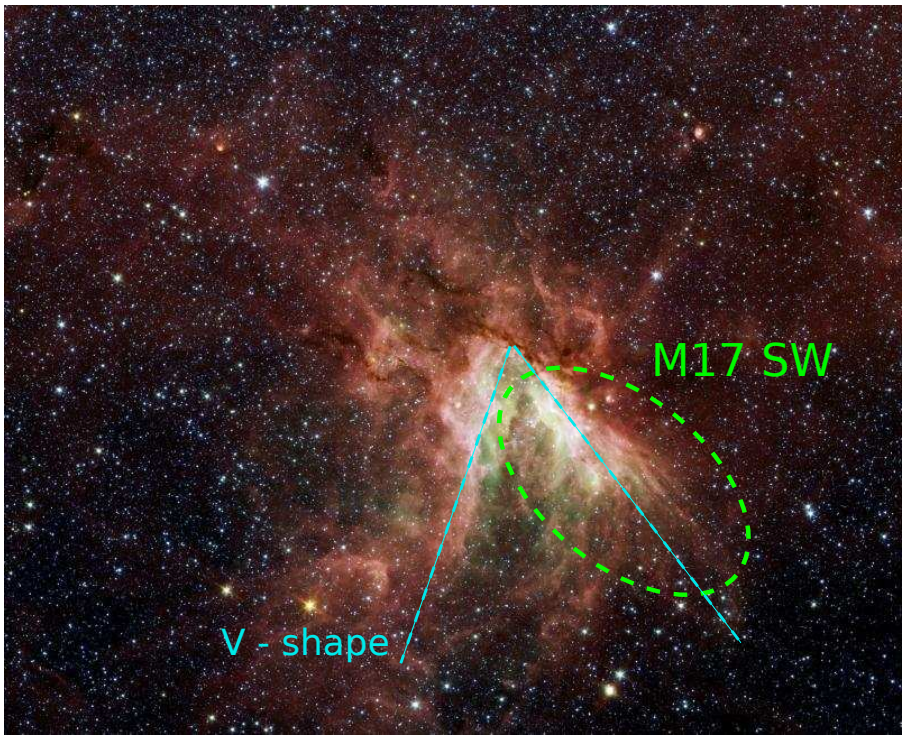

FIGURE 4.1— General view of M17 in the near infrared. This picture was taken with Spitzer's infrared array camera. It is a four-color composite, in which light with a wavelength of 3.6 μm is blue; 4.5 μm light is green; 5.8 μm light is orange; and 8 μm light is red. Dust is red, hot gas is green and white is where gas and dust intermingle. The foreground and background stars in the image are not related to M17. M17 is also known as the Omega Nebula or the Swan Nebula. In the image the region of our study, M17 SW is indicated. Also the V-shape, previously commented, can be noticed. Image credit: NASA/JPL-Caltech/Univ. of Wisc.

(where the dust is practically nonexistent) to the dense parts of the molecular cloud, crossing the PDR front. As discussed before, extensive investigations have been done on M17 and particularly on M17 SW. However, all studies related to the dust continuum were done at large scales, using large beam sizes and computing global results. Here, we present a detailed dust continuum study across the PDR in order to analyze how the dust characteristics change through the photodissociation front.

Since M17 SW is a very well known region the initial idea was to observe it with our new camera (A-MKID) and to create two maps, one with the LFA (Low Frequency Array at 850 μm) and the other one with the HFA (High Frequency Array at 350 μm). The purpose of that was on one hand, to compare (for calibration and sensitivity purposes) the LFA map with the LABOCA map (see figure 4.2), which

works at the same frequency, and on the other hand, to include these two maps in the study presented in this chapter in order to improve our analysis. However, during the first commissioning of the A-MKID camera (APEX, December 2013) M17 SW was visible only during the sun avoidance period and these observations could not be performed for (antenna) security reasons. However, M17 SW will be one of the prime targets for the commissioning of the A-MKID camera during this year 2014.

It is also important to mention that for structures larger than the telescope beam the mapping speed of the LFA would be, on one hand, a factor ~ 10 faster than that of LABOCA and on the other hand, a factor ~ 500 faster than that of SABOCA (the APEX continuum camera at 860 GHz) for the HFA, which really introduces a big improvement. Also, it is remarkable that observations with the LFA and the HFA will be performed simultaneously, considerably saving observation time. In general, we can say that as soon as the goals are achieved the new camera will be much more efficient than the current receivers.

4.2 Observations, data reduction and analysis method

4.2.1 Data

For this study different maps covering the range between the near infrared and the millimeter/submillimeter were used. Maps from Spitzer-IRAC (4.5 μm and 5.8 μm), MSX satellite (8.0 μm, 12.0 μm, 15.0 μm and 21.0 μm), Herschel-PACS (70 μm and 160 μm) and LABOCA (850 μm) were selected; in some cases values from Herschel-SPIRE (500 μm) were also included. All maps were taken from the corresponding public archive except for the LABOCA map, where data reduction and calibration processing was needed. The rest of the maps was already reduced. In figure 4.2 the LABOCA map resulting from our reduction is shown; the reduction was done using the BOA[1] software (BOlometer Array Analysis Software).

The following procedure was done for all the maps in the same way. The maps were converted to the same units, [Jy/pixel], to compute the flux densities. All the maps were convolved to the beam of the map with worst resolution, which was the LABOCA map (850 μm) with a beam size of 19 arcsec (HPBW).

Flux densities were extracted along a linear cut at position angle (P.A.) 90° (E from N) across the PDR front (see figures 4.3, 4.4 and 4.5). This direction was chosen in order to cover a representative part of the region, from the H_{II} region to the molecular cloud through the PDR. The reference position for all our maps was the star SAO 161357: RA(J2000) = 18:20:27.6 and Dec(J2000) = -16:12:00.9. The coordinates of our observations (hereafter strip of measurements) were taken at offsets (relative to the

[1] `http://www3.mpifr-bonn.mpg.de/div/submmtech/software/boa/boa_main.html`

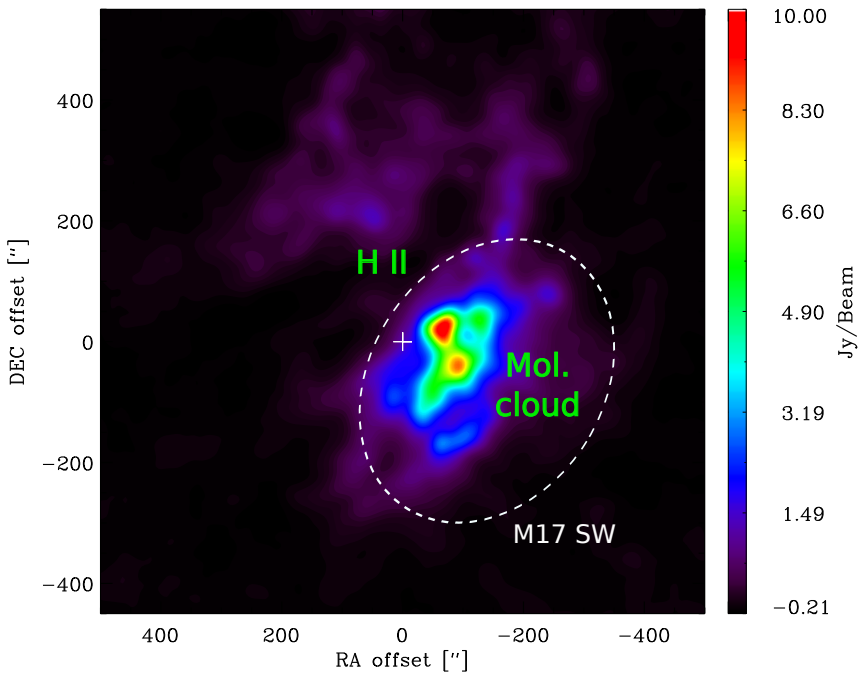

FIGURE 4.2— M17 map from LABOCA after our reduction. The coordinates are relative to the star SAO 161357 (white central cross): RA(J2000) = 18:20:27.6 and Dec(J2000) = -16:12:00.9. Flux density units are *Jy/Beam*. The BOA software was used for the data reduction. On the figure the region of our study, M17 SW, is indicated. The H_{II} region and the molecular cloud are also shown. The PDR front is located between these two regions.

reference position) of $+30''$ in declination and from $+60''$ to $-200''$ in right ascension, in steps of $-20''$.

The same aperture size of 20 arcsec diameter was used for all the flux density measurements, slightly larger than the resolution of LABOCA (19 arcsec).

The main information of the maps used is summarized in table 4.1.

In figures 4.3, 4.4 and 4.5 three of the ten aforesaid frequency maps (in Jy/pixel) are shown: 4.5 μm, 70 μm and 870 μm. These maps show how the morphology of the source changes at different wavelengths; it can be noticed that the brightest region is slightly displaced to the west as the wavelength increases. The apertures and positions where the fluxes were extracted are depicted by white circles.

For each flux density measurement its per log-frequency value, νF_ν in $[\mathrm{W/m^2}]$, was calculated and therefore the spectral energy distribution (SED) for each position could be obtained.

TABLE 4.1— Main characteristics of the maps used in our study.

Instrument	Wavelength (μm)	Flux units	Angular resolution ($''$)	Pixel size ($''$)
Spitzer-IRAC	4.5	MJy/sr	2	0.60
Spitzer-IRAC	5.8	MJy/sr	2	0.60
MSX	8.28	$W/(m^2 \cdot sr)$	20	6.00
MSX	12.13	$W/(m^2 \cdot sr)$	20	6.00
MSX	14.65	$W/(m^2 \cdot sr)$	20	6.00
MSX	21.3	$W/(m^2 \cdot sr)$	20	6.00
Herschel-PACS	70	$Jy/pixel$	5	3.20
Herschel-PACS	160	$Jy/pixel$	13	6.40
Herschel-SPIRE	500	$Jy/beam$	36	14.00
APEX-LABOCA	870	$Jy/beam$	19	4.55

According to Povich et al. (2007) and Cohen et al. (2007) there are some systematic calibration errors in the IRAC maps, where the flux tends to be overestimated. As in Povich et al. (2007) the SSC "infinite-aperture" correction factors determined by Jarrett[2] were adopted for the IRAC maps, and the flux values at 4.5 μm and 5.8 μm were multiplied by factors of 0.94 and 0.73 respectively.

Povich et al. (2007) also shows that there is a strong emission of PAH in the 5.8 μm and 8.0 μm components, and that the 4.5 μm component (free of PAH emission) is contaminated by the H_I Br-α recombination line (corresponding roughly to 20% of the total 4.5 μm emission). These two effects do not have the same impact. The PAH emission is present as soon as we move away from the H_{II} region, mainly after the PDR (moving from East to West in our strip, i.e., from the H_{II} region to the molecular cloud) where the cloud becomes denser and molecules start to appear. On the contrary, the H_I Br-α recombination line contribution increases towards the H_{II} region and decreases as we move away from that region.

Following Povich et al. (2007), three different factors were applied to correct the Br-α contribution to the 4.5μm component. For the positions close to the H_{II} region (positions 1 to 4) a 22% contribution was considered, for the positions in the middle (positions 5 to 10) a 19% contribution, and for the positions which were further out (positions from 10 to 14) a 15% contribution.

In order to compute the PAH contamination, a study of the 5.8 μm, 8.0 μm, 12.0 μm and 15.0 μm emission components was done. Figure 4.6 shows the following flux ratios along the strip: IRAC-5.8 / IRAC-4.5, MSX-8.0 / IRAC-4.5, MSX-

[2] http://ssc.spitzer.caltech.edu/irac/calib/extcal

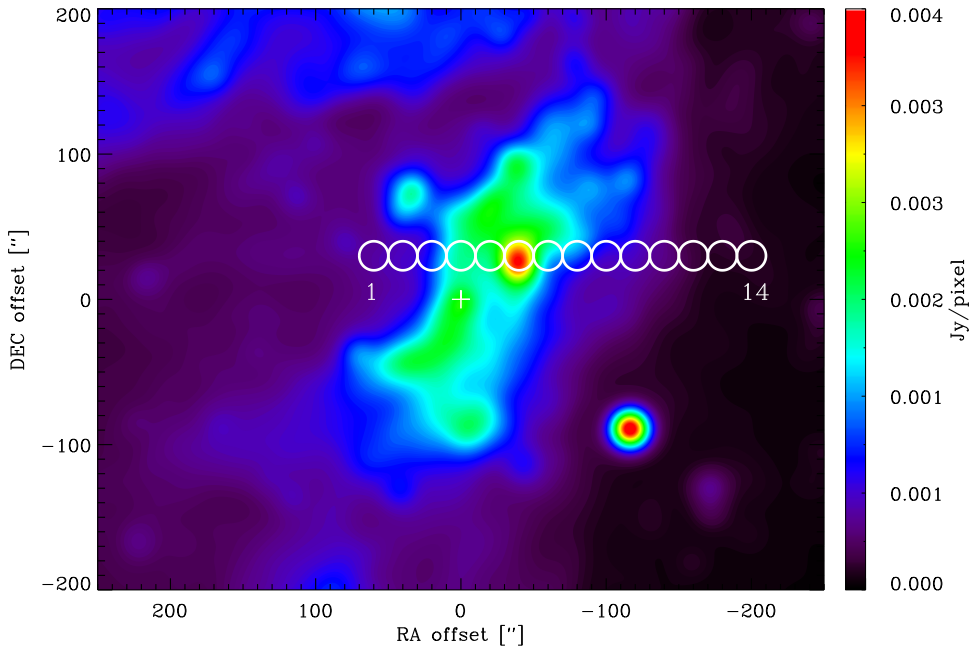

FIGURE 4.3— IRAC map at 4.5 μm. Flux density units are $Jy/pixel$. The coordinates are relative to the reference position (white central cross): RA(J2000) = 18:20:27.6 and Dec(J2000) = -16:12:00.9. White circles represent our strip of fourteen measurements (positions 1 - 14 from left to right).

12.0 / IRAC-4.5 and MSX-15.0 / IRAC-4.5. The IRAC-4.5 image was used for normalization because it is free of PAH emission (Povich et al. 2007). In the figure PAH emission can be clearly seen in the 5.8 μm and 8.0 μm components as soon as the dense region is reached, after the PDR (in the western part of our strip, i.e., to the right). In the 12.0 μm and 15.0 μm components the PAH contribution in the dense region is lower or may be hidden by the strong dust emission coming from the PDR (center of the strip), as it seems to happen in the 12.0 μm component.

Since the PAH contribution is strong (and also quite variable) for the short wavelengths (not for the 4.5μm component) as the molecular cloud is approached, some of the flux measurements were considered as an upper limit for the fitting process: This is the case for the 5.8 μm and 8.0 μm components from the position 9 onwards, and for the 12.0 μm component from the position 11 onwards.

Another point to take into consideration is the contribution of the CO $J = 3-2$ line to the LABOCA map. The LABOCA map covers a frequency range between 313 and 372 GHz and the CO $J = 3-2$ line is at 345.8 GHz. It is important to know the contribution of that line and in case of being significant the map should be corrected

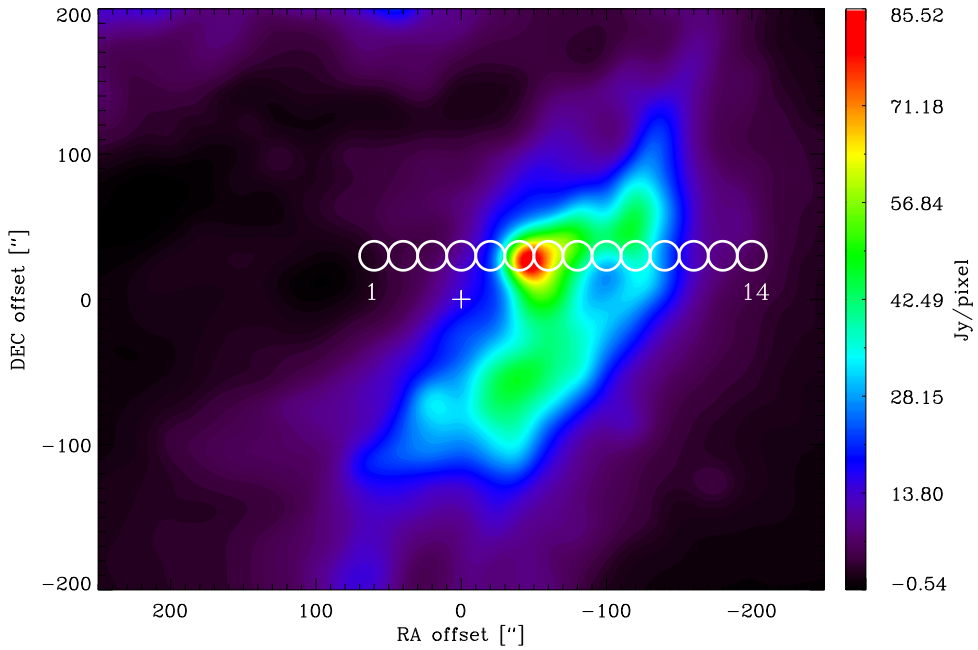

FIGURE 4.4— PACS map at 70 µm. Flux density units are *Jy/pixel*. The coordinates are relative to the reference position (white central cross): RA(J2000) = 18:20:27.6 and Dec(J2000) = -16:12:00.9. White circles represent our strip of fourteen measurements.

for that. From observations[3] of the CO $J = 3-2$ line in M17 SW, its contribution in the LABOCA map could be computed: it is roughly $\sim 3\%$ in the PDR front and then progressively increases until roughly $\sim 13\%$ in the last measured position of our strip (position 14). Due to the low contribution of the CO $J = 3-2$ line to the LABOCA map it was finally decided not to correct for that. It is important to remark that a 20% error is considered in all the flux measurements and that therefore the CO $J = 3-2$ line contribution remains always within the error margin.

4.2.2 Black/gray body fitting

In order to estimate the dust temperature, a black/gray body model was fitted to the dust SED of each position. After different attempts a model composed of two gray-body laws (i.e., modified blackbody laws) was assumed for all of our positions measured in order to characterize each SED. Each gray-body is characterized by a cold and a hot component: The M17 geometry is complex (see section 4.1) and due to the seven

[3]Observations made with FLASH, also at the APEX Telescope; `http://www.apex-telescope.org/instruments/pi/flash/`

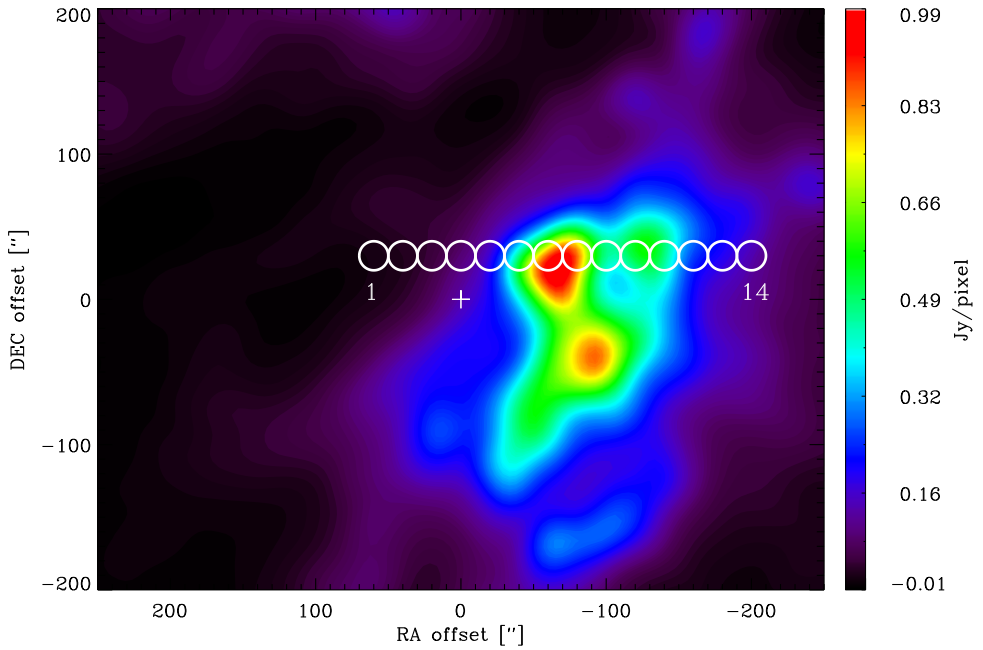

FIGURE 4.5— LABOCA map at 870 μm. Flux density units are $Jy/pixel$. The coordinates are relative to the reference position (white central cross): RA(J2000) = 18:20:27.6 and Dec(J2000) = -16:12:00.9. White circles represent our strip of fourteen measurements.

O-stars in the center of the H_{II} region, which are heating the PDR, it is natural to find different layers at different temperatures, all of them contributing to the shape of the dust SED. According to the number of maps used (number of frequencies) the most reasonable approximation was to characterize each SED with two components. To add a third component would increase the degrees of freedom of our fittings, but consequently, the quality of them would be reduced (too many degrees of freedom for the given number of measurements). Since it is a diffuse region and, as we will see later, considered optically thin at the selected wavelengths, the two components were treated as gray-body laws.

In the literature it is common to find the modified blackbody law in order to characterize the dust emission (e.g. Dupac et al. 2002; Shetty et al. 2009a). A blackbody could be included as third component in order to compute the temperature of some particular hot cores along the PDR. However this option was rejected because it involved too many degrees of freedom in the fitting process and consequently a loss of quality in our fittings.

The modified blackbody (or gray-body) law takes the form:

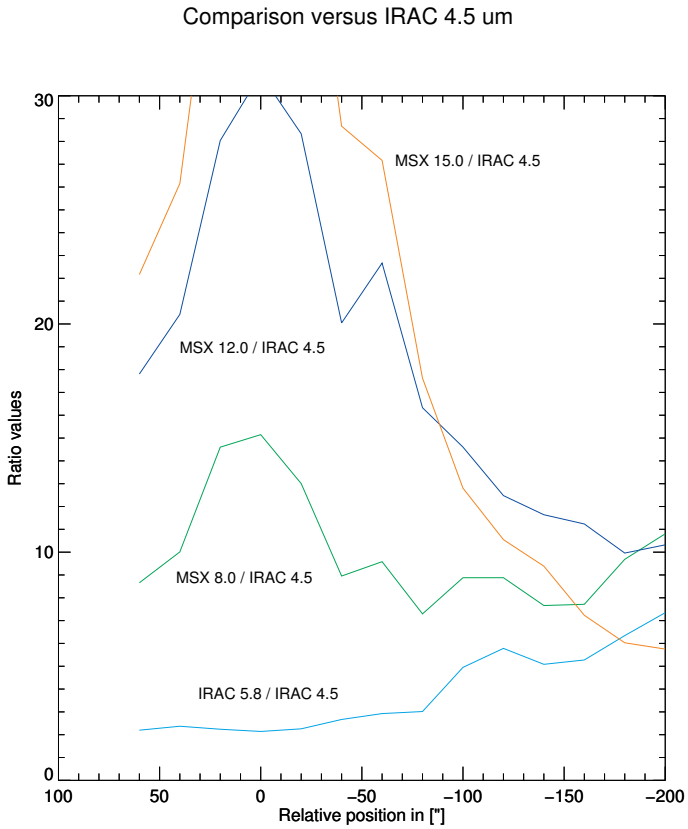

FIGURE 4.6— Mid-infrared fluxes relative to the IRAC-4.5μm fluxes along E - W cuts of the IRAC-5.8, MSX-8.0, MSX-12.0 and MSX-15.0 images. From the relative position $\approx -100''$ to the right PAH emission can be found clearly in the IRAC-5.8 and MSX-8.0 components.

$$S_\nu = \Omega B_\nu(T)\,\kappa_0 \left(\frac{\nu}{\nu_0}\right)^\beta \Sigma \tag{4.1}$$

where Ω is the solid angle of the observing beam, Σ is the mass column density of the emitting material, $\kappa_0 \left(\frac{\nu}{\nu_0}\right)^\beta$ is the frequency-dependent opacity of the dust (κ_ν) (Shetty et al. 2009a, further references therein), β is its spectral index and $B_\nu(T)$ is the Planck function:

$$B_\nu(T) = \frac{2h\nu^3}{c^2} \frac{1}{e^{\frac{h\nu}{kT}} - 1} \tag{4.2}$$

The frequency-dependent opacity term, $\kappa_0 \left(\frac{\nu}{\nu_0}\right)^{\beta}$, is defined by the opacity κ_0 at a reference frequency ν_0. For this purpose the frequency of LABOCA was used, 345 GHz (870 μm).

Therefore, the model used to do our fitting is composed of the sum of two gray-body laws, one for each component (cold and hot component):

$$S_{\nu\ TOTAL} = S_{\nu\ COLD} + S_{\nu\ HOT} \tag{4.3}$$

(hereafter $S_{\nu\ COLD} \rightarrow S_{\nu\ 1}$ and $S_{\nu\ HOT} \rightarrow S_{\nu\ 2}$)

The independent variable of our equation was the frequency (ν), and three more degrees of freedom per component were considered in oder to fit our SEDs with the 2-gray-body model:

1. $S_{\nu\ 1}$ component: T_1, β_1 and the parameter $C_1 = \kappa_0 \Sigma_1$,
2. $S_{\nu\ 2}$ component: T_2, β_2 and the parameter $C_2 = \kappa_0 \Sigma_2$,

where C_1 and C_2 are the optical depths of the cold and hot components, respectively, at the reference frequency ν_0. The remaining values were known:

1. Ω: For the solid angle the final resolution of our maps ($19''$) was used; all the maps were converted to the worst resolution, section 4.2.1. With the conversion factor 1 square arcsec $= 2.3504 \times 10^{-11}$ sr the solid angle subtended by the beam could be calculated.
2. $c = 299792458$ m/s (speed of light).
3. $h = 6.62606957 \times 10^{-34}$ J $\cdot$ s (Planck constant).
4. $k = 1.3806488 \times 10^{-23}$ J/K (Boltzmann constant).

4.2.3 Starting point and procedure

Before starting the fitting process it was necessary to choose some initial values for our unknown parameters. It is important to set them to some coherent values to be sure that the least-squares fitting method finds the absolute minimum and that the best approximation is reached.

Temperature (T) and spectral index (β)

In the literature there is ample work about the relation between dust temperature and spectral index. Some authors (Dupac et al. 2002 and Dupac et al. 2003) claim that

there is an intrinsic inverse correlation between the dust temperature and the spectral index. Dupac et al. (2003) shows that this relation is well fitted by the hyperbola

$$\beta = \frac{1}{0.4 + 0.008T}\,. \tag{4.4}$$

They explain that several interpretations are possible for this effect. One is that the grain sizes change in dense environments; another one is that the chemical composition of the grain is not the same in different environments and that this affects the temperature; and the third and, according to the author, the most likely effect is an intrinsic dependency of the spectral index on the temperature.

Other authors (Shetty et al. 2009a and Shetty et al. 2009b) found this inverse relation as well, however, they affirm that this anticorrelation is due to the noise in the flux measurement. The fits to fluxes in the R-J regime ($h\nu \ll kT$, small frequencies) are very sensitive to observational uncertainties, such as noise, and this may produce a spurious inverse $T-\beta$ relationship. They explain that the hyperbolic relation found by Dupac et al. (2003) is not the only explanation for the $T-\beta$ relation and they even show other possible fits for the $T-\beta$ relation. Thus, their conclusion is that least-squares fittings to the observed dust SED may not be able to reveal any intrinsic correlation between β and T.

Shetty et al. (2009a) also mention another problem somehow related to the previous conclusion: As we said, least-square fits of dust SEDs obtained from fluxes estimated assuming the R-J regime are very sensitive to noise uncertainties and then several $T-\beta$ combinations could fit the same SED. To mitigate this effect the inclusion of shorter wavelengths observations would help, but then not only the dust emission would be measured in the observed flux: Embedded sources transiently heating up very small grain could as well contribute to the measured flux at wavelengths $\lambda \leq 100$ μm (Li & Draine 2001).

In conclusion, either because it is an intrinsic characteristic of the dust or maybe because of the uncertainties in the flux measurements, observational evidences indicate the existence of an inverse relation between T and β. Hence, to start our fitting process we set the cold component to $\beta_1 = 0.8$ and $T_1 = 100$, and the hot component to $\beta_2 = 0.3$ and $T_2 = 300$, following an inverse relation. In order to quantify these starting parameters the hyperbolic relation by Dupac et al. (2003) was used.

Opacity (κ) and column density (N)

As we discussed before (section 4.2.2), the frequency of LABOCA (345 GHz) was chosen as reference frequency. This frequency was introduced as ν_0 in the fitting function and the rest of the frequency dependent parameters (like κ_0) were referred to this frequency. A consistent value for C_1 and C_2 is needed to start our fitting iteration.

Shirley et al. (2011) estimate the dust opacity in the submillimeter range in their study. They compare infrared and submillimeter dust continuum observations of the low-mass Class 0 core, B335, in order to constrain the ratio of submillimeter to infrared opacity (κ_{smm}/κ_{ir}). Then, using the average value of theoretical dust opacity models at 2.2 μm, they constrain the dust opacity at 850 μm and 450 μm. The dust opacity found at 850 μm, which is very close to our reference, was $\kappa_{850} = (1.18 \text{ to } 1.77)^{+0.36}_{-0.24}$ cm^2/g. For our initial calculation the value 1.54 cm^2/g was used, which is the nominal value of the previous equation.

Regarding the column density (N) some information was found in the literature where column density values were calculated at our temperature (20-300 K) and frequency range. According to Evans et al. (2001), Dupac et al. (2001) and Peretto et al. (2010) a coherent value for this environment at this temperature and frequency range should be in the order of $N_{\mathrm{H_2}} \approx 10^{22}\mathrm{cm}^{-2}$; which is in agreement with values reported by Hollenbach & Tielens (1997).

We have to notice that this value is calculated as a number of hydrogen molecules. Then the gas mass column density is $\Sigma = N_{\mathrm{H_2}} \times \mu$; μ is the gas mass in grams per hydrogen molecule, according to Kauffmann et al. (2008) roughly 2.8 times the mass of atomic hydrogen (m_{H}), where 2.8 is the molecular weight per hydrogen molecule ($\mu_{\mathrm{H_2}}$), counting hydrogen, helium and metals[4].

$\mu = \mu_{\mathrm{H_2}} \cdot m_{\mathrm{H}} \approx 2.8 \times 1.673723 \times 10^{-24} g = 4.686424 \times 10^{-24} g$.

Thus, the initial value that we used in our iteration was:

$\Sigma = N_{\mathrm{H_2}} \cdot \mu = 10^{22}$ cm^{-2} $\times 4.686424 \times 10^{-24}$ g $= 4.686424 \times 10^{-2}$ g$\cdot$cm^{-2}.

Consequently, the initial value for C_1 and C_2 should be:

$C_1 = C_2 = \Sigma \cdot \kappa_{850} = 1.54$ cm^2/g $\times 4.686424 \times 10^{-2}$ g/cm^2 $= 7.217093 \times 10^{-2}$ (dimensionless).

Since C_1 and C_2 are fit parameters (i.e., the optical depths at the reference frequency), their order of magnitude is sufficient for an initial guess. Thus, they were set to $C_1 = C_2 = 1 \times 10^{-2}$.

Procedure

Once the initial values were set the least-squares fitting process was applied to each measured position in order to reach the best approximation to our SEDs.

In the fitting β is as a fixed parameter, because we realized that the quality of the fit increased with less free parameters. This is because there are not enough measurements to accept more components (free parameters). In each measured position β was adjusted according to the resulting temperature obtained (keeping the inverse relationship $T - \beta$) and the fitting quality parameters (see below).

[4]The value $\mu_{\mathrm{H_2}} = 2.8$ is valid only for molecular gas, but since we only want to determine an initial parameter the order of magnitude is sufficient and this value gives us a good approximation.

For the fitting process the logarithm of the flux densities of the SEDs was used instead of the nominal values, because the dynamic range of our flux data was too large, and therefore the least squares fitting method would put more weight to fit the higher values than the lower ones. This is because the difference between the measured value and the fitted value is larger in the higher values than in the lower ones. By using a logarithmic scale all the values are converted to the same order of magnitude, and this problem disappears.

To verify the quality of our fittings two plots were calculated in each fitting iteration:

1. Scatter plot of the observed values versus the estimated values. The ideal scenario would be when all the points are following the line $y = x$ ($slope = 1$ and $y - cut$ in 0), which would mean that the observed values are exactly the same as the estimated values. In our plots a linear function was fitted in order to see how far our measurement was from the ideal situation (see bottom left of figures 4.7, 4.8, 4.9 and 4.10).

2. Scatter plot of the residuals versus frequency. For each frequency the residual was calculated as $residual_i = \frac{(fitted-val_i) - (measured-val_i)}{(measured-val_i)}$. The ideal scenario in this case would be that for all frequencies the residuals are zero, which means that the observed values and the estimated ones are identical. In our plots the RMS was determined in order to see how good the fitting was in the iteration. The RMS was calculated as $RMS = \sqrt{\frac{\sum(residual_i)^2}{n-elements}}$ (see bottom right of figures 4.7, 4.8, 4.9 and 4.10).

4.3 Results and discussion

The method discussed in the previous section was applied and after some iterations the best fitting approximation was reached for each position.

In the figures 4.7, 4.8, 4.9 and 4.10 the fitting results for the 14 positions are presented. The plots show the logarithm of each SED (in black), $log(\nu F_\nu)$ (νF_ν in $[\mathrm{W/m^2}]$), versus frequency, ν in [Hz]. The total flux resulting from the combination of the two individual components (hot and cold) is shown in green (see equation 4.3). The fitting result of each component represented by a gray-body law is also shown (red). In each plot, the two measures of quality are calculated and plotted as well.

Looking at the figures it is clear that two components fit perfectly the SEDs from approximately position 6 onwards, but, as it was explained in section 4.2.2, also two

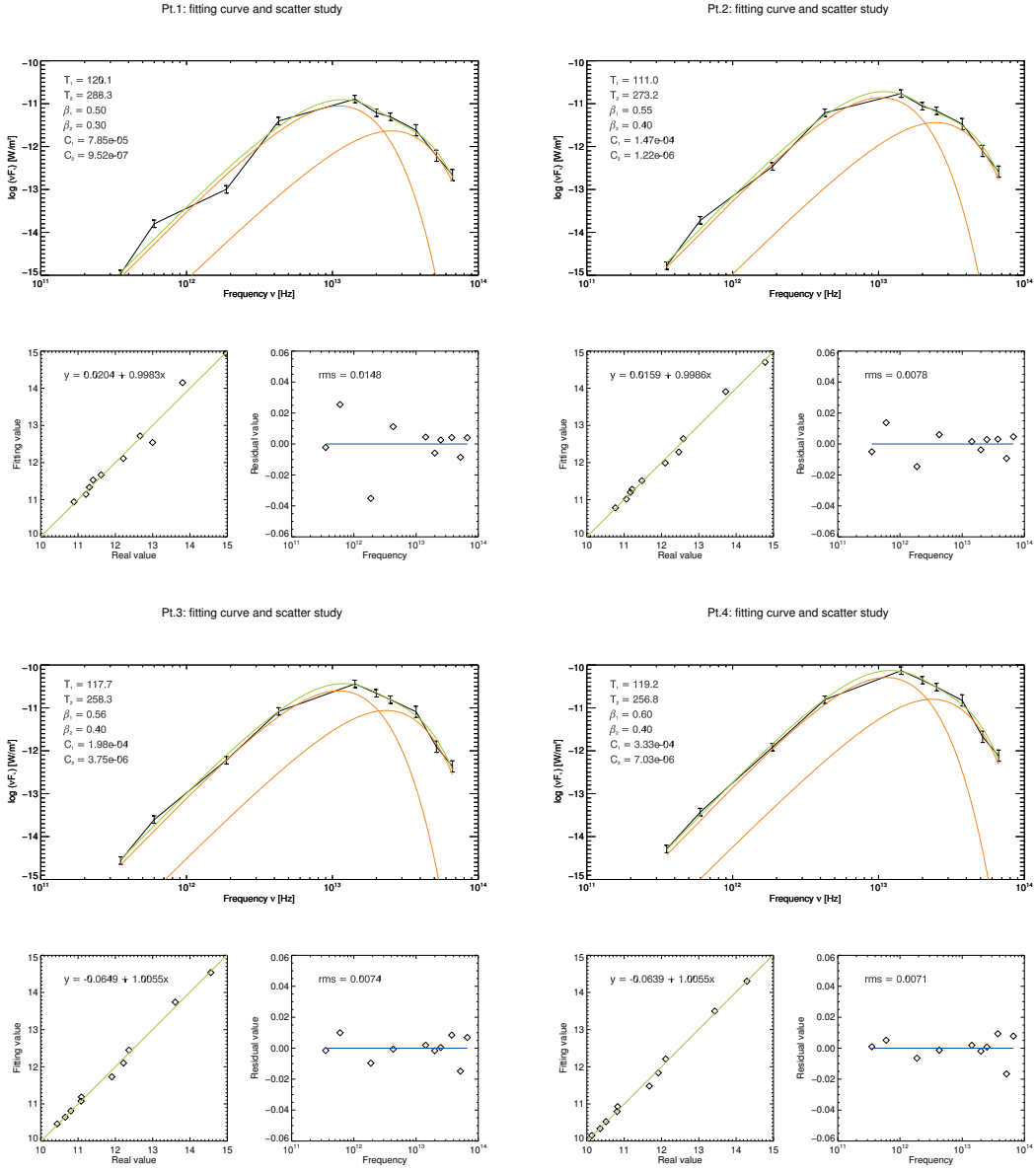

FIGURE 4.7— SEDs of the positions 1, 2, 3 and 4. The fitting results shown for each case (upper plot) are: the general fitting in green, and each component, represented by a gray-body law, in red. For each case, the two measures of quality are also plotted: scatter plot of the measured values versus the fitted values (bottom left), and scatter plot of the residuals versus frequency (bottom right).

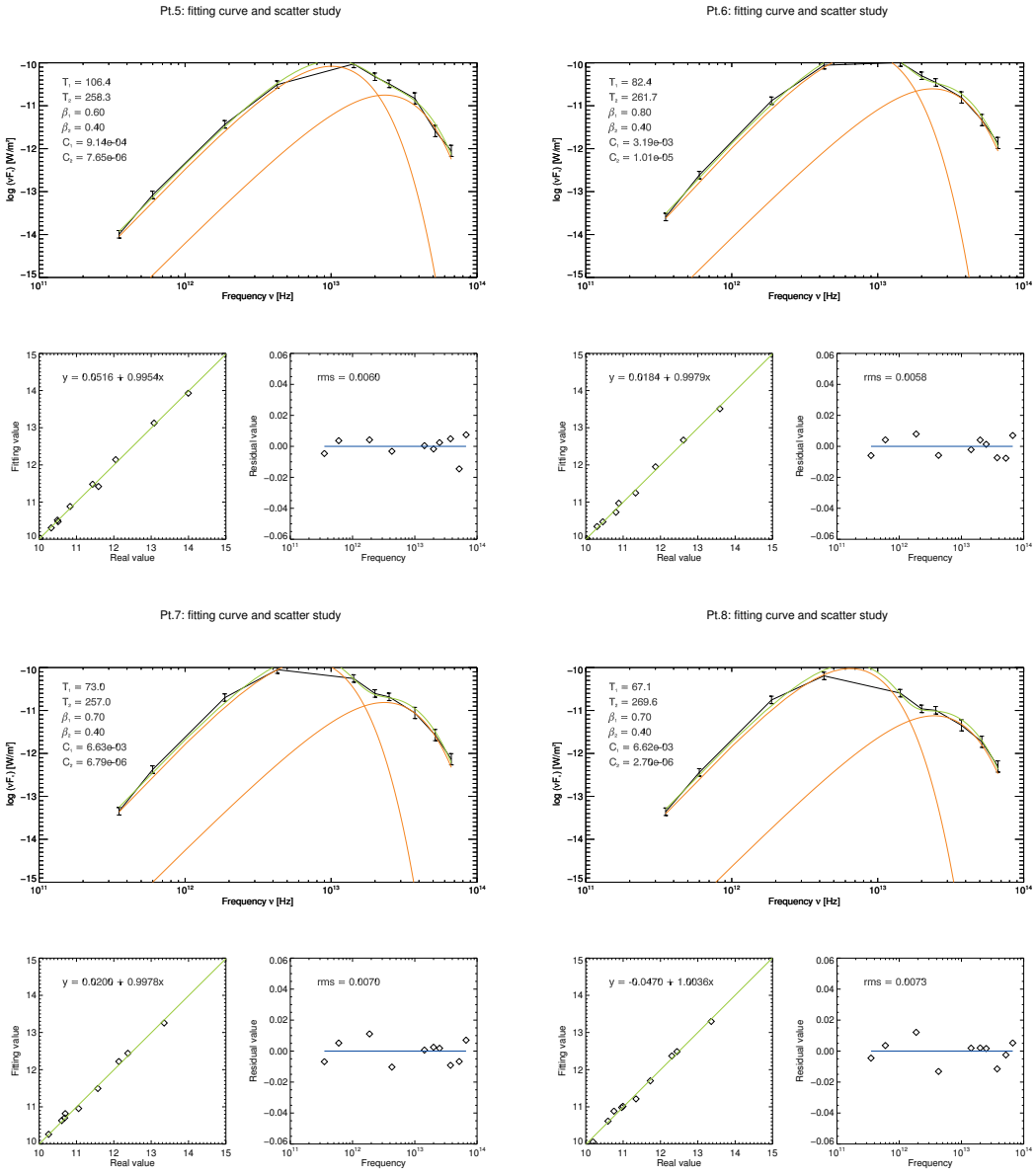

FIGURE 4.8— SEDs of the positions 5, 6, 7 and 8. The fitting results shown in each case (upper plot) are: the general fitting in green, and each component, represented by a gray-body law, in red. For each case, the two measures of quality are also plotted: scatter plot of the measured values versus the fitted values (bottom left), and scatter plot of the residuals versus frequency (bottom right).

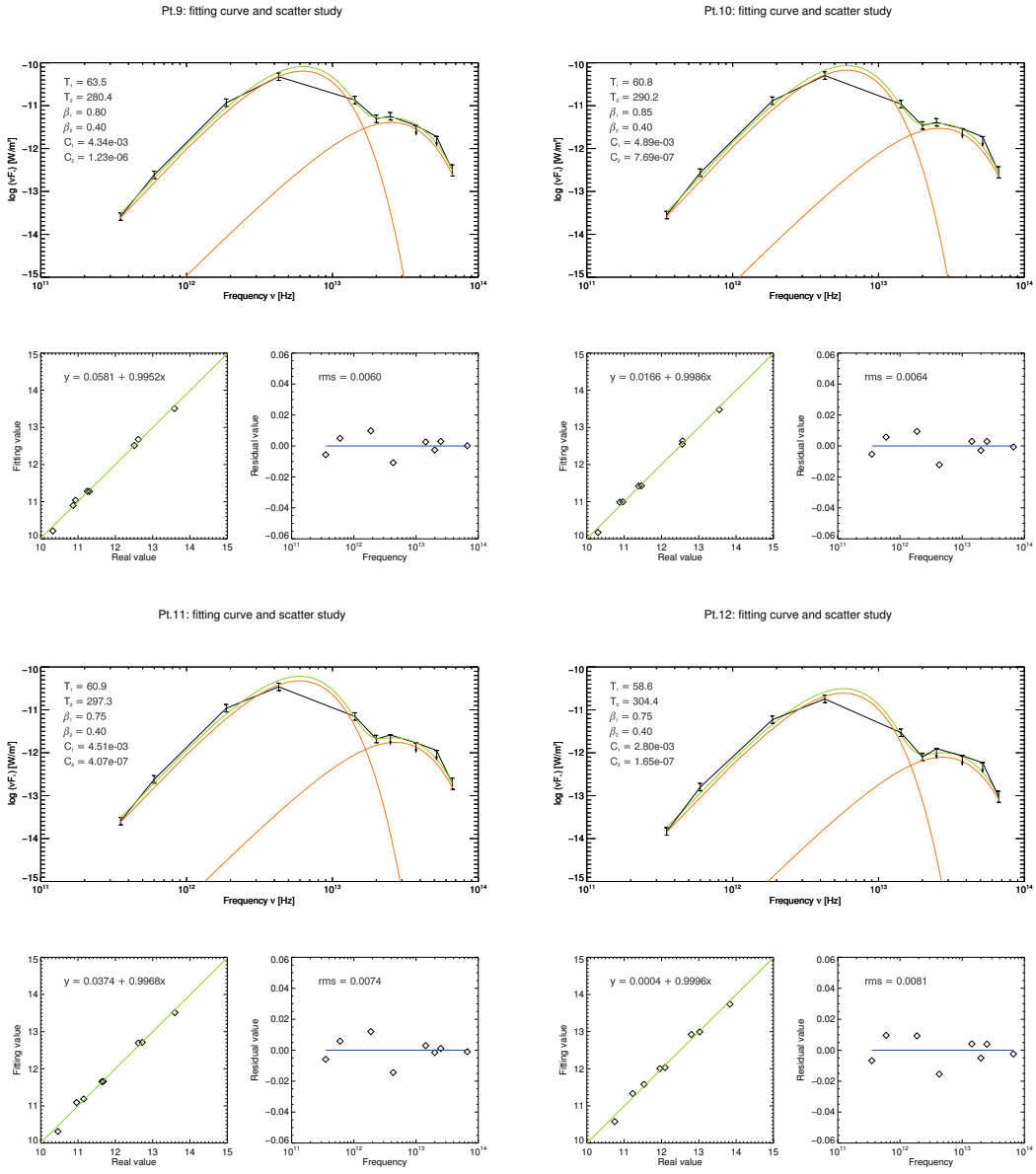

FIGURE 4.9— SEDs of the positions 9, 10, 11 and 12. The fitting results shown in each case (upper plot) are: the general fitting in green, and each component, represented by a gray-body law, in red. For each case, the two measures of quality are also plotted: scatter plot of the measured values versus the fitted values (bottom left), and scatter plot of the residuals versus frequency (bottom right).

components were needed for the first positions because the resulting SEDs are too wide to be fitted with only one component.

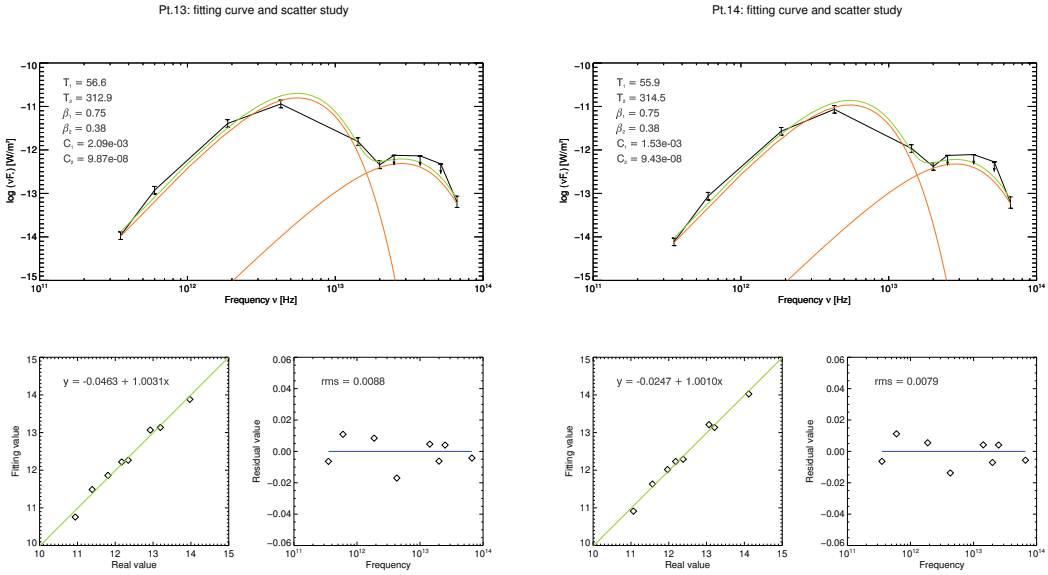

FIGURE 4.10— SEDs of the positions 13 and 14. The fitting results are shown in each case (upper plot): the general fitting in green, and each component, represented by a gray-body law, in red. Also in each case, the two measures of quality are plotted: scatter plot of the measured values versus the fitted values (bottom left), and scatter plot of the residuals versus frequency (bottom right).

Table 4.2 also shows the resulting fitting values for each position and for each component (cold and hot).

4.3.1 Temperature (T) and spectral index (β)

The estimated temperature profiles along the strip (from the H_{II} region to the molecular region) of the hot and cold component are shown in figure 4.11. In figure 4.14 the evolution of the spectral index along the strip and the relation T - β arising from our fittings are also shown.

To understand the variation of the dust temperature, the complex geometry of our source has to be considered (see section 4.1). We have to realize that with our strip of measurements a wide region of M17 SW is covered and almost all the different gas phases along the line-of-sight towards M17 SW are observed (see section

TABLE 4.2— Fitting results for the cold and hot component.

Position	**Cold component** [a]			**Hot component** [a]		
	T_1 $[K]$	β_1	C_1 $(\kappa_0\,\Sigma_1)$ $(\times 10^{-3})$	T_2 $[K]$	β_2	C_2 $(\kappa_0\,\Sigma_2)$ $(\times 10^{-6})$
1	120	0.50	0.079	288	0.30	0.95
2	111	0.55	0.147	273	0.40	1.22
3	117	0.56	0.198	258	0.40	3.75
4	119	0.60	0.333	257	0.40	7.03
5	106	0.60	0.914	258	0.40	7.65
6	82	0.80	3.190	262	0.40	10.10
7	73	0.70	6.634	257	0.40	6.79
8	67	0.70	6.624	270	0.40	2.70
9	63	0.80	4.340	280	0.40	1.23
10	61	0.85	4.893	290	0.40	0.77
11	61	0.75	4.512	297	0.40	0.41
12	59	0.75	2.795	304	0.40	0.17
13	57	0.75	2.092	313	0.38	0.10
14	56	0.75	1.529	314	0.38	0.09

[a] Since these measurements are estimated from our fitting model a $\sim 27\%$ error has to be considered for each one. This error is calculated considering the fitting errors ($\sim 10\%$) and the variance of the resulting parameters ($\sim 25\%$).

4.2.1). In section 4.2.2 we explained that due to the characteristics of M17 SW it is expected to find diverse dust layers with different temperatures and composition. We also described that the model was simplified to two temperature components in each measurement (T_{cold} and T_{hot}) because only nine frequency maps were available.

According to the temperature profile plotted in figure 4.11 and in agreement with the geometry of M17, three parts in our line of measurements (see figures 4.3, 4.4 and 4.5) can be distinguished:

1. *From the position '1' to the positions '2' - '3'.* This region is the closest one to the seven O-stars (heating sources) surrounded by the H_{II} region. The dust temperature is dropping slowly in the two components as we move away from the heating sources. There is no other effect because the PDR is not reached yet. The two components could be described as two layers: The outer one at T_{hot} which is hotter because it is radiatively heated by the UV flux of the heating sources, and the inner one at T_{cold}, which has a lower temperature because the UV flux to which it is exposed is shielded by the outer layer.

2. *From the position '3' - '4' to the positions '8' - '9'.* This is the PDR. Here again the geometry can be treated as two layers of different temperature: The outer one

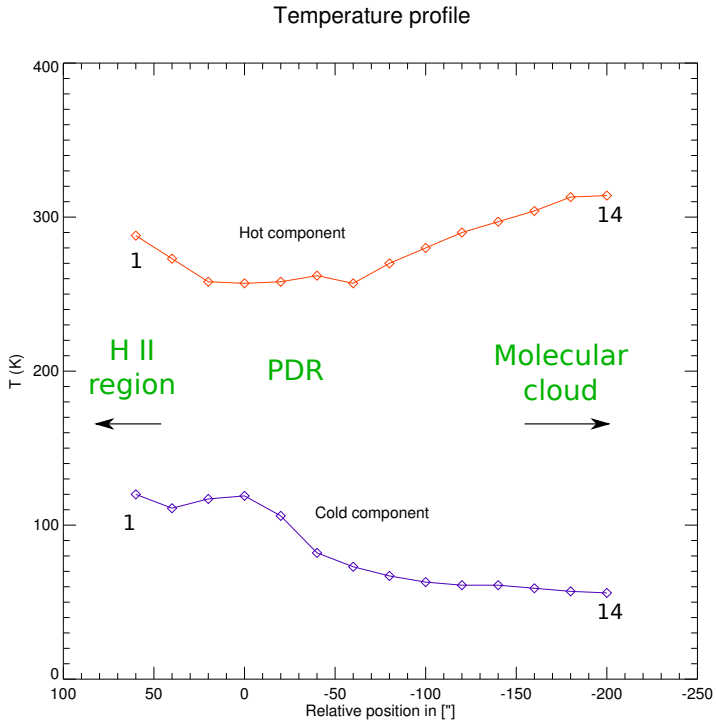

FIGURE 4.11— Temperature profile of the hot and cold component along the strip of measurements.

at T_{hot}, and the inner one at T_{cold}. The cold component increases its temperature because it may be heated in several ways, radiatively due to the high UV flux to which this region is exposed, and, when the density rises, collisionally by the gas, which is heated by the ionization of carbon and by the photodissociation and collisional de-excitation of UV-pumped H_2 (Hollenbach & Tielens 1997). The hot component represents the outer layers, which are still under the influence of the heating sources (i.e., radiatively heated) so that the dust temperature remains constant or even increases slightly.

3. *From the position '9' - '10' to the position '14'.* This is after the PDR. Again two layers can be considered to model the geometry: T_{cold} for the inner layer and T_{hot} for the outer one. Beyond the PDR the UV flux is reduced significantly, molecules start to appear and the medium becomes denser. The cold component does not have any heating mechanism anymore and its temperature decreases progressively, while the hot component behaves in the

opposite way. Although there is no clear explanation for this, one hypothesis could be that this temperature belongs to a faint outer layer of dust which is still heated by the O-stars of the H_{II} region, but since the intensity of the previous mechanisms (points 1 and 2 of this enumeration) were much stronger this layer was hidden, and since now the activity is notably reduced it is visible. One argument which would support this hypothesis is the result shown in figure 4.12, where the peak fluxes of the fitting SEDs are plotted for each component and for each measured position. In the figure it can be noticed that in this region (at the end of the strip) the flux density of the hot component is qualitatively lower than in the central region where the PDR is. Qualitatively, both components exhibit the same behavior regarding the profile of their peak flux densities; as expected, they have the strongest emission within the PDR. Another argument which could help to understand this assumption is the one shown in figure 4.13; in this figure the fitting results from *position 6* and *position 14* are plotted. These two positions were chosen because on one hand, *position 6* is the one with the strongest emission, and on the other hand, *position 14* is the last measured position and the furthest away from the PDR. The figure shows that the dust emission from the PDR is higher than that from the dense and molecular region; in particular, in the emission from the hot component, the difference becomes even larger by roughly two orders of magnitude. Therefore, it can be concluded that this faint layer of dust could be hidden by the strong emission of the PDR.

The resulting structure can also be understood as a combination between the model previously explained and, on a smaller scale, the clumpy PDR model (Stutzki & Guesten 1990). In the model of a clumpy PDR the hot component would represent the inter-clump medium which is hot because of the influence of the heating sources, and the cold component would represent the clumps which are shielded by the inter-clump medium and which are therefore colder.

In figure 4.14 (upper panel) the spectral index profile of the two components along the strip of measurements is shown, and on the lower panel, the T - β relation resulting from our fits is plotted. In general terms, it is true that an inverse relation exists between temperature and spectral index, as it was explained in section 4.2.3. It is notable that the hot component keeps its spectral index roughly constant, but this could be explained with the hyperbolic behavior studied by Dupac et al. (2003), which would make the inverse relation stronger at low temperatures than at higher ones. In fact, the β versus T plot (figure 4.14, lower panel), where the Dupac et al. (2003) hyperbola $\beta = 1/(0.4 + 0.008T)$ is overlaid, suggests that our data may be described by a hyperbola, specifically in the low temperature range. This could be

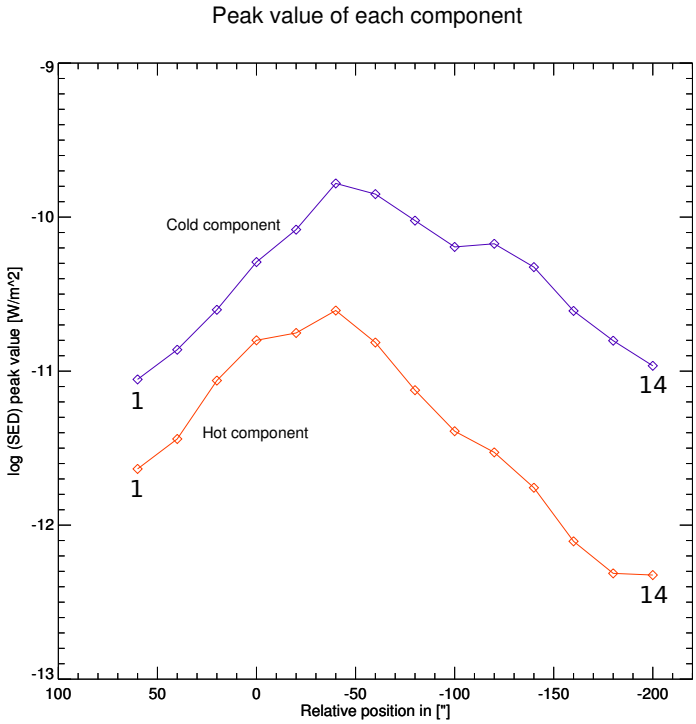

FIGURE 4.12— SED peak values of the cold and hot component at each measured position. The region where the spectral energy is higher corresponds to the PDR.

understandable since, according to Shetty et al. (2009a), least squares fittings of SEDs are very sensitive to noise uncertainties and therefore a relatively large dispersion can exist between these two parameters in this range of temperatures.

4.3.2 Column density (N), opacity (κ) and optical depth (τ)

Until now the temperature and the spectral index have been analyzed. However, the third parameter fitted for each component still has to be examined, namely, C_1 and C_2 (i.e., the optical depths at the reference frequency 345 GHz). As we saw in section 4.2.2, $C_1 = \kappa_0 \cdot \Sigma_1$ and $C_2 = \kappa_0 \cdot \Sigma_2$, where κ_0 is κ_{850} since the frequency of LABOCA was chosen as a reference. If the dust opacity value calculated by Shirley et al. (2011) is taken as a reference for our case ($\kappa_{850} = (1.18 \text{ to } 1.77)^{+0.36}_{-0.24}$ cm^2/g), the column density value can be obtained for each measured position and for each

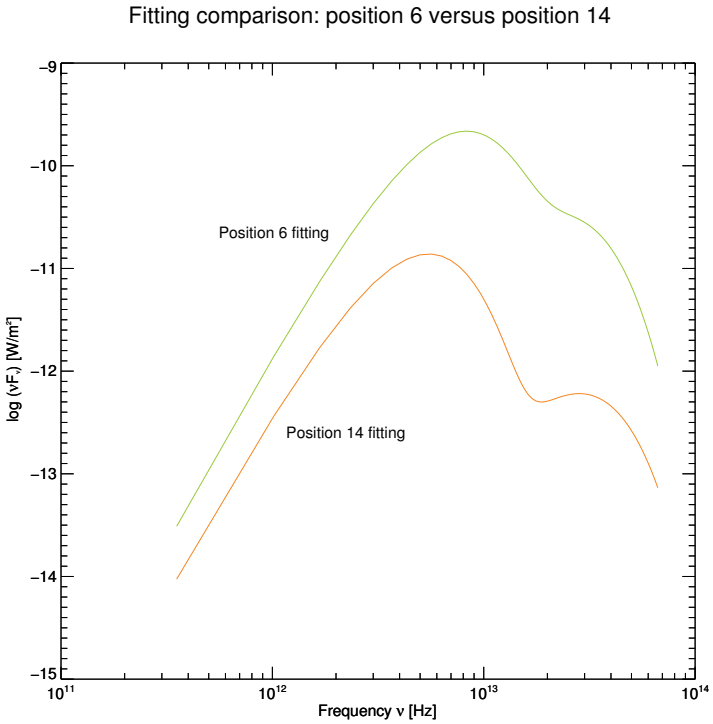

FIGURE 4.13— Comparison between the fitting result of position 6 and position 14. Position 6 corresponds to the PDR and position 14 to the dense and molecular region. It is clear that the "flux density" coming from the PDR is higher than the one emitted by the molecular region.

component. Each component gives the column density of a different dust layer at different temperature and with different dust composition.

Following this method it is assumed that N_{H_2} is calculated from the dust continuum. However, this is not the only method to calculate the N_{H_2}; e.g., it can be calculated using the integrated intensity of the CO 3-2 line as well. Both results may differ because they consider different environments under different assumptions (van Kempen et al. 2009).

It is important to note that the dominant process of H_2 (molecular hydrogen) formation in the Milky Way (and in other galaxies) is through *grain catalysis*. In this process when two hydrogen atoms, bound to the surface of a dust grain, encounter each other, they react to form H_2. The energy released from this reaction is large enough to overcome the forces which were binding the two atoms to the grain, and the H_2 molecule is expelled from the grain surface. A detailed explanation of this process

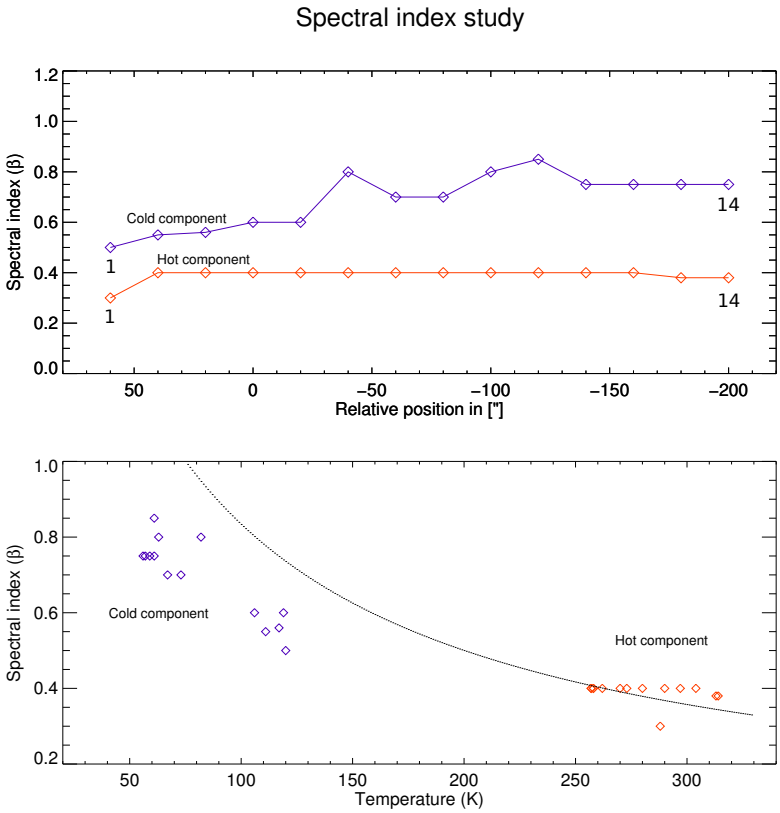

FIGURE 4.14— In the upper plot the spectral index profile of the opacity of the hot and cold component through the strip of measurements is represented. In the lower plot the spectral index versus the temperature is plotted, again for the two components. The dotted line represents the hyperbola of Dupac et al. (2003), $\beta = 1/(0.4+0.008T)$, which according to their study is the best fit for the T - β relation.

can be found in Hollenbach & Salpeter (1971) and in Draine (2011). Therefore, to use the column density of the molecular hydrogen as a dust column density "tracer" is actually a reasonable approximation in our case[5].

Since the column density calculated is per molecule of hydrogen (gas) it makes more sense to refer the dust opacity not to the dust mass but to the gas mass. If we assume the "canonical" value for the dust to gas mass ratio of 1 : 100 ([6]), the aforesaid

[5]Normally, in molecular clouds where the dust population is high almost all the hydrogen is in its molecular form, and therefore, the column density obtained from the dust is directly related to N_{H_2}.

[6]This ratio is a general approximation and can vary according to the environment, therefore some

opacity value of $\kappa_{850\ dust} = 1.32\ \mathrm{cm}^2/\mathrm{g}$ has to be divided by a factor 100 to calculate a reliable N_{H_2} (Ossenkopf & Henning 1994, Shirley et al. 2000 and van Kempen et al. 2009). This also means that the total mass (gas and dust) equals the gas mass within the uncertainty of this analysis.

In figure 4.15 the column density (N_{H_2}) profile along the strip (upper plot) and the relation column density versus temperature (lower plot) is shown. The column density of the cold component always remains higher than the column density of the hot component, this would be explained because in general cold temperatures involves less activity and denser environments than higher temperatures; this explanation would agree with the T - N_{H_2} plot as well. Also, the column density profile plot would agree with the previous description (section 4.3.1), in which, on one hand, the cold component becomes colder as we move away from the PDR (entering the molecular cloud) and therefore its column density increases, and on the other hand, the hot component becomes hotter following the same direction and consequently its column density decreases.

On the other hand, if κ_{850} is fixed to the Shirley et al. (2011) value and using the spectral index (β) resulting from our fittings, the value of the frequency-dependent opacity, κ_ν, can be obtained for each measured position and each component. As we already know from section 4.2.2, κ_ν can be calculated as: $\kappa_\nu = \kappa_0 \left(\frac{\nu}{\nu_0}\right)^\beta$. Again, the different dust temperatures and composition make this result specific for each component. In figures 4.16 and 4.17 the dust opacities along the strip of measurements are plotted, each figure for each component. In this case the κ_{850} used for the calculation is directly the "Shirley" value ($\kappa_{850\ dust}$) because the dust opacity is the goal of this calculation. The dust opacity at each frequency is shown in the figures. It can be seen that the opacity increases with the frequency.

Once the frequency-dependent opacity is known, the optical depth for each frequency, τ_ν, can be calculated for each measured position and for each component, following the formula used by e.g., Kauffmann et al. (2008):

$$\tau_\nu = N_{\mathrm{H}_2} \cdot \mu_{\mathrm{H}_2} m_{\mathrm{H}} \kappa_\nu \tag{4.5}$$

where μ_{H_2} is the molecular weight per hydrogen molecule[7] and m_{H} is the H-atom mass. The κ_ν value used is the dust opacity related to the gas mass so as to calculate

uncertainties have to be considered when this conversion is used.

[7]The molecular weight depends on the gas phase which is ionized, atomic or molecular. Since we ignore the exact distribution of these phases across the PDR, we approximately use the value of μ_{H_2} for the molecular phase. Therefore, the calculated τ_ν can be ultimately considered as an upper limit.

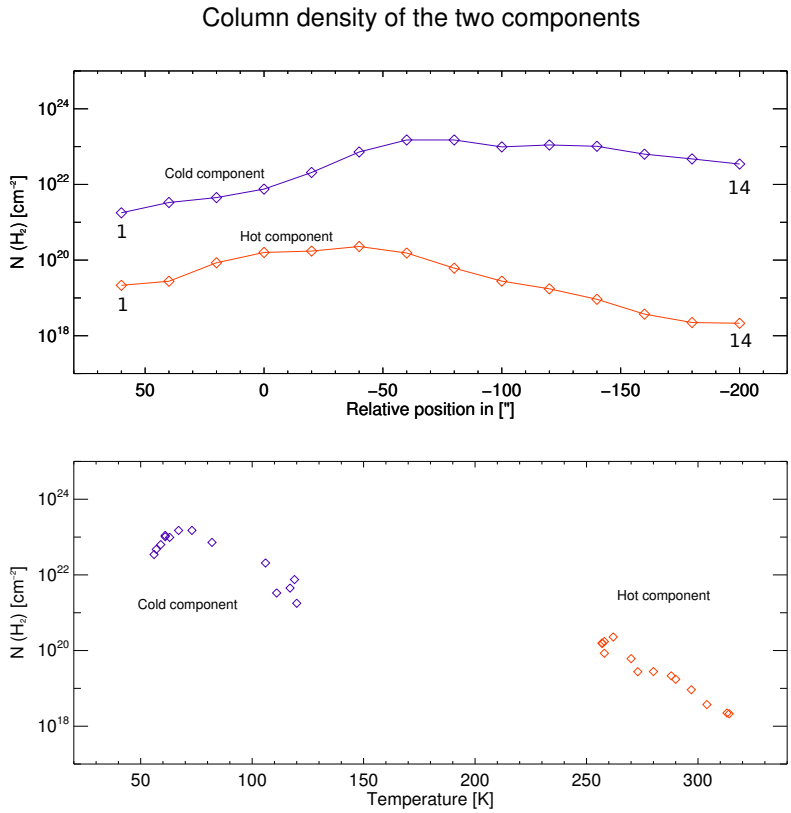

FIGURE 4.15— Column density of each component along the strip of measurements. The cold component becomes denser during and after the PDR whereas the hot component is getting more diffuse following the same direction .

the optical depth τ_ν from a gas column density. Therefore, the opacities applied here were the dust opacities obtained previously divided by 100 (Ossenkopf & Henning 1994, Shirley et al. 2000 and van Kempen et al. 2009).

In figures 4.18 and 4.19 the optical depth along the strip is shown for each frequency, for the cold and the hot component, respectively. The hot component remains always in an optically thin regime, since $\tau_{\nu\ HOT} \ll 1$ for all frequencies and in all positions. However, for the cold component in the last part of the PDR (reaching the molecular region), the optically thin condition, $\tau_{\nu\ COLD} \ll 1$, does not hold for the higher frequencies, and these wavelengths should be considered optically thick in this region. Nevertheless, the contribution of the cold component to the flux density at

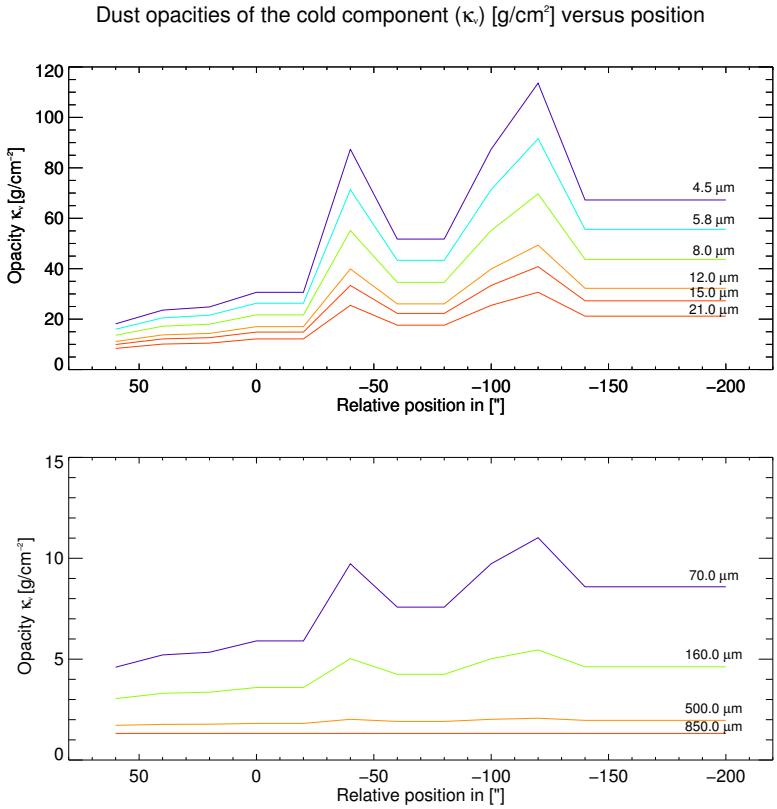

FIGURE 4.16— Dust opacities of the cold component. In the upper panel the opacities corresponding to the wavelengths 4.5 µm, 5.8 µm, 8.0 µm, 12.0 µm, 15.0 µm and 21.0 µm are shown . In the lower one opacities of the wavelengths 70 µm, 160 µm and 500 µm and 850 µm, are represented. On one hand, the opacity profile along the strip follows the shape of the spectral index since the opacity is spectral index dependent (see figure 4.14). And on the other hand, the opacity increases clearly with the frequency.

these frequencies is very low (less than 10% for the four shortest wavelengths) and could be ignored.

4.3.3 Mass profile

Another parameter that can be calculated is the mass (dust or dust + gas) for each measured position. In order to simplify the calculation the two components (hot and

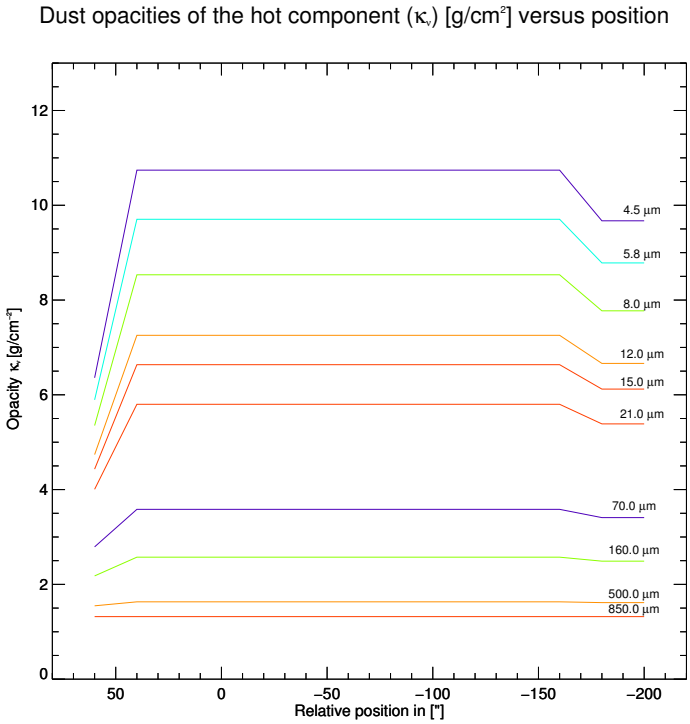

FIGURE 4.17— Opacities of the hot component at all used wavelengths. A conclusion similar to that drawn from the previous figure could be found (figure 4.16).

cold) are considered independently, which means that there is no contribution in the cold component coming from the hot component and vice-versa. In this way the gas mass can be estimated with the formula:

$$M = \Omega \Sigma D^2 \tag{4.6}$$

where D is the distance to the source, and Ω is the solid angle subtended by the resolution of $19''$ and Σ is again the gas mass column density derived from the fits. For the distance of our source the value of 1.98 kpc reported by Xu et al. (2011) was adopted.

According to figures 4.18 and 4.19, the optically thin regime, which is the prerequisite for using the gray-body laws of this analysis, can be assumed in most cases. The only case where τ_ν becomes larger and the optically thin assumption does not hold anymore is for the cold component at the high frequencies (short

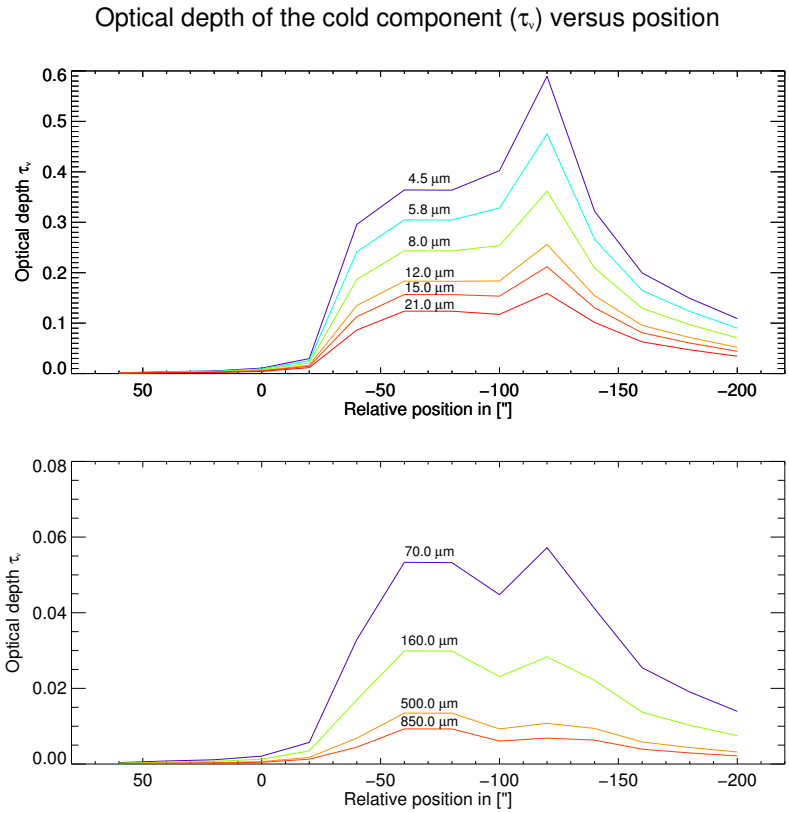

FIGURE 4.18— Optical depth of the cold component along the strip. During the last part of the PDR and reaching the molecular region, the optically thin condition, $\tau_{\nu\ COLD} \ll 1$, can not be applied for the higher frequencies, and therefore, the component becomes optically thick for these wavelengths.

wavelengths). However, as it was discussed in the previous paragraph, the contribution of the cold component to the flux densities at short wavelengths is very small (at least a factor 10 smaller) and can be ignored for our approximation.

Figure 4.20 shows the mass profile for each component, which is a scaled version of the column density profile (figure 4.15) because on each position of the strip the mass refers to the same solid angle, namely, Ω. Therefore, the same conclusion drawn from the column density profile can be applied here, i.e., that in general the cold component is denser than the hot one and therefore more massive.

On one hand, the cold component increases its mass rapidly crossing the PDR, where the dissociation of particles is taking place and where it is approaching the

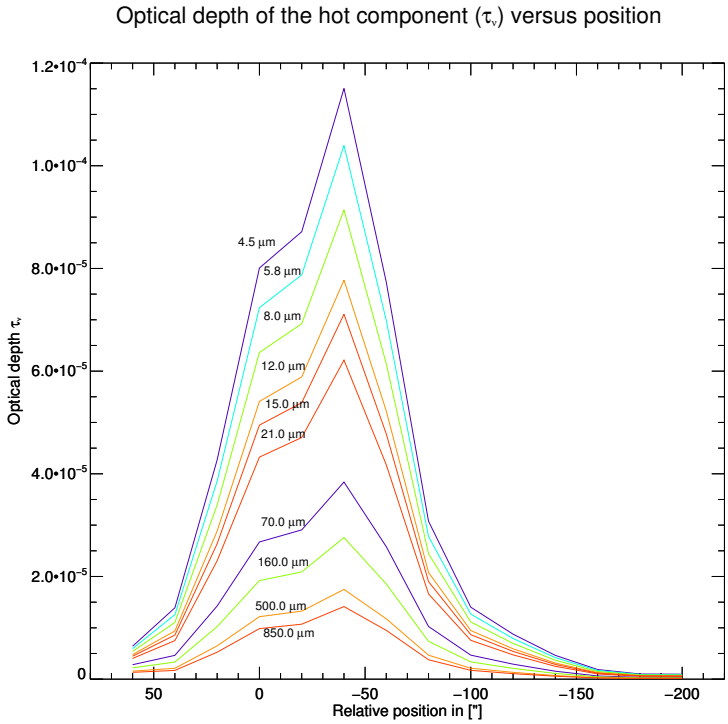

FIGURE 4.19— Optical depth of the hot component along the strip. The hot component remains in optically thin regime all along the strip and in all frequencies: $\tau_{\nu\ HOT} \ll 1$.

molecular cloud. Thereafter, in the molecular region, the dust mass decreases smoothly, i.e. the molecular cloud is getting more diffuse away from the region. On the other hand, the hot component behaves in a similar way as the cold one: Its mass increases while it is crossing the PDR and reaching the molecular region. However, once the molecular cloud is reached its value drops significantly; this would agree with the hypothesis explained in section 4.3.1, where after the PDR the hot component would represent a very diffuse and faint dust layer which is surrounding the whole region studied here.

4.3.4 UV flux and visual extinction

Hollenbach et al. (1991) proposed one-dimensional models of PDRs defined as mainly neutral regions where far-ultraviolet (FUV) radiation dominates the heating process.

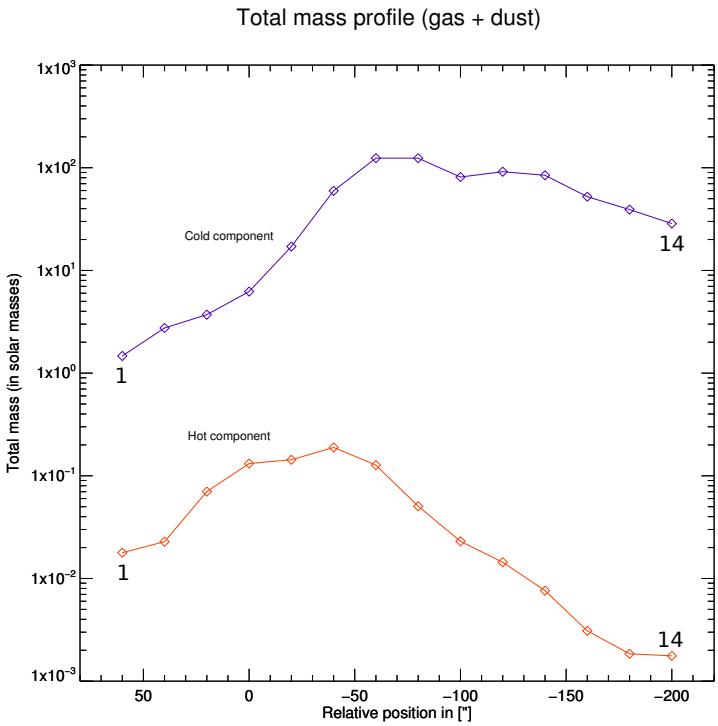

FIGURE 4.20— Mass profile of the two components along the strip. The mass of the cold component increases along the PDR and decreases slightly in the molecular region. The mass of the hot component behaves in a similar way along the PDR but decreases rapidly in the molecular region.

From these models they could estimate the amount of FUV flux which heats the PDR using the temperature, the visual extinction and the optical depth of the region. They showed some approximations of the general formula which are valid under some assumptions and thus the general model could be simplified. For our calculation it is assumed that the equilibrium dust temperature is roughly the same as the dust temperature achieved from our fitting. Hence, the following formula derived by Hollenbach et al. (1991) can be used:

$$T_{dust} \approx T_0 = 12.2\, G_0^{0.2}\ [K] \tag{4.7}$$

where G_0 is the FUV flux measured in units of the equivalent Habing flux (1.6×10^{-3}erg cm^{-2} s^{-1}, which is the flux calculated by Habing (1968) for the local ambient interstellar radiation flux).

According to Hollenbach et al. (1991) this formula was derived for temperatures between $10-150$ K, therefore it may not be suitable for our hot component (temperatures >250 K). A method to confirm the FUV results for the hot component would be to calculate the UV flux emitted by the exciting sources (O and OB stars) and then to calculate the absorption that the FUV radiation undergoes between the source and the measurement point. The first part can be easily computed integrating over the UV range of the Planck function of these stars ($T \sim 30000-20000$ K). This gives us a $G_0 \sim 10^{15}$ at the stellar surface. However, several studies regarding the absorption by the intermediate medium (e.g. Hollenbach & Tielens 1997 and Boisse 1990) reveal that this calculation is not straightforward. Several parameters which are beyond the goal of the current study are needed, e.g., clumpiness, filling factor and photon scattering according to the complex M17 SW structure. Therefore, due to the complexity of this calculation, it will considered as future work. For our study, the FUV values obtained from the hot component will be considered only as a reference for comparison and will have to be confirmed.

In figure 4.21 the FUV flux (G_0) is shown.

As it can be expected, the hot component is more exposed to the far-ultraviolet flux than the cold one, and they present different behaviors:

1. The FUV in the cold component is decreasing progressively as we move along the strip (from the H_{II} region to the molecular region). The FUV flux emerges from the O-stars at the center of the region (see section 4.1) and since it causes the photodissociation process, it is being absorbed as it crosses the PDR.

2. On the contrary, the FUV in the hot component maintains a roughly constant value, this is because this component refers to a diffuse dust layer with lower density (see section 4.3.2), and therefore the absorption is low. Even where we can start to measure the outer and very diffuse dust layer at the end of our strip (see section 4.3.1) the FUV is slightly increased because the absorption is even lower.

Another parameter that can be calculated is the visual extinction A_V. According to Kauffmann et al. (2008), and based on Bohlin et al. (1977), the relation between the visual extinction (A_V) and the column density per hydrogen molecule (N_{H_2}) is:

$$N_{H_2} = 9.4 \times 10^{20} \cdot A_V \text{ cm}^{-2} \tag{4.8}$$

This equation is valid for dusty environments in molecular clouds where mainly all the hydrogen is in its molecular form; consequently, it may not be completely true for the firsts positions of our strip of measurements. This formula comes from the original formula from Bohlin et al. (1977):

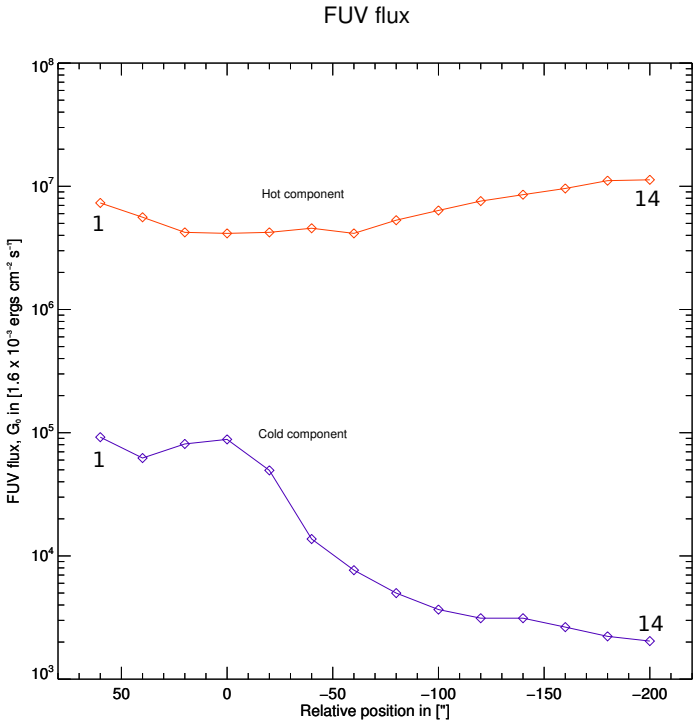

FIGURE 4.21— Far-ultraviolet (FUV) flux of the two components along the strip of measurements, relative to the Habing flux. Since the hot component represents a more diffuse layer than the cold one, FUV remains longer

$$N_{total\ \mathrm{H}} \simeq 1.9 \times 10^{21} \cdot A_V\ \mathrm{cm}^{-2} \tag{4.9}$$

where

$$N_{total\ \mathrm{H}} = N_{\mathrm{H_I}} + 2N_{\mathrm{H_2}} \tag{4.10}$$

and considering that $N_{\mathrm{H_2}} \gg N_{\mathrm{H_I}}$.

Since we do not know where the exact transition between atomic and molecular hydrogen is located in the PDR, we approximate our scenario by a dusty molecular cloud (equation 4.8). Therefore, the A_V obtained would indicate an upper limit (at least in the firsts positions of our strip).

In figure 4.22 the visual extinction of the two components is shown. Since it is a parameter dependent on column density the results achieved can be understood with

the same arguments as before. The visual extinction is directly related to the mass and the column density, which means that the positions where the column density is higher contain more mass and therefore present higher visual extinction. The different results obtained from the cold and hot component can be interpreted as follows: The cold component shows more extinction than the hot one since the cold component is denser and more massive than the hot component.

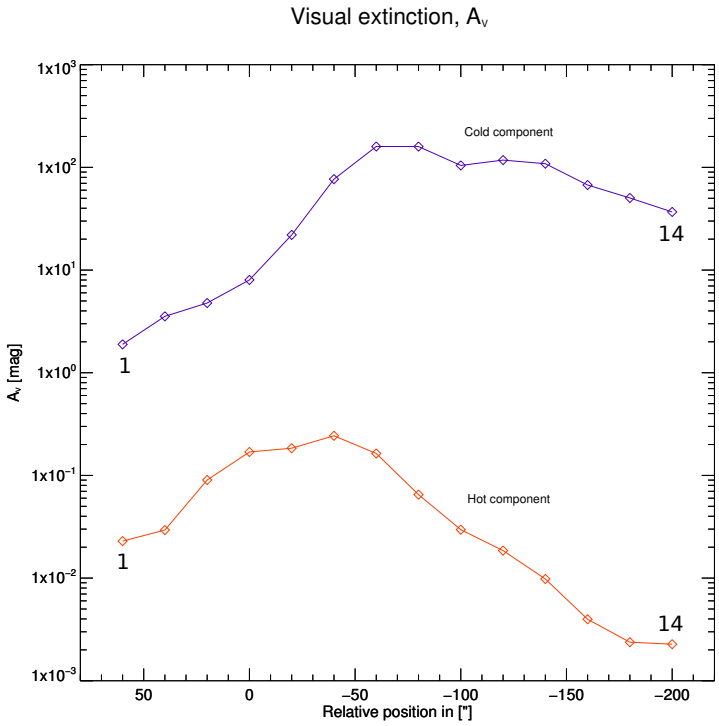

FIGURE 4.22— Visual extinction of each component along the strip of measurements. Since the visual extinction is directly related to the column density, higher column densities imply a higher visual extinction.

4.3.5 Summary of the calculations

Tables 4.3 and 4.4 summarize the study of the cold and hot component, respectively, done in this section. In these tables a characteristic sample of the measurements accomplished in this section is shown. We present the parameters computed for three positions of our strip of 14 measurements (1, 6 and 14, see images 4.3, 4.4 and 4.5).

With these three positions we have a sample of each of the three parts distinguished in our region: next to the H_{II} and before the PDR, within the PDR, and in the "molecular region" after the PDR (see above in this section).

TABLE 4.3— Cold component results for three positions of our strip.

Point	T_{dust} (K)	N_{H_2} $(10^{22} \cdot cm^{-2})$	M_{total} [a] $(M_\odot)$	$\tau_{70\mu m}$ (10^{-2})	A_V (mag)	FUV $(G_0 \times 10^4)$
1	120	0.178	1.47	0.04	1.89	9.21
6	82	15.015	124.15	5.33	159.73	0.77
14	56	3.461	28.62	1.39	36.82	0.20

[a] To calculate dust mass: $M_{dust} \approx M_{total}/100$

[b] Since these measurements are estimated from our fitting model a $\sim 27\%$ error has to be considered for each one. This error is calculated considering the fitting errors ($\sim 10\%$) and the variance of the resulting parameters ($\sim 25\%$).

TABLE 4.4— Hot component results for three positions of our strip.

Point	T_{dust} (K)	N_{H_2} $(10^{20} \cdot cm^{-2})$	M_{total} [a] $(M_\odot)$	$\tau_{12\mu m}$ (10^{-6})	A_V (mag)	FUV $(G_0 \times 10^6)$
1	288	0.216	0.018	4.78	0.023	7.33
6	262	1.537	0.127	52.25	0.163	4.15
14	314	0.021	0.002	0.67	0.002	11.29

[a] To calculate dust mass: $M_{dust} \approx M_{total}/100$

[b] Since these measurements are estimated from our fitting model a $\sim 27\%$ error has to be considered for each one. This error is calculated considering the fitting errors ($\sim 10\%$) and the variance of the resulting parameters ($\sim 25\%$).

4.4 Summary and conclusions

In the present study the dust component of M17 SW has been analyzed. 10 different maps at different frequencies and a strip of 14 measurements crossing the region were used for this purpose. The maps covered the frequency range from the near infrared to the millimeter/submillimeter, where the dust emission is present. The analysis was performed along a strip across the PDR, positions were equidistant every $20''$ in right ascension at constant declination and measurements were done through the same aperture size ($20''$ of diameter).

According to the number of frequencies used in our analysis, and to the shape of the dust SEDs, we modeled the region with two components, a hot component and a cold one. In each position, the least-squares method was applied in order

to fit a function consisting of two gray-body (i.e., modified blackbody) laws, each representing one of the two dust components.

From the aforesaid fittings the dust temperature (T_{dust}), the spectral index (β) and the column density were determined for each measured position.

Furthermore, from the obtained parameters and with some relations found in the literature (see section 4.3) other parameters of interest were computed: the column density (N_{H_2}), the optical depth (τ_V), the mass (dust or total mass), the visual extinction (A_V) and the far ultraviolet flux (FUV, G_0). These other calculations helped us to understand the geometry of the region.

From our study, the following conclusions could be drawn:

1. Three regions with different characteristics were distinguished along the strip of measurements:

   - Phase 1: Towards the H_{II} region and in front of the PDR.
   - Phase 2: Towards the PDR.
   - Phase 3: In the "molecular cloud" behind the PDR.

   A detailed explanation of this structure can be found in the previous section (section 4.3). The assumed geometry also agrees with the common PDR structure (Tielens & Hollenbach 1985 and Hollenbach & Tielens 1997).

2. Each component (cold and hot) behaved in a different way throughout the three phases. A summary of the findings is presented here:

   - *"Cold" component*: The temperature decreases slightly until the PDR is reached ($T \approx 110$ K). In this small phase the cold component may be related to the dust in some diffuse and external layers since little dust is expected to be found in the immediate vicinity of the H_{II} region and before the PDR. The low mass and consequently the low visual extinction agrees with this argument ($A_V \approx 2$, $N_{H_2} \approx 10^{21}$ cm^{-2}).

     Across the PDR the temperature rises to $T_{max} \approx 120$ K due to the combination of two factors: On one hand, where the PDR is directly adjacent to the H_{II} region, the FUV flux from the latter is heating the dust. On the other hand, we are moving to denser and more massive regions ($N_{H_2 max} \approx 10^{23}$cm^{-2}), and therefore the dust may also be heated by collisions with the gas (which in turn is heated by the photodissociation of molecular hydrogen and photoionization of carbon), while the FUV flux ($10^4 < G_0 < 10^5$) is reduced because it is being absorbed when it crosses the PDR.

Finally, behind the PDR, the temperature drops ($T \approx 50$ K) because the FUV flux coming from the heating sources has been absorbed significantly ($G_0 < 5 \cdot 10^3$). We are in a molecular cloud and the medium develops into a denser and more massive region; only at the end of the strip the mass starts to decrease slightly, which means that the molecular cloud is becoming more diffuse ($N_{\mathrm{H}_2} \approx 10^{22}$ cm^{-2}).

Despite the decrease of the temperature at the beginning of the strip, it can be concluded that this component clearly behaves as expected from a PDR.

Also, this component could be understood under the frame of a clumpy PDR model (Stutzki & Guesten 1990), or at least, under a combination between the model explained and the clumpy PDR model. In that scenario the cold component would represent partly the cold clumps surrounded by a hot inter-clump medium (see next point). To figure out that scenario a better angular resolution would be needed in order to resolve some of the clumps. With the new A-MKID camera the resolution of the HFA will be around $8''$ and hopefully this issue can be clarified in the near future.

- *"Hot" component*: This component represents more external dust layers. In general terms these layers are less dense and less massive than those associated with the cold component.

  At the beginning, the temperature slightly decreases as it happens in the cold component ($280 < T < 260$ K). The process here can be understood in a similar way as for the cold component. The only difference is that the layers associated with the hot component are less dense, and consequently more diffuse ($N_{\mathrm{H}_2} \approx 10^{19}$ cm^{-2}). In these layers the FUV flux is stronger and therefore they are hotter ($G_0 \approx 10^6$). These layers probably are more external than those represented by the cold component ($A_V \approx 0.02$).

  Along the PDR, the temperature maintains a roughly constant value ($T \approx$ 260). Since it is a diffuse region the photodissociation process is low and the FUV flux can penetrate further into the cold component (still $G_0 \approx 10^6$, $A_V \approx 0.2$) and, consequently, maintain the grain heating. On the other hand, the activity in the inner regions also influences this component, slightly warming the dust grains. It is in this phase where dust emission is higher.

  After the PDR, in the molecular region an interesting effect has been found. The medium becomes less dense and less massive and hence the visual extinction is reduced significantly ($A_V < 0.05$). However, the temperature and the FUV flux keep their value constant or even increase slightly ($T \approx$ 300 K , $G_{0\ \mathrm{max}} \approx 10^7$). As hypothesis for this behavior it was suggested that these temperatures are associated with even more outer, diffuse and

consequently very faint layers. Due to their low visual extinction, the FUV flux could penetrate through them, but because of their faintness, they were hidden by the strong emission of the PDR; and since the emission from the cold gas and dust is notably reduced there they can be detected.

Following the clumpy PDR model introduced in the previous point, this component could also be understood as a combination between the model explained just above and the clumpy PDR model. In that scenario the hot component would partly represent the hot inter-clump medium containing the clumps. As it was mentioned before, better angular resolution is needed to really confirm this scenario.

If we want to deeply understand the chemistry taking place inside PDRs, a broader study than the work at hand will be needed.

3. An optically thin regime could be assumed across the relevant frequency range ($\tau_{\nu\ COLD} \ll 1$ and $\tau_{\nu\ HOT} \ll 1$). The only case where τ_ν increased, and where the optically thin assumption may not hold anymore, is for the cold component at high frequencies (low wavelengths). However, since the contribution of the these frequencies to the cold component was very low, it could be ignored in our model.

4. An inverse relation between Temperature (T) and spectral index (β) has been found. Some studies regarding this aspect were done by Dupac et al. (2002) and Dupac et al. (2003) and by Shetty et al. (2009a) and Shetty et al. (2009b). The reason for this behavior is not yet well established. On one hand, Dupac's studies relate this inverse relation to an intrinsic dependency of the spectral index on the dust temperature, and on the other hand, Shetty's investigations affirm that this anticorrelation is due to the noise in the flux measurement. They assert that least-square fits to fluxes in the R-J regime ($h\nu \ll kT$, small frequencies) are very sensitive to observational uncertainties, such as noise, and this may produce a spurious inverse $T - \beta$ relationship.

   Further investigations are needed to really determine the cause of this behavior but with our study the inverse relation, could be reaffirmed at smaller spatial scales (higher resolution).

4.5 Further work

In order to improve our study M17 SW must be further analyzed. For this purpose, more observations will be needed since in the present study all the aspects discussed were extracted only from the dust continuum flux.

1. As we discussed in the section 4.3.2, N_{H_2} could also be calculated by integrating the flux over the CO $3-2$ line and by applying the relation between H_2 and CO abundances by Wilson & Rood (1994) (van Kempen et al. 2009). Since different conditions are assumed in each case the results will be different. On one hand, CO can be frozen out onto the dust grains at low temperatures and in sufficiently high density environments, this would decrease the deduced H_2 column density. On the other hand, the computation of N_{H_2} from the dust continuum assumes that all the dust emission is an isothermal envelope which is not completely true since some inner structures can contribute to the continuum emission (van Kempen et al. 2009). To compare both column densities would help to better understand the morphology of the region.

2. It would be convenient to estimate the column density of atomic hydrogen (N_H) with a method independent of the dust continuum, in order to compare it with the molecular hydrogen column density (N_{H_2}). This would help us to better analyze the photodissociation front of the PDR because the H to H_2 transition could be roughly located (Hollenbach & Tielens 1997). The N_H could be derived e.g., from the "21 cm line" emission maps. Following this purpose, another important transition which takes place in PDRs and could be studied is the C^+ to CO transition .

3. It is expected to find intense emission from the fine structure lines in the PDR: [C II] at 158 μm, [O I] at 63 μm and 146 μm, and [C I] at 370 μm (also others but less intense ones); these lines dominate the cooling of the atomic gas. Emission from the molecular transition CO $1-0$ and significant H_2 rovibrational emission arising from the UV pumping mechanism could be also detected (Tielens & Hollenbach 1985, Hollenbach et al. 1991 and Hollenbach & Tielens 1997). The study of all these lines would help to better analyze and understand the chemistry and the energy balance inside the PDR.

4. The next A-MKID commissioning phase is expected for October 2014. If the period is favorable we expect to observe M17 SW with both detectors (LFA at 850 μm and HFA at 350 μm). This will allow us to improve our study in mainly two aspects. First, we will be able to compare the LFA map with that of LABOCA and extract some conclusions about the performance of the new camera, and also about the observing time saved. And second, we will be able to add to our analysis another map with a new frequency (HFA at 350 μm) and with higher angular resolution ($\sim 8''$). This better angular resolution may provide us with some information about the clumpy PDR model in the region.

Here we have presented some aspects that could be added to our analysis in the near future, this list is of course not exhaustive.

5

Final summary

In order to recapitulate the work done during this thesis I summarize here the main points.

An optical system for the A-MKID camera has been developed and tested during the first commissioning of the camera which was accomplished in December 2013. The system has been designed to optimize the MKIDs response, as well as to minimize the number of optical elements used, in order to make the camera as compact as possible.

With the A-MKID optical design the following has been achieved:

1. A purely reflective system in order to achieve the best dual frequency response. The use of lenses implies the use of anti-reflection coatings, and it is almost impossible to optimize a coating for two frequencies at the same time.

2. A completely diffraction-limited system for the two working frequencies of the camera (LFA: 345GHz and HFA: 850GHz) with a FoV of $>$15 x 15 arcmin^2 .

3. An average distortion of $\sim$ 13% in the complete FoV.

4. Pixel spacing around 1 $F\lambda$, which is a good compromise between throughput, mapping speed and the resources given.

5. An angular resolution of $\sim 18.3''$ (FWHM of the main beam).

Some beam maps were computed from fully sampled maps on several planets (Mars, Uranus and Jupiter) in order to characterize the receiver beam. Some aberration has been detected in some parts of the array, concluding that some misalignments were introduced during the installation of the optics. This means that a better alignment

is required for the next run. Due to this aberration the resulting main beam had an ellipticity of $\sim 11\%$.

Due to transport damages of the cryogenic isolating structures, no observations could be performed with the HFA (High Frequency Array). Observations of a Galactic target, the nebula NGC3603, were performed with the LFA (Low Frequency Array) of the new camera. The best value sensitivity obtained in a map of this source was ~ 80 mJy/beam (RMS), which is roughly three times worse than the RMS obtained in a map of the same source with LABOCA (same frequency) and with approximately the same integration time. We conclude that a better characterization of our detectors and read-out system is required to increase the sensitivity. However, no strange artifacts were detected in these observations and no major issues were reported.

In order to demonstrate the high scientific potential of continuum observations at these wavelengths, a study of the dust component of the well known nebula M17 SW has been carried out. Although no data of the new camera could be included in this study (they will be included in further publications), interesting results have been achieved with the available data of this source in the sub-millimeter and infrared wavelength range.

Using maps at different frequencies spectral energy distributions (SEDs) for a specific aperture size were calculated along a strip of measurements. This allowed us to cover the complete region in order to characterize the different gas phases existing in a volume reaching from the H_{II} region to the molecular cloud, including the photodisociation front contained in between. The SEDs were well fitted using a combined function of two gray-body laws, representing a cold and a hot component.

From these fits the dust temperature (T_{dust}), the spectral index (β) and the column density (N_{H_2}) were obtained for each measured position.

Also, from these parameters and with some relations found in the literature, additional important parameters were computed (e.g. mass, optical depth or visual extinction), which helped us to understand the geometry of the region.

From the results obtained we concluded the following:

1. Three regions with different characteristics were distinguished along the strip of measurements: towards the H_{II} region and in front of the PDR (phase 1); within the PDR (phase 2); and in the "molecular cloud" behind the PDR (phase 3).

2. The two-component model can be understood as a cold and dense layer (cold component) which is shielded by an external, hotter and more diffuse layer (hot component), which at the same time is more exposed to the heating sources (O and OB stars) embedded in the H_{II} region of M17. This model is in agreement with the common PDR structure described by Hollenbach & Tielens (1997). Furthermore, the results could also be understood, on smaller scales,

with a clumpy PDR model studied by Stutzki & Guesten (1990), where the cold component represents cold clumps embedded in a warmer inter-clump medium, which is represented by the hot component.

3. The last conclusion is that observations of these large structures (in the sub-millimeter range) could have been performed in a more efficient way with a larger camera. The mapping speed of the new camera for structures much larger than the telescope beam (as for M17 SW, $\sim 200''$x $200''$) would need to be: on one hand, a factor ~ 10 faster than LABOCA for the LFA, and on the other hand, a factor ~ 500 faster than SABOCA (the APEX continuum camera at 860 GHz) for the HFA (considering the same sensitivity per pixel). In addition, for the current study, the new camera will provide, data of 850 GHz which is not currently available. Actually, the new camera will provide in a single run of observations, the two frequency maps simultaneously, saving observing time from this side as well. Also, this will allow us to well characterize the low frequency part of the SED of the cold-component gray-body, without the need for combining maps from different instruments.

Bibliography

Baars, J. 2003, ALMA Memo Series, Memo 456

Baryshev, A., Baselmans, J. J. A., Freni, A., et al. 2011, IEEE Transactions on Terahertz Science and Technology, 1, 112

Beetz, M., Elsaesser, H., Weinberger, R., & Poulakos, C. 1976, A&A, 50, 41

Benford, D. J., Allen, C. A., Kutyrev, A. S., et al. 2000, in Eleventh International Symposium on Space Terahertz Technology, 187

Benoit, A., Yates, S. J. C., Grémion, E., et al. 2008, Journal of Low Temperature Physics, 151, 940

Bergin, E. A., Goldsmith, P. F., Snell, R. L., & Ungerechts, H. 1994, ApJ, 431, 674

Bhatia, R. S., Chase, S. T., Edgington, S. F., et al. 2000, Cryogenics, 40, 685

Blain, A. W. & Longair, M. S. 1993, MNRAS, 264, 509

Bohlin, R. C., Savage, B. D., & Drake, J. F. 1977, NASA STI/Recon Technical Report N, 78, 13984

Boisse, P. 1990, A&A, 228, 483

Brogan, C. L. & Troland, T. H. 2001, ApJ, 560, 821

Chapman, S., Blain, A., Ivison, R., & Smail, I. 2005, Spitzer Proposal, 20767

Cohen, M., Green, A. J., Meade, M. R., et al. 2007, MNRAS, 374, 979

Draine, B. T. 2011, Physics of the Interstellar and Intergalactic Medium

Dupac, X., Bernard, J.-P., Boudet, N., et al. 2003, A&A, 404, L11

Dupac, X., Giard, M., Bernard, J.-P., et al. 2002, A&A, 392, 691

Dupac, X., Giard, M., Bernard, J.-P., et al. 2001, ApJ, 553, 604

Evans, II, N. J., Rawlings, J. M. C., Shirley, Y. L., & Mundy, L. G. 2001, ApJ, 557, 193

Fazio, G. G., Hora, J. L., Allen, L. E., et al. 2004, ApJS, 154, 10

Fowler, J. W., Niemack, M. D., Dicker, S. R., et al. 2007, Appl. Opt., 46, 3444

Gatley, I., Becklin, E. E., Sellgren, K., & Werner, M. W. 1979, ApJ, 233, 575

Griffin, M. J., Bock, J. J., & Gear, W. K. 2002, Appl. Opt., 41, 6543

Guesten, R. & Fiebig, D. 1988, A&A, 204, 253

Güsten, R., Nyman, L. Å., Schilke, P., et al. 2006, A&A, 454, L13

Habing, H. J. 1968, Bull. Astron. Inst. Netherlands, 19, 421

Hanson, M. M., Howarth, I. D., & Conti, P. S. 1997, ApJ, 489, 698

Harper, D. A. & Low, F. J. 1971, ApJ, 165, L9

Harper, D. A., Low, F. J., Rieke, G. H., Harley, A., & Thronson, A. J. 1976, ApJ, 205, 136

Holland, W. S., Bintley, D., Chapin, E. L., et al. 2013, MNRAS, 430, 2513

Hollenbach, D. & Salpeter, E. E. 1971, ApJ, 163, 155

Hollenbach, D. J., Takahashi, T., & Tielens, A. G. G. M. 1991, ApJ, 377, 192

Hollenbach, D. J. & Tielens, A. G. G. M. 1997, ARA&A, 35, 179

Hollister, M. I., Czakon, N. G., Day, P. K., et al. 2010, in Twenty-First International Symposium on Space Terahertz Technology, 263–269

Irwin, K. D. & Hilton, G. C. 2005, Transition-Edge Sensors, ed. C. Enss, 63

Irwin, K. D. & Lehnert, K. W. 2004, Applied Physics Letters, 85, 2107

Kadin, A. M. 2005, eprint arXiv:cond-mat/0510279

Kauffmann, J., Bertoldi, F., Bourke, T. L., Evans, II, N. J., & Lee, C. W. 2008, A&A, 487, 993

Kreysa, E., Gemünd, H.-P., Raccanelli, A., Reichertz, L. A., & Siringo, G. 2002, in American Institute of Physics Conference Series, Vol. 616, Experimental Cosmology at Millimetre Wavelengths, ed. M. de Petris & M. Gervasi, 262–269

Lamb, J. 2001, ALMA Memo Series, Memo 359

Li, A. & Draine, B. T. 2001, ApJ, 554, 778

Low, F. J. & Aumann, H. H. 1970, ApJ, 162, L79

Maloney, P. R., Czakon, N. G., Day, P. K., et al. 2010, in Society of Photo-Optical Instrumentation Engineers (SPIE) Conference Series, Vol. 7741, Society of Photo-Optical Instrumentation Engineers (SPIE) Conference Series

Martin, H. M., Hills, R. E., & Sanders, D. B. 1984, MNRAS, 208, 35

Mazin, B. A. 2009, in American Institute of Physics Conference Series, Vol. 1185, American Institute of Physics Conference Series, ed. B. Young, B. Cabrera, & A. Miller, 135–142

Mazin, B. A., Day, P. K., Irwin, K. D., Reintsema, C. D., & Zmuidzinas, J. 2006, Nuclear Instruments and Methods in Physics Research A, 559, 799

Meixner, M., Haas, M. R., Tielens, A. G. G. M., Erickson, E. F., & Werner, M. 1992, ApJ, 390, 499

Monfardini, A., Benoit, A., Bideaud, A., et al. 2011, ApJS, 194, 24

Monfardini, A., Swenson, L. J., Bideaud, A., et al. 2010, A&A, 521, A29

Ossenkopf, V. & Henning, T. 1994, A&A, 291, 943

O'Sullivan, C., Cahill, G., Murphy, J. A., et al. 2008, Infrared Physics and Technology, 51, 277

Peretto, N., Fuller, G. A., Plume, R., et al. 2010, A&A, 518, L98

Pérez-Beaupuits, J. P., Spaans, M., Hogerheijde, M. R., et al. 2010, A&A, 510, A87

Povich, M. S., Churchwell, E., Bieging, J. H., et al. 2009, ApJ, 696, 1278

Povich, M. S., Stone, J. M., Churchwell, E., et al. 2007, ApJ, 660, 346

Price, S. D., Egan, M. P., Carey, S. J., Mizuno, D. R., & Kuchar, T. A. 2001, AJ, 121, 2819

Reid, M. A. & Wilson, C. D. 2006, ApJ, 644, 990

Revéret, V., André, P., Talvard, M., et al. 2008, Journal of Low Temperature Physics, 151, 32

Richards, P. L. 1994, Journal of Applied Physics, 76, 1

Sayers, J., Czakon, N. G., Day, P. K., et al. 2010, in Society of Photo-Optical Instrumentation Engineers (SPIE) Conference Series, Vol. 7741, Society of Photo-Optical Instrumentation Engineers (SPIE) Conference Series

Schlaerth, J., Vayonakis, A., Day, P., et al. 2008, Journal of Low Temperature Physics, 151, 684

Shetty, R., Kauffmann, J., Schnee, S., & Goodman, A. A. 2009a, ApJ, 696, 676

Shetty, R., Kauffmann, J., Schnee, S., Goodman, A. A., & Ercolano, B. 2009b, ApJ, 696, 2234

Shirley, Y. L., Evans, II, N. J., Rawlings, J. M. C., & Gregersen, E. M. 2000, ApJS, 131, 249

Shirley, Y. L., Huard, T. L., Pontoppidan, K. M., et al. 2011, ApJ, 728, 143

Siringo, G., Kreysa, E., De Breuck, C., et al. 2010, The Messenger, 139, 20

Siringo, G., Kreysa, E., Kovács, A., et al. 2009, A&A, 497, 945

Snell, R. L., Howe, J. E., Ashby, M. L. N., et al. 2000, ApJ, 539, L97

Stark, A. A. & Graf, U. 2013, STO Memo

Stutzki, J. & Guesten, R. 1990, ApJ, 356, 513

Tielens, A. G. G. M. & Hollenbach, D. 1985, ApJ, 291, 722

van Kempen, T. A., van Dishoeck, E. F., Salter, D. M., et al. 2009, A&A, 498, 167

Weiß, A., Kovács, A., Güsten, R., et al. 2008, A&A, 490, 77

Wilson, C. D., Howe, J. E., & Balogh, M. L. 1999, ApJ, 517, 174

Wilson, T. L. & Rood, R. 1994, ARA&A, 32, 191

Xu, Y., Moscadelli, L., Reid, M. J., et al. 2011, ApJ, 733, 25

Yoon, J., Clarke, J., Gildemeister, J. M., et al. 2001, Applied Physics Letters, 78, 371

Zemax manual. 2011, ZEMAX Optical Design Program User's Manual, Radiant ZEMAX LLC

Zhao, Y., Allen, C., Amiri, M., et al. 2008, in Society of Photo-Optical Instrumentation Engineers (SPIE) Conference Series, Vol. 7020, Society of Photo-Optical Instrumentation Engineers (SPIE) Conference Series

Zmuidzinas, J. & Richards, P. L. 2004, IEEE Proceedings, 92, 1597

List of Figures

List of Tables

Acknowledgments

First of all, I would like to thank Rolf for giving me the opportunity to do my PhD in the Technological division of the Sub-mm group in the MPIfR. It has been one of the best experience in my life, both at professional and personal level. Thanks also Rolf for all the advise and supervision given during my PhD. Also, I would like to express my fully gratitude to Stefan, for being my main supervisor and for all the help and supervision given during all the thesis. Many thanks to Juan Pablo for being my supervisor of at least one third of the thesis, and for being a guide in this new topic for me which was "astronomy"! Also, many thanks to Axel for all his advise and help, and being there to answer any question, here in Bonn and also in Chile. Many thanks also to Helmut for all his effort and helpful comments during the last days before submitting. I would like also to thank Karl, my official supervisor, and head of the department, for making this experience possible, and also, to Frank, my second official supervisor, for accepting to be part of my committee. Also thanks to Professor Brock and Professor Bott for being part of my examination committee. Gracias también a Iván, él fue mi primer contacto aquí en el instituto y sin su soporte e intención creo que esto tampoco hubiese sido posible. Also, many thanks to all the people of the department, scientific and technological group, because I am sure that you helped me at some point, even if it was for that coffee on that day in the kitchen, it was useful for sure.

Secondly, I am very happy to have a very very nice group of friends that always was, and is, supporting me, during the good and bad moments, always! Muchas gracias a todos por estar ahí siempre! a los de Bonn, los que están y los que ya se fueron, a los de Reus, a los de la Uni y a los del Penya. Me considero realmente afortunado por teneros, a algunos lejos físicamente pero cerca siempre en el pensamiento. Sin vosotros esto tampoco hubiese sido posible. Muchas gracias! Moltes gràcies! Grazie mille! Thanks a lot! Danke schön! Y en especial quiero agradecerle a Alice, por estar ahí siempre durante el último año y medio, per il tuo aiuto e appoggio in tutto questo periodo! Grazie Ali!

And my finally, quiero agradecer a mi familia por el apoyo incondicional que me han dado y me dan siempre, en todo lo que hago y que siempre han estado y van a estar destrás del teléfono por si se les necesita. Muchas gracias papá! Muchas gracias Laura! y también muy especialmente quiero agradecerle a mi madre que siempre ha sido y será un referente, que estuvo siempre ahí para todo cuando estaba entre nosotros, y ahora, desde algún lugar del cielo, ha estado y va estar siempre apoyándome en todo! Muchas gracias mamá!